

**CRITICAL SYSTEM ENGINEERING ANALYSES FOR
PLANETARY DEFENSE**

by

Warren G. Greczyn

B.S. in Aerospace Engineering, December 1986, The Pennsylvania State University

M.S. in Engineering Science and Mechanics, August 1989, The Pennsylvania State

University

A Dissertation submitted to

the Faculty of

The School of Engineering and Applied Science

of The George Washington University in partial satisfaction

of the requirements for the degree of Doctor of Science

January 31, 2006

Dissertation directed by Dr. David F. Chichka

Assistant Professor of Engineering and Applied Science

Abstract

The deflection of asteroid and comet Earth-impact threats is studied, and the kinematic requirements for threat object deflections that prevent Earth impact are characterized. This paper uses direct solutions of Kepler's equation coupled to an Earth gravitational model to determine threat object pre- and post-deflection orbital behaviors. The primary defense scenario considered is the deflection of asteroid threats through the application of a 1 cm/s velocity change, a level generally accepted by the planetary defense community as achievable in the near term. Threat displacement at Earth passage is assessed as the primary metric of deflection success. Key characteristics of defense system performance are analyzed, including optimal selection of the timing, direction, and required directional accuracy of successful deflections, along with duration of the threat engagement window and the effects of variations in deflection velocity. Deflected threat behaviors are developed parametrically for a representative threat set that spans the full range of observed hazardous threat orbits. The resulting trends are presented in conjunction with a broad-based treatment of the threat itself, including its origins, populations, general behaviors, and the history of both Earth impact and of efforts to develop an understanding of potential impactors. This is done with the aim of capturing the motivation for planetary defense in general and of making this paper a more complete and useful tool in the design of planetary defense systems, missions, and programs.

Table of Contents

Abstract.....	ii
Table of Contents.....	iii
List of Figures.....	v
List of Tables.....	xi
Chapter 1 - Introduction.....	1
Chapter 2 - The Threat.....	3
2.1 Asteroids.....	3
2.2 Comets.....	5
2.3 Earth Impact History.....	10
2.4 Probability and Consequences of Earth Impact.....	17
2.5 Our Reaction – General.....	20
2.6 Our Reaction – Surveillance.....	22
2.7 Our Reaction – Mitigation.....	28
2.8 Threat Structure and Response.....	33
2.9 Near Earth Object Orbits: Comets.....	38
2.10 Near Earth Object Orbits: Asteroids.....	40
Chapter 3 - Mitigation Modeling.....	46
3.1 Representative Threat Set.....	46
3.2 Threat Displacement Simulation.....	60
Chapter 4 - Threat Displacement Simulation Products.....	73
4.1 Asteroid Example Case.....	73
4.2 Representative Threat Set Analysis Points.....	87

4.3 Overall Asteroid Deflection Opportunities.....	89
4.4 Latest Possible Asteroid Deflection Before Earth Impact.....	91
4.5 Threat Displacement Margin Through Earlier Asteroid Deflection.....	92
4.6 Optimal Deflection Direction	97
4.8 Deflection Window Duration	105
4.9 Effect of Various Imparted Velocity Changes on Displacements.....	110
4.10 Threat Displacement Behavior Over a Range of Threat Inclinations	113
4.11 Comet Deflection Example Case.....	115
4.12 Comets and Inclination.....	122
Chapter 5 - Mission Design Conclusions	124
5.1 Mission Design Considerations.....	124
5.2 Follow-on Work	128
References.....	130
Appendix A – Perihelion Offset	135
Appendix B – Simulation Code Description	150

List of Figures

Figure 2-1: Oort Cloud and Kuiper Belt	7
Figure 2-2: Size Distribution of Discovered Earth Impact Craters.....	13
Figure 2-3: The Tunguska Event Overlaid on Washington D.C. Metro Area	15
Figure 2-4: Updated Hazard Curve.....	18
Figure 2-5: Cumulative Total of Known Near-Earth Asteroids vs. Time	23
Figure 2-6: Propellant Required for Rocket Engine Deflection of a Threat Object	32
Figure 2-7: Highlighted Impact Craters on Eros	35
Figure 2-8: Rotational Motion of Toutatis.....	37
Figure 2-9: Common Orbits for Short Period Comets.....	39
Figure 2-10: Extents of Example Aten Orbits	42
Figure 2-11: Range of Example Apollo Orbits.....	43
Figure 2-12: Representative Amor Orbits.....	45
Figure 3-1: Distribution of Perihelia for Observed PHAs	47
Figure 3-2: Inner Orbit of PHA 2004 UL	48
Figure 3-3: Distribution of Aphelia for Observed PHAs.....	49
Figure 3-4: Distribution of Aphelia for Observed PHAs Less Outlier	50
Figure 3-5: Orbit of Apollo 1999 XS35 Looking Down on Ecliptic.....	51
Figure 3-6: Orbit of Apollo 1999 XS35 – Oblique View	51
Figure 3-7: Distribution of Eccentricity for Observed PHAs	52
Figure 3-8: Distribution of Inclination for Observed PHAs	53

Figure 3-9: Attainable Single-Passage Inclination Changes for a Kuiper Object Encountering Earth	55
Figure 3-10: Histogram of Radii of Perihelion for Observed PHAs	56
Figure 3-11: Histogram of Eccentricities for Observed PHAs	56
Figure 3-12: Histogram of Inclinations for Observed PHAs	57
Figure 3-13: Scatter Plot of Eccentricity vs. Inclinations for Observed PHAs	59
Figure 3-14: Scatter Plot of Perihelion vs. Inclination for Observed PHAs	59
Figure 3-15: Representation of Process for Generating an Earth-Impact Threat: Step 1	63
Figure 3-16: Representation of Process for Generating an Earth-Impact Threat: Step 2	64
Figure 3-17: Representation of Process for Generating an Earth-Impact Threat: Step 3	65
Figure 3-18: Use of Sphere of Influence in Modifying Pre-Deflection Threat Orbit: Step 1	66
Figure 3-19: Use of Sphere of Influence in Modifying Pre-Deflection Threat Orbit: Step 2	67
Figure 3-20: Geometry of Applied Deflection Velocity.....	68
Figure 3-21: Use of Sphere of Influence in Calculating Threat Displacement at Earth	70
Figure 4-1: Example Threat Orbit for One Period.....	73
Figure 4-2: Example Threat Displacement Plot.....	74
Figure 4-3: Example Threat Maximum Deflection Offset from Perihelion	76

Figure 4-4: Example Threat Perihelion Passage.....	78
Figure 4-5: Example Threat Orbital Plot with Perihelion and Optimal Deflection Point.....	79
Figure 4-6: Comparison of Achievable Displacement for the Example Threat – Lateral vs. Velocity-Vector-Aligned Deflection.....	80
Figure 4-7: Example Threat Maximum Attainable Deflection at Earth	81
Figure 4-8: Example Threat Maximum Attainable Deflection at Earth to 450 Days Before Impact.....	82
Figure 4-9: Example Threat Transangle Values for Maximum Threat Displacement.....	82
Figure 4-10: First Successful Mitigation for Example Threat Case	84
Figure 4-11: Example Threat Transangle Values for Maximum Threat Displacement.....	85
Figure 4-12: Example Threat Maximum Threat Displacement Values.....	86
Figure 4-13: Example Threat Transangle Values Associated with Maximum Threat Displacement	86
Figure 4-14: Total and Successful Deflection Peaks by Perihelion for Unconstrained Representative Threat Set	90
Figure 4-15: Latest 1 cm/s Earth-Miss Deflection Opportunities.....	91
Figure 4-16: Deflection Times to Achieve Threat Displacement of 10-Earth Radii with a	93
Figure 4-17: Deflection Times to Achieve Threat Displacement of 10-Earth Radii with a 1 cm/s Deflection at High Eccentricities	94

Figure 4-18: Threat displacement Margin in Terms of Miss Factor; Low Perihelia.....	96
Figure 4-19: Threat displacement Margin in Terms of Miss Factor; High Perihelia.....	96
Figure 4-20: Example Threat Displacement over Transangle at 250 Days Before Earth Impact	98
Figure 4-21: Example Threat Displacement over Transangle from 200-300 Days Before Earth Impact	99
Figure 4-22: Example Threat Displacement over the Full Ten-Peak Range	100
Figure 4-23: Example Threat Displacement Over a Two-Peak Period	101
Figure 4-24: Sorted Distribution of Angular Deflection Window	103
Figure 4-25: Angular Deflection Window Widths for Zero-Degree Threat Inclination.....	104
Figure 4-26: Sorted Distribution of Temporal Deflection Window	106
Figure 4-27: Deflection Window Distribution for First Deflection Peak	107
Figure 4-28: Deflection Window Distribution for Tenth Deflection Peak	107
Figure 4-29: Deflection Window Behavior for Perihelion of 0.1 AU	108
Figure 4-30: Deflection Window Behavior for Perihelion of 0.2 AU	109
Figure 4-31: Effect of Increasing Deflection Velocity	110
Figure 4-32: Deflection Velocities Required to Recover a Full Earth Miss.....	111
Figure 4-33: Sorted Distribution of Threat Velocity Change Required to Achieve a True Earth Miss.....	112

Figure 4-34: Normalized Threat Displacement over a Range of Threat	
Inclinations	114
Figure 4-35: Comet Threat Case.....	116
Figure 4-36: First Successful Mitigation for Example Comet Threat Case.....	117
Figure 4-37: Transangle Values Required for Maximum Threat Displacement	
Against Example Comet Threat	117
Figure 4-38: Transangle Values Required for Maximum Threat displacement	
against Example Comet Threat	118
Figure 4-39: Transition in Transangle from Cometary to Asteroid Threats.....	119
Figure 4-40: Required Deflection Location (1 cm/s) for Earth Miss of	
Example Comet Threat.....	121
Figure 4-41: Variation over Threat Inclination of Deflection Time Required	
to Produce an Earth Miss	123
Figure A-1: Perihelion Offset Test Case.....	136
Figure A-2: Perihelion-Deflected Threat Closest Approach to Undeflected	
Threat Aphelion.....	138
Figure A-3: Deflected Threat Closest Approach to Undeflected Threat	
Aphelion: Deflections Occurring Before Perihelion	139
Figure A-4: Distance from Undeflected Threat Impact Point at Undeflected	
Time of Flight from Perihelion	142
Figure A-5: Change in Time of Arrival at Closest Passage to Undeflected	
Threat Impact Point.....	144
Figure A-6: Deflected Threat Closest Approach to Original Impact Point	145

Figure A-7: Deflected Threat Closest Approach to Original Impact Point:
 Deflections Occurring Before Perihelion.....146

Figure A-8: Monotonic Decrease in Threat Closest Approach to Original
 Impact Point: Deflections Occurring Before Perihelion147

Figure A-9: Deflected Threat Closest Approach to Earth: Deflections
 Occurring Before Perihelion148

Figure A-10: Zoom in of Deflected Threat Closest Approach to Earth:
 Deflections Occurring Before Perihelion.....148

Figure A-11: Non-Monotonic Behavior in Threat Closest Approach to Earth:
 Deflections Occurring Before Perihelion.....149

List of Tables

Table 3-1: Asteroid Threat Orbital Element Extents	58
Table 4-1: Case Run Summary	88

Chapter 1 - Introduction

The design and engineering trade spaces inherent in the development of a “planetary defense” system capable of defending the Earth against catastrophic impacts by asteroids or comets will prove to be enormously complex both technically and programmatically. Design variations will be practically limitless, and competition between factions pressing for emphasis on surveillance and those who urge that attention be weighted toward mitigation will make it difficult to achieve a coordinated development program. When a program is established, these two factions are sure to continue competing fiercely for scarce funding and other resources. In an actual planetary defense system, however, surveillance and mitigation must work together in an efficiently integrated and, most importantly, well-matched architecture: an approach with a highly-capable mitigation element will fail if it is matched with myopic surveillance, while robust surveillance is useless when paired with a stunted capability to mitigate.

This paper aims to illuminate key planetary defense system and mission design issues by presenting a parametric analysis of post-deflection orbital behaviors achievable against a representative threat set that encompasses the observed threat. Threat object displacement at Earth passage is assessed as the primary metric of deflection success. Key characteristics of defense system performance are analyzed, including optimal selection of the timing, direction, and required directional accuracy of successful deflections, along with the duration of the threat engagement window and the effects of variations in deflection velocity. The resulting trends are directly applicable as guidelines in the design of effective planetary defense systems, missions, and programs.

A brief treatment of the threat itself, prerequisite to placing any defense mission assessment into a proper systems engineering context, is presented in Chapter 2, The Threat. This includes overviews of asteroids and comets themselves, the history of Earth impacts, the expected probability and consequences of the impacts, the history of mankind's efforts to understand and address the threat, and the threat's physical structure and its potential reactions to mitigation efforts. Chapter 3, Mitigation Modeling, presents the representative threat set against which the parametric performance analysis was performed, and a description of the simulation process developed to carry out that analysis. Chapter 4, Threat Displacement Simulation Products, reviews in detail a sample threat deflection analysis as introduction to the general form of the generated data, and presents the core analysis results including magnitude of achievable threat displacements; timing, direction, and directional accuracy; engagement window duration; and effects of varying deflection velocity. Chapter 5, Mission Design Conclusions, discusses the simulation results in the context of their potential impact to the execution of a planetary defense mission, and highlights several areas of potential interest for subsequent research.

There are numerous sources for gaining a more complete understanding of any of these planetary defense topics; many but by no means all are cited in this paper. Omissions of references are for the most part relative to points that have been well established and accepted in the planetary defense community, and the omission of any one source should not be taken as judgment of its adequacy.

Chapter 2 - The Threat

The impact threat is classically and correctly divided into that presented by asteroids and that presented by comets. This chapter contains discussions of the origin and make up of each, the history Earth impacts, the expected probability and consequences of the impacts, the history of mankind's efforts to understand and address the threat, and discussions on the threat's physical structure and its potential reactions to mitigation efforts. At the conclusion of this chapter is a treatment on those threat objects that have been observed to approach nearest to the Earth. These objects are almost exclusively asteroids, and the discussion serves to introduce the development of a representative threat set.

2.1 Asteroids

Asteroids range in size from dust grains to planetoids many hundreds of kilometers across. The bulk resides in a torus between Mars and Jupiter: the well-known Asteroid Belt. The largest of the objects are believed to have interiors that, like the Earth's, have dissociated into a metallic core (mostly iron and nickel) underneath a rock mantle. In general, asteroids can be composed solely of or in combinations of rock and metal, but they are very often found to be an intriguing mix of carbon, hydrogen, oxygen, and nitrogen, the most elemental building blocks of life, at least as we know it.

The existence of much of the asteroid population is attributed to the destruction of a proto-planet that formed or perhaps formed only partially and briefly in an orbit just beyond that of Mars, the existence of said body being predicted by Bode's Law of

planetary placement [6]. This body survived only until the formation of Jupiter brought overwhelming gravitational disturbances to the region [21]. Prior to being destroyed, the body must have grown large enough and survived long enough to develop its own metallic core; this would explain how it is that some fairly small asteroids are comprised solely of iron-nickel despite being far too small to have accomplished core-mantle dissociation on their own [21].

While indigenous by definition to the Asteroid Belt, it is clear that asteroids enter into lower orbits. In general, they are driven inward from orbital positions within the Belt that happen to be in resonance with other planets, mainly Jupiter. In these zones, an asteroid will find that the gravitational tug from repeated passage by Jupiter is timed so that it occurs always in the same inertial direction (i.e., in the same direction with respect to the “fixed” star background). These tugs produce small displacements that are likewise always in the same inertial direction, and the displacements accumulate over long periods of time. Eventually the asteroid finds itself slowly being removed from the resonance orbit and placed into more populated regions of the belt, wherein it is more likely to suffer a gravitational encounter with another asteroid and perhaps then enter into an orbit that approaches the Earth. When these resonance orbits are examined telescopically, they are indeed found to be well emptied of objects.

This resonance/ejection process is apparently still at work delivering fresh asteroids to the inner planets at a fairly steady rate. This assertion is made essentially by default: if the process had ended, there would be very few asteroids in and amongst the inner planets (i.e., from Mars on inward), as that volume of space would have been cleansed by way of planetary encounters. As there are, in fact, large numbers of asteroids amongst the

inner planets, the question arises as to how it is that asteroids are continuously forced from the more populous regions of the belt into the short-lived resonance orbits from which some are eventually delivered inward.

The culprit, it turns out, is believed to be the Sun. As it shines on an asteroid, the object's rotation or tumbling motion (all have such motions to some extent [34]) constantly presents to the Sun a fresh, cool face to shine upon. That face, as it moves from local "morning" to local "noon," experiences a net inward flow of light energy and it becomes heated. As that very hot local surface then rotates on into afternoon and is decreasingly illuminated, the net flow of energy turns outward and the face cools. The low but steady outward flow of afternoon-pointing infrared photons that causes this cooling results in a net thrust that adds up over long periods of time as this "Yarkovsky Effect [36]" continuously changes the orbits of all asteroids, forcing some into the Jovian resonances and then, perhaps, to Earth.

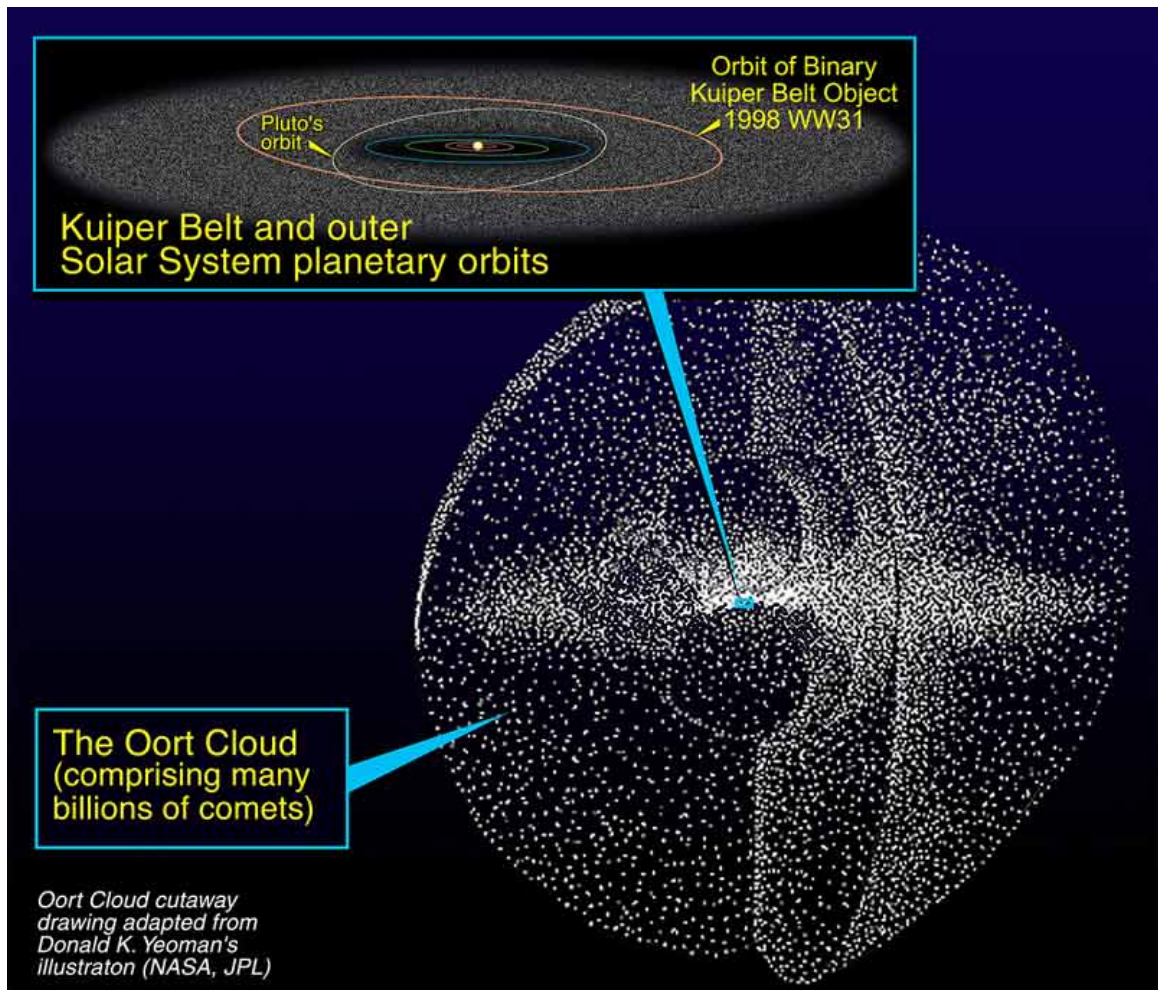
2.2 Comets

Comets are typically and appropriately described as dirty snowballs (in accordance with the famous description by Professor Fred Whipple of Harvard [18]). Each is a coagulation of mostly water ice, but also some methane and ammonia ices [45], mixed through with rock and dust [21], compressed by its own gravity and frozen into a solid mass by the cold of deep space. They were formed out beyond the rocky inner planets, starting just beyond the proto-planet that eventually became the Asteroid Belt and reaching to perhaps 50 astronomical units (abbreviated as "AU" and representing the average distance of the Earth from the Sun of about 149,600,000 km). There, far from the

new Sun, the frozen gases bumped against and attached themselves to the resident bits of rock and dust, the pieces accumulated, and comets grew.

In the regions of comet formation beyond Neptune (from 30 AU out to the 50 AU limit just described), the gaseous and dusty medium was too diffuse to create truly massive planetary bodies, so it was only comets that formed. This region is known as the Kuiper Belt, and, as is shown in the inset of Figure 2-1, it holds close to the ecliptic, as did the disk-like cloud from which the solar system originally condensed.

Figure 2-1: Oort Cloud and Kuiper Belt



Commonly held theory states that Kuiper Belt comets remained to a great degree out of the gravitational reach of even the outer planets, suggesting that most of them are still generally where they were created. That said, recent orbital modeling efforts have sparked a theory indicating that if the gas giants Jupiter, Saturn, Uranus, and Neptune had formed later than presiding theory demands, and if they did so in orbits other than where they currently reside (i.e., in orbits contrary to those required by Bode's Law), one can arrive at a final arrangement that is very nicely *in* accordance with Bode's Law and accounts for the heretofore unexplained eccentricities and inclinations of Jupiter's and

Saturn's current orbits. This new theory, however, also results in the orbits of Uranus and Neptune being temporarily cast out into the Kuiper Belt and clearing it of vast numbers of native comets, theoretically inciting the period of planetary development known as the Late Heavy Bombardment (LHB), a period of heavy planetary impact activity at approximately 700 millions years after the planets formed [15]. This theory has been called into question, however, on the point of whether the beginning of planetary formation actually held off long enough to allow this emptying of the Kuiper Belt to coincide with the LHB [35]. (Regarding the collective reference to the "gas" giants, it is acknowledged that Uranus and Neptune are more popularly and more properly referred to as the "ice" giants, because of their icy mantles.)

Regardless of its current population, the Kuiper Belt most assuredly contains only comets, again, thanks to the low density of the gaseous medium in that part of the early solar system. However, in the region from Neptune's orbit at approximately 30 AU down to what would eventually be the location of the Asteroid Belt, the native medium was relatively dense and found itself further enriched by gases blown out of the inner solar system by the light pressure of the newly ignited Sun, a process that assured that the inner planets indeed would be rocky. This medium was sufficiently thick to support not only massive cometary production, but also *planetary* production, specifically, that of the gas and ice giants. With the formation of these planets, overwhelming gravitational disturbances were created, and the comets of this region were summarily ejected, flung in random directions into essentially interstellar space. There, where the Sun's gravitational attraction is extremely weak, many of their orbits were stabilized by the gravity of passing stars and interstellar nebulae [45], or by galactic tidal forces [22]. The result,

shown in the main portion of Figure 2-1, is the Oort Cloud, a thick shell of frozen bodies thought to surround the Sun essentially equally in all directions starting at about 0.5 light-years and extending to perhaps 3 light-years, over 190,000 times the distance from the Earth to the Sun.

The sizes of Oort objects have not yet been determined by direct observation, but estimates range from several tens to over one hundred kilometers in diameter: Earth impact by an Oort object would likely result in the permanent sterilization of our planet, if not its outright pulverization [11]. Making the situation worse is that Oort objects are thought to exist in staggering numbers: the NASA source cited in Figure 2-1 estimates “many billions,” while high-end estimates approach a trillion [21]. This is not to say that the Oort comets are crowding each other. If the outer edge of the Oort Cloud is assumed to extend to only 0.75 light-years, its surface area still would be over 7 square light-years, and the average volume of space available for each of a trillion bodies would be over seventy-five times the spherical volume inside the Earth’s orbit. Spacing is probably tighter in the Kuiper belt, but the probability that any two Kuiper objects will encounter one another and make their escape by virtue of that encounter seems extremely small; for any two Oort objects it seems vanishingly small. Clearly, though, some comets do escape. For Oort objects this can be attributed to the same forces that had originally trapped them: again, the gravity of passing stars and nebulae, or galactic tidal forces. Likewise, Uranus and Neptune sometimes do manage to act on Kuiper objects sufficient to perturb their orbits over time perhaps enough to cause them to encounter neighboring objects, and then to enter long dives toward the inner planets [4].

As extreme and vanishing as are the respective chances of encounters among Kuiper and Oort objects, the sheer number of objects and the enormity of time since the creation of their respective populations gives such encounters at least some statistical probability of occurrence. When a comet is finally compelled by some series of mechanisms to dive toward the inner solar system, however, its descent is not a rapid process. If an Oort comet's dive began even from the inner edge of the cloud it would take almost three million years before it finally reached Earth. If an Earth impact by an Oort comet is imminent, our demise would have been decided long before the first humans ever existed. Objects from the Kuiper Belt do not take quite so spectacularly long to fall: sun-approaching comets with perihelia of, say, 1 AU and aphelia of 30 to 50 AU – the aforementioned extents of the Kuiper Belt – would have respective periods between 60 and 130 years.

2.3 Earth Impact History

Realization of the impact threat to Earth is not new. The earliest reference to at least the possibility that celestial bodies could collide is thought to have been presented as early as the fifth century B.C. by the Greek thinker and philosopher Democritus [45]. Both the potential for collisions and their dire consequences were formally documented as early as the 1690s by Edmond Halley [50]. His realization might very well have occurred upon consideration of “his” comet, although it was not named Comet Halley until after he died: there is no evidence that Halley or his contemporaries recognized that many of the Earth's surface features are, in fact, impact craters. Today it is generally accepted that Halley was quite correct to believe that the Earth, Moon, other planets and

their moons have all suffered huge numbers of impacts, some by comets, some by asteroids, many quite tremendous. The Moon itself is thought to be the oldest single piece of evidence of the catastrophic nature of such events, as a standing theory holds that it was formed from the swept-up debris of a massive impact suffered by the Earth perhaps only 50 million years after its creation [8].

It is our planet's more recent geologic and fossil record, however, that brings out the full implication of Earth's impact history. The most compelling and celebrated chapter of this history centers on a crater 180 km across [16], created 65 million years ago and now buried deep under Mexico's Yucatan by ages of geologic activity [3]. The geologic record shows that appearing simultaneous to this crater's formation is a layer studded with bits of impact-melted rock along with high concentrations of iridium and chromium 53 isotope, two materials that are of relative abundance in extraterrestrial bodies but that are rare on Earth [54]. By all evidence this layer of what appears to be impact debris envelopes the entire planet.

Based on this geological evidence, it is a near certainty that the Chicxulub crater (named for a village in the region) is the healed-over impact scar from an asteroid perhaps 10 km in diameter that impacted the Earth at several tens of kilometers per second [54]. What makes this event so profound is that the global layer of geologic debris marking the time of this impact also happens to divide two very distinct periods of life on this planet: the Cretaceous Period, marked most notably by the proliferation and nearly complete dominance by the dinosaur, and the subsequent Tertiary Period, equally notable for its conspicuous and nearly complete *absence* of dinosaurs, exceptions being very few but including those which later evolved into birds [56]. This Cretaceous/Tertiary

delineation is the now widely-discussed “K/T boundary” (so named because “C/T” had already been given to the admittedly more obscure geologic boundary between the Cenomanian and Turonian periods). The K/T boundary represents not just the nearly complete demise of the dinosaur, but a 70% reduction in the overall number of species on the planet.

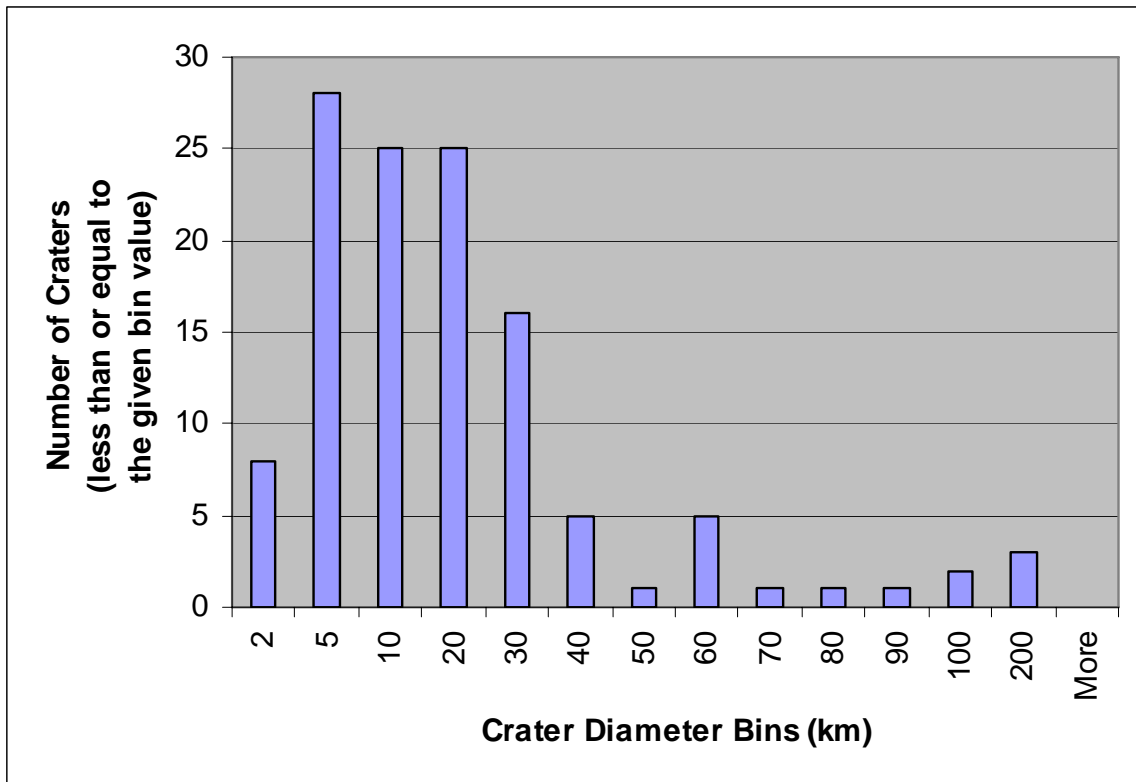
The massive die off that occurred across the K/T boundary may have taken place over a very short period of time, perhaps as little as a few years, although a recent theory runs slightly counter to this broadly accepted assertion [56]. The mechanism of the die off was most likely starvation. It is believed that vast quantities of dust were injected into the stratosphere by the impact, and that a global shower of molten droplets of ejected rock sparked planet-wide forest fires. With dust and smoke conspiring to blacken the skies for what may have been years, photosynthesis was stifled, and the global cooling effect referred to as “impact winter,” a condition akin to “nuclear winter,” took hold. The environmental effects of this single asteroid impact ended the evolutionary chains of vast numbers of higher life forms on the Earth, and life on our planet today might look startlingly different had that impact not occurred: the age of the dinosaurs well might have continued, and because the age of the mammals well might have never occurred, mankind might not have existed.

Important as it was to the character of life on Earth, the Chicxulub event was not Earth’s first catastrophic impact. Geologic evidence similar to that in K/T boundary indicates a series of impact-generated extinction events, a standout being the truly massive die off at the Permian-Triassic boundary 250 million years ago, where up to 96% of marine species and 99% of reptile genera vanished [44]. The actual crater from that

impact has not been identified, but numerous other impact scars are still evident today.

Figure 2-2 shows that of those terrestrial craters that have managed to survive the erasing effects of plate tectonics and other geologic and erosive processes, 61 are at least 10 km in diameter, 13 are over 50 km, and there are 5 that stand at 100 km or larger.

Figure 2-2: Size Distribution of Discovered Earth Impact Craters [16]

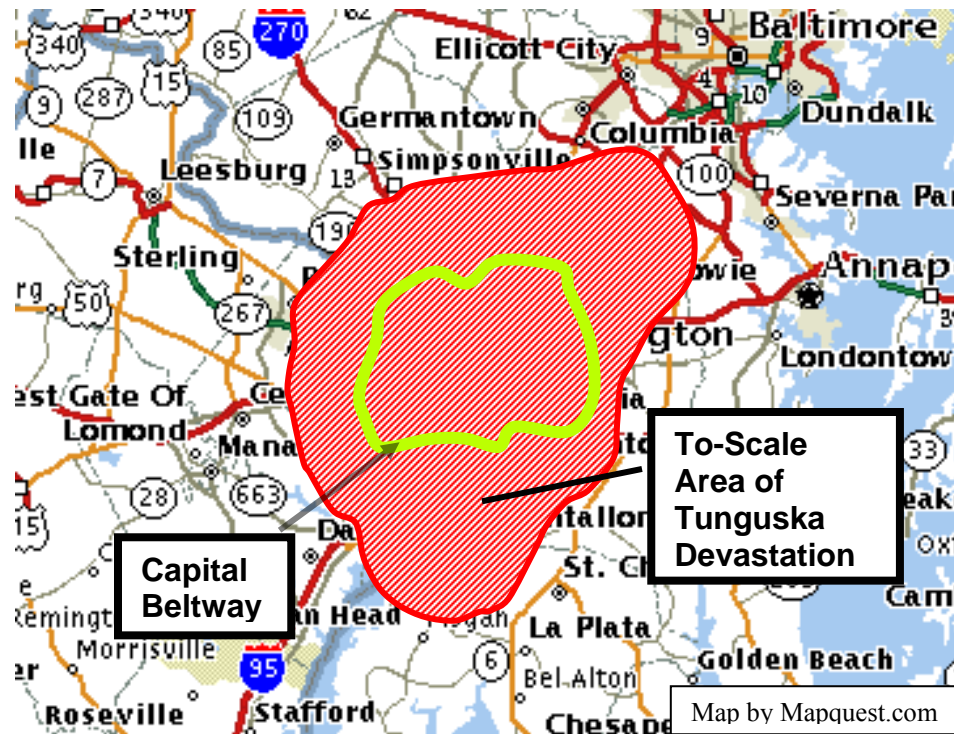


Comforting though it would be to have comet and asteroid impacts confined to distant history, they are not. Of the many relatively recent encounters, the most studied, discussed, and argued of them is what is known as the Tunguska Event. In 1908, what was either a small piece of a comet on the order of 100 meters in diameter [5] or a small stony asteroid of perhaps 60 meters [33] entered the Earth's atmosphere over the

Tunguska region of Siberia. As the object plunged deeper into the atmosphere, the increasingly-thick air created tremendous aerodynamic forces on the leading face of the body. At only a handful of kilometers short of the Earth's surface, those forces exceeded the material's structural strength and the front of the body fragmented, creating a sudden jump in the surface area being blasted by the oncoming air and thus a nearly instantaneous spike in the aerodynamic forces being suffered by the body [47]. This fragmenting chain reaction engulfed the object, pulverizing it and converting essentially all of its kinetic energy into a massive explosion [23]. Because the object was traveling perhaps in excess of 30 km per second, that energy release, which goes as the square of velocity, may have been close to 50 megatons [47], 2500 times the energy released on either Hiroshima or Nagasaki.

The outcome was devastating. As relatively crude as were the scientific instruments of the day, they were able to register the passage of the blast wave as it circled the globe twice. When an exploration team finally reached the site in 1930, they found that 2000 square kilometers of thick forest had been knocked flat, the fallen trees still all pointing radially away from the center of the blast [45]. The shaded region in Figure 2-3 is a to-scale overlay of the destroyed region in Tunguska superimposed onto the Washington, D.C. metropolitan area. If an object similar to the one in question were to enter our atmosphere over the U.S. Capital, there would be very little left standing and few left alive both inside the Beltway (the lighter inner ring) and in much of the surrounding areas.

Figure 2-3: The Tunguska Event Overlaid on Washington D.C. Metro Area



The Tunguska Event made it clear that asteroids and comets (or certainly cometary pieces) do not have to reach the ground in order to do horrendous damage. However, when such objects do reach the ground, the stakes rise dramatically. A surface impact from a stony object only 200 meters in diameter could obliterate – literally wipe clean – an area the size of Connecticut [49]. Kilometer-wide Meteor Crater, Arizona’s famous 50,000-year-old [16] landmark (literally), was created by an iron object thought to be only 30 meters across [1], and is a startling portrayal of how such objects, even if made essentially of a monolithic piece of stainless steel, do not burrow their way into the Earth after impact, but explode very near the surface and with tremendous force.

Any such surface hit on Earth, of course, has essentially a 70% chance of occurring in water, and about a 50% chance of occurring in a deep ocean basin. An object at the larger

end of the size scale such as that which produced the Chicxulub crater would most likely survive passage through the water, and would then detonate upon meeting the underlying rock. The result would be similar to that of Chicxulub, which itself may have been at least a partial water impact. A smaller object, however, such as a comet fragment or small asteroid, will explode nearer to the water's surface. This would produce a deep-water wave: a tsunami. Such a wave might be only 1 or 2 meters high at the surface of a deep ocean basin, but it would have enormous amplitude, reaching perhaps to the sea floor for larger impactors. Because that amplitude will fall off only inversely with the distance from impact [19], a threat object as small as 100 meters in diameter can produce a deep-water wave that would still be up to a meter high even at 1000 km from the ocean impact point. When the wave approaches a continental shelf (and it will do so at perhaps several hundred miles per hour) it will slow but its massive energy will cause it to also rise, its final height at shore being dependent on local topography. The ratio of wave's height at shore compared to its height in deep water, referred to as the "run-up factor," is typically somewhere between 10 and 25, resulting in an on-shore wave typically between 3 and 8 stories high.

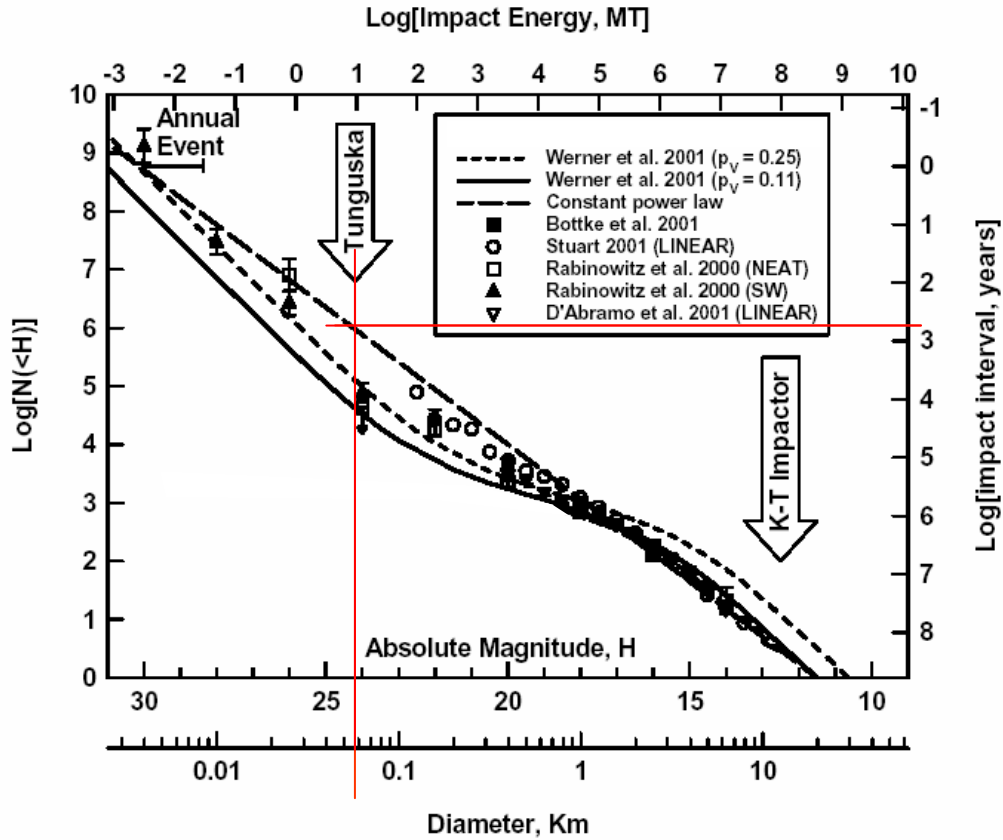
Damage from such an event will certainly not be confined to beachfront property, as the tsunami in the Indian Ocean basin has shown. Waves of the size described can be carried perhaps 30 km inland and up to 4 times farther for less resistive croplands or grazing lands [19], with the flow of water itself and the debris it carries scrubbing the land clean. Recent efforts to model the water surface "craters" produced by asteroid impacts do reduce predicted on-shore wave heights somewhat, but with man's propensity

to build and live very near coastlines, the inherent danger of impact-produced tsunami remains substantial.

2.4 Probability and Consequences of Earth Impact

While it is clear that comets and asteroids continue to present a threat to Earth and to the life on it, in order to know whether and to what degree action should be taken against this or any threat, an understanding is required of the probabilities involved. It was by a painstaking census of the Moon's vast collection of layered, overlapping, and often mutually-obscuring craters that the first estimate of the rate of Earth impact was calculated. An updated version of that original "hazard curve" as it is called, is shown in Figure 2-4.

Figure 2-4: Updated Hazard Curve [33]



The plot's left vertical axis presents a measure of the cumulative population of those threat objects whose brightness is less than the indicated absolute magnitude H . (Absolute magnitude is the object's visual magnitude as it would be observed if it was at 1 AU from both an observer and the Sun, with the observer able to see in full the object's sun-lit face. H can be related to threat object size, but only through a series of assumptions as to the optical properties of its surface.) The remainder of the plot is dedicated to the average interval expected between impacts as a function of threat object size or, equivalently, impact energy. The "average" nature of the interval statistics must be stressed. Having suffered the 1908 Tunguska impact, there was nothing to prevent an event of the same scale from occurring the very next year, nor is there any guarantee that

a similar event must occur within 650 years, which is the average interval reported in Figure 2-4 for Tunguska-sized events. Note that the object diameter associated with Tunguska in Figure 2-4 indeed registers at just below 60 meters, but the associated explosive energy reads at one-fifth of that referenced earlier. The difference translates to a factor of approximately 2.25 in assumed impact velocity if constant object mass is assumed. This highlights the theoretical nature of estimating an event's impact energy from the size of the crater or area of devastation.

Impact rate data are certainly the first step toward understanding the impact risk, but it does not by itself present impact frequency in terms of consequences. If the consequence of interest is loss of human life, the peak risk would come from impactors that are just large enough to cause truly global effects (i.e., the plant die off and subsequent pervasive starvation such as that attributed to the impact at Chicxulub). The risk peaks here because while the impact of a slightly larger object could cause greater loss of life, the probability of actually encountering that slightly larger impactor drops precipitously as was shown in Figure 2-4, so the overall risk is lower. This regional-to-global transition is believed to occur at threat diameters of around 1 kilometer, where the expected loss of human life peaks at about one-quarter of the world's population, or approximately 1.5 billion people [32]. When the approximated probability of impact of that 1-kilometer object is coupled with a standardized life expectancy figure of, say, 75 years, the product is a unified statement of the risk under which everyone on the planet exists: a 1 in 40,000 chance of being killed in an asteroid or comet impact event [29], about half the probability of being killed in the crash of a large commercial airliner [32]. As with airliner accidents, it is not typically expected that only one or two people would

die in an asteroid or cometary event. Unlike airliner accidents, however, it is very likely that even a moderately catastrophic event could kill many millions.

2.5 Our Reaction – General

The broad-audience reaction to the impact risk as quantified earlier is most often one of healthy interest, but seldom more. This is very much in spite of the fact that if a catastrophic impact were to occur today (Figure 2-4 indicates that it is just a matter of time) it most likely will occur with essentially zero warning. Still, the derived 1-in-40,000 probability of death is apparently just not that frightening. Were it sufficiently frightening, a consolidated and well-funded planetary defense development effort would already be in place. No such effort exists, but this is not to say that the danger has gone unnoticed.

As previously mentioned, Halley documented the consequences of the impact threat as it was understood late in the 17th century. It was not until the early 19th century, however, as astronomy began to mature and, more importantly, as it became increasingly popularized, that some fairly encompassing but admittedly ornamental statements on the topic are first found, and those from the unlikely source of Lord Byron. He saw it as extremely ironic that something sufficiently disturbing could occur to the heavenly bodies so admired by man as to “...bring one down amongst them, and set fire unto their ant hill [50].” Not one to leave a line of thought incomplete, Byron also prophetically mused that mankind might defend itself and “tear rocks from their foundations by means of steam, and hurl mountains... against the flaming mass [50].”

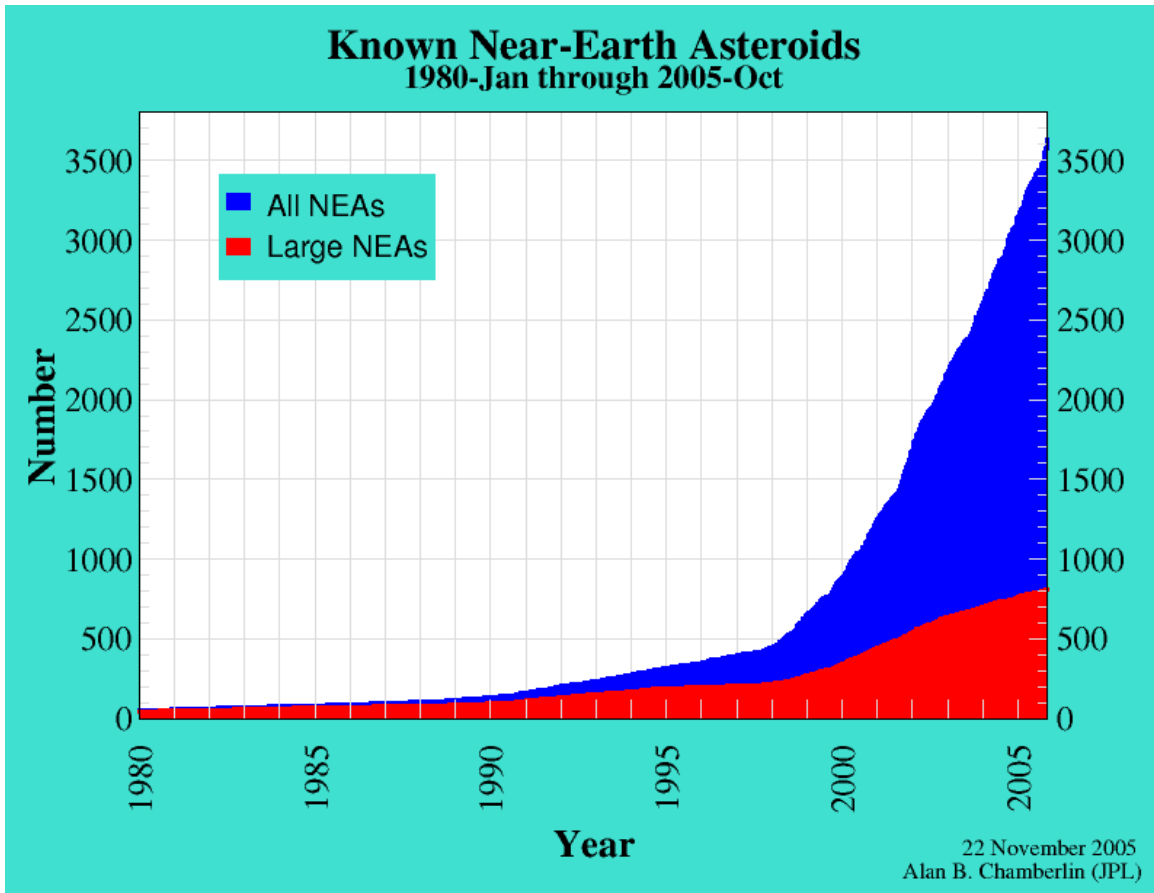
The first contemporary scientific treatment of interest to the discussion (if the pseudoscientific writings of the 1950s [53] are ignored) had to wait until 1968, but even then the discipline had risen only to the level of a class project at MIT [55]. At the time, however, the two pieces of key information needed to establish planetary defense as a true discipline were still missing, and they did not start to surface until 1980. It was that year that saw the establishment of the Spacewatch Program at the University of Arizona, a concerted effort to count and characterize near-Earth threat objects. By coincidence, it was that same year that the connection was made between the Chicxulub crater and the mass extinctions of the associated K/T Boundary. Together, these new understandings, first of the planetary defense threat population and second of the severity of the consequences of the impacts, allowed a leap forward in the perception and recognition of the overall threat.

It was not until a decade later, however, after a combined urging by an April 1990 American Institute of Aeronautics and Astronautics (AIAA) position paper [51] and the painfully close passage with essentially zero warning of an asteroid with the unassuming name of 1989FC, that Congress directed two workshops be convened, one on asteroid and comet detection and one on mitigation [51]. Congress no doubt felt especially justified in its decision when four years later, as if to prove that impacts do occur, a 10-kilometer comet named Shoemaker-Levy 9 broke into pieces and slammed into Jupiter, releasing perhaps a quarter of a million megatons of energy [22].

2.6 Our Reaction – Surveillance

The reports from these Congressionally-mandated workshops became the blueprint for much of the activity that followed. The product of the workshop that focused on detection was a plan for the “Spaceguard Survey,” a 20-year program for finding and cataloging 90% of those Near Earth Objects (NEOs, although the term NEAs is often used when only asteroids are concerned) having diameters at or above the peak-risk diameter of 1 kilometer. This surveillance program is in fact currently being conducted, now a joint venture between NASA and the Air Force, and is very much on its way to meeting its goal of completing its NEO catalog by 2008. The pace of discovery of this survey is shown in Figure 2-5.

Figure 2-5: Cumulative Total of Known Near-Earth Asteroids vs. Time [38]



Modern asteroid hunting of the type that populated Figure 2-5 is conducted with ground telescopes outfitted with electronic focal planes, the digital output of which is examined by software designed to pick out automatically the telltale motion of an asteroid against the constant star background. When a moving object is spotted, and if it is confirmed to be both a new object and one having an orbit that crosses into the region of space between Earth's orbit and that of Mars, it is labeled an NEO. (While objects that approach the Sun no closer than the 1.3 AU of Mars' orbit certainly have no immediate chance of colliding with the Earth, they could have a substantial probability of being further perturbed by a Mars encounter, and so they are included in the count.) Further, if

it is determined that the new object will at any time in its predictable future pass within 0.05 AU of the Earth (just shy of 20 times the average distance from Earth to the Moon, center to center) it is given the addition label of Potentially Hazardous Asteroid (PHA, or PHC for a like-behaving comet).

Thus far, none of the cataloged PHAs have been projected to have any possibility of actually striking the Earth: the closest projected passage of any sizable object as of the completion of this text was that of asteroid 2004 MN4 (recently named 99942 Apophis), which will close to perhaps 24,000 km of the Earth in 2029. In general, however, asteroid projections are not always that accurate that far into the future, as the projections depend on the accuracy of our estimates of the gravitational forces inflicted on the threat by the Sun, other planets and moons, and other asteroids [27]. Though tiny, these errors build upon each other and dominate the calculations if projections are made too far into the future. Also, it must be remembered that by no means have all hazardous objects been discovered; based on the patterns of asteroid discovery represented in Figure 2-5, it is estimated that there are about 1100 NEAs of 1 kilometer diameter or larger [37], only about 820 of which have been found.

The most difficult to detect of the undiscovered NEAs will probably be the final 10% that will remain after Spaceguard has achieved its 90% goal. It is a good possibility that the reason these holdouts will have waited to be discovered is that they have very low albedos, making their signatures challenging to the current ground-based systems [10]. These systems also have viewing limitations such as restrictions on how close the center of observation can be to the local horizon or to the galactic plane, and on how far the Sun and Moon must be below the local horizon [17]. It is possible, therefore, that some

portion of the hold-out NEAs are in orbits that are challenging to ground-based telescopes.

These restrictions force the question of whether asteroid hunting should continue to be performed from the ground or should at some time be moved to Earth-orbit, the lunar surface, or even deep-space platforms. Further, regardless of from where the search is conducted it might be best to conduct it in the infrared (as opposed to visible bands), in which the objects being hunted are bright even when only their night sides are observable. This is due to the fact that, as mentioned previously, all asteroids rotate or tumble to some extent, and thus spread the Sun's heat around their mass in a fairly even fashion [42]. However, if advantage is to be taken of this thermal symmetry, space-based sensors must again be considered, as they do not have to look through a warm and IR-absorbing atmosphere. It is at this point, however, that the discussion will be abandoned, as there are already a sufficient number of voices on each side of the ground-vs.-space surveillance argument. Suffice to say that for now the space-basing option is open for consideration, and in the mean time, ground-based systems are continuing to find NEAs [38].

Once an object is found and determined to have not been previously observed, the next task is to try to make a rough estimate of its size, and, to whatever extent possible, its material makeup and bulk structural properties. First estimates of size can be made by knowing distance and brightness, but the relationship between these two is dependent on the object's albedo, which, as mentioned earlier, must be estimated. Multi-color imaging or spectroscopy can often give clues as to surface material, from which bulk material properties can be inferred to some degree. Also, changes in brightness as the object

rotates or tumbles through space can sometimes give clues as to the general shape of the body. Further, an object is sometimes found to have a rotation rate so high that, given its particular size, it would fly apart if it was only a collection of gravitationally-attracted pieces, implying that the object under observation must be a solid body. Unfortunately, if an object's observed spin rate is not above that discrete threshold, no such assumption can be made as to its internal structure. However, should any object come within the field of view of one of the large planetary radars, such as Goldstone (a 70-meter steerable dish) or Arecibo (a 300-meter fixed dish), much of the guesswork can be removed. Such instruments can estimate surface material composition based on the character of the radar backscatter, and can discern in great detail an asteroid's overall shape, rotation or tumble characteristics, and even surface topography.

The bulk of the surveillance discussion thus far, though centered on asteroids, is also applicable to comets, although they are in general more problematic. Until their orbits bring them close enough to the Sun for their characteristic and easily-observed tails to start to form (which usually does not occur until the object is inside the orbit of Jupiter) comets will be, in general, many magnitudes fainter than comparably-sized asteroids. This is partially because in general they will be farther away than most asteroids of concern, but also because they often will have lower albedos: in the "dirty snowball" description of comets, it is the "dirty" factor that is thought to dominate, at least with respect to surface materials. There are also cases where the asteroid/comet line is blurred, as asteroid-like objects have been found in orbits that rightly belong to comets. These are believed to be extinct cometary cores, having flown close to the Sun so many times that little of their original volatiles remain. This class of objects turns out to be the single

worst possible Earth impact threat, as they are extremely difficult to see (they are dark and no longer can form observable tails) and can have Earth-relative velocities up to 70 km per second if in a retrograde orbit near the ecliptic. With energy of impact being proportional to the square of that Earth-relative velocity, an object on the described trajectory need be only a little over half a kilometer across to inflict the damage otherwise expected from a 1-kilometer asteroid.

To detect inbound comets when they are still beyond the orbit of Jupiter, whether they are extinct or still filled with volatiles, a survey might have to reach as far down as 7 magnitudes fainter than the present effort [10]. Building a surveillance system to this level would have the additional advantage of increasing the capability to catalog smaller near-Earth asteroids, which, though below the 1-kilometer observation goal of Spaceguard, exist in much greater numbers and are very capable of regional or even continental devastation. While the NEO survey has cataloged over 4 times as many sub-kilometer objects as it has those with diameters of 1 kilometer and above (as was shown in Figure 2-5), there is a call in the planetary defense community for the survey to formally reduce the object size threshold of interest down to the 200-to-300 meter range [31], which would require the survey to extend down the visual magnitude scale to about 24 from where it currently sits at 19.5. This is driven to a great extent by the growing understanding of and commensurate concern about the aforementioned small-asteroid tsunami threat. Focusing the search on NEAs smaller than 1 kilometer has also been recommended by the US National Research Council [40].

2.7 Our Reaction – Mitigation

At some time in the future, a detected threat object could be determined to have a substantial probability of colliding with the Earth. When that occurs, there are two distinct approaches that can be taken. Much has been written about survival-oriented options such as evacuation of at-risk coastal regions. Unfortunately, this is applicable only to the smallest ocean impactors and carries the unfortunate consequence of leaving behind all non-movable possessions, architecture and other cultural treasures to be destroyed. Likewise there have been proposals for the creation of cavernous bomb shelters in deep mines located well away from the predicted impact site. This approach presents the unenviable and Strangelovian task of deciding who gets in and who does not, while creating the suspenseful hope that the prediction of the location of impact was not off by too far. Such options all fall far short of what is inherently advertised by the term “planetary *defense*.”

True defense-oriented options, preferable by the author’s thinking but certainly with extreme challenges of their own, fall into two basic families of action: deflection and what is often termed “dispersal.” The latter option entails an outright disruption of the threat object into a scattering of smaller pieces, as might be achieved by, for instance, the detonation of an implanted nuclear device. To justify taking this approach, however, a guarantee would be needed that the dispersal velocities achieved would be sufficiently large and that residual pieces would be sufficiently small that any portion of the original threat object that does still continue on to Earth impact would produce an acceptably low level of damage. If dispersal velocity does not sufficiently exceed the escape velocity of the object’s collective-mass, the pieces will simply reassemble. Likewise, if the dispersed

threat pieces that do remain on an Earth-impact trajectory are too large to be destroyed high in the atmosphere there would be a diminished but still catastrophic series of impacts. While it is believed that existing nuclear devices could fragment stony objects up to perhaps 100-meters in diameter and comets up to 500 meters, the largest surviving fragment still would be nearly half the diameter of the parent body [52]. It is an oddity of the planetary defense trade space is that if an object is small enough for a dispersal to leave only safely-sized fragments, it is probably small enough to be simply deflected.

There are several options available for producing deflections in threat objects, and they divide roughly into two camps: those that deliver a single and relatively large impulsive velocity change and those that apply low-level but continuous thrust so as to build up a sufficient velocity change over an extended period of time. Continuous thrust options include such mechanisms as mass drivers or solar sails, or feature some form of directed energy impingement, wherein the threat object is illuminated with a laser or with concentrated sunlight to continuously “boil off” small portions of its surface to produce a reaction mass [24]. A newly-emerged concept is that of a “gravity tractor” where a high-mass spacecraft with advanced nuclear ion propulsion would maintain a constant but small distance between it and a threat object. Over time, the mutual gravitational attraction between the object and the spacecraft would modify the object’s velocity [25]. Unfortunately, even if the near future sees devices of any of these sorts developed and space qualified, their application to planetary defense would still face enormous challenges. Engineering the attachment and operation of a massive sail to what would in all likelihood be a randomly-rotating and equally randomly-shaped asteroid; or the long-term and most likely autonomous operation of the machinery needed to collect and feed

host-asteroid material to a mass driver; or even scaling up solar concentrator or laser sizes so as to effect a reasonable thrust would all be extraordinary feats. The gravity tractor concept is attractive in that it negates the issue of the rotational state of the object, but the required level of propulsion technology development would be substantial.

As with solar concentrator or laser impingement approaches, impulsive deflection concepts generally seek to deposit energy into the threat object so as to create ejecta as a propulsive reaction mass: the rapid or even explosive release of ejecta in one direction so as to effect a small but measurable change in velocity of the parent body in the opposite direction, in accordance with conservation of linear momentum. The deposition energy can come from a nuclear device (whether surface, sub-surface, or stand-off), or simply by the hypervelocity kinetic impact of a space vehicle. While the actual energy transfer mechanisms brought into play with a nuclear device are quite complex and depend greatly on the style of device being employed, the extraordinarily high energy densities of these devices has made the technical efficacy of this approach fairly broadly accepted [46]. On the other hand, however, initial skepticism as to the efficiency of kinetic impact deflections is quite understandable. If an interceptor spacecraft of, say, 10,000 kilograms finds itself engaging even a relatively small, stony threat object of, say, only 50 meters in diameter, its mass is barely better than $1/20,000^{\text{th}}$ that of its onrushing opponent.

Relief in this apparently one-sided contest comes by virtue of the asteroid's tremendous velocity. In many of the cases of interest the orbital velocity of the threat itself will be so high that an intercepting spacecraft will have to do little more than simply get in the threat's way to assure that the impact causes essentially complete conversion of the interceptor's kinetic energy into explosive heat energy. It is the deposition of this

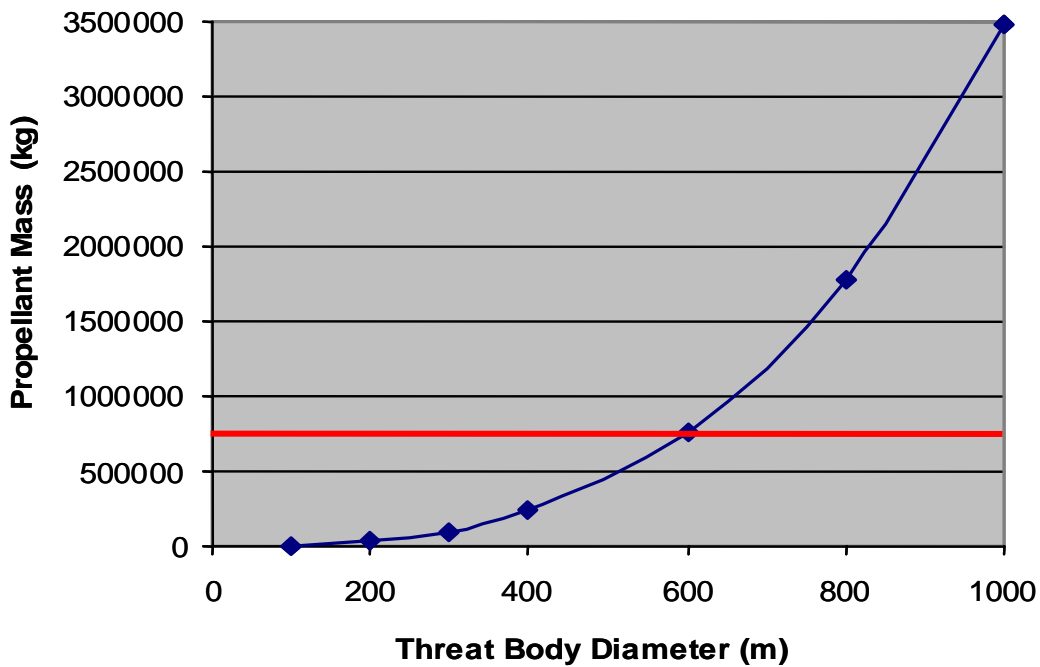
energy that produces the sought-after ejecta and does so, ironically, by the same kinetic energy mechanism that makes threat impacts so damaging to the Earth's surface [49]. It is of note, therefore, that when a kinetic impact is employed, the goal is not the production of a momentum effect, but of conversion and deposition of the impacting spacecraft's kinetic energy to produce ejecta as a reaction mass [24]. In fact, at the relative velocities involved, the specific energy of an intercepting spacecraft, while well shy of that of nuclear devices, is several hundred times that of high explosives [2].

Kinetic energy deflections have been determined to be adequate against broad classes of threat objects, including the fairly frequently-encountered intermediate-sized objects that cause tsunamis [7]. This plus the existence of a strong technical basis for interceptor design and operation, along with the advantage of avoidance of political ramifications associated with the use of nuclear devices in space combine to make kinetic deflections fairly attractive as a near-term option. Still, even with the success of the Deep Impact mission, a decision to focus planetary defense system development exclusively on a kinetic intercept option would be a difficult one to make, as specific energies of nuclear devices are three orders of magnitude greater than that available from a kinetic intercept, an advantage that would be difficult to abandon.

A deflection method closely related to the purely-impulsive nuclear and kinetic options and one that merits mention because of its conceptual simplicity is that of pushing a threatening asteroid with a current-technology rocket motor. Figure 2-6 shows the relation of propellant mass to threat object diameter for a 1 cm/s change in threat velocity, which is generally accepted by the planetary defense community as the level of velocity change achievable in the near term by way of kinetic impact or nuclear means

[2]. The threat object was assumed to be made of rock at 3000 kilograms per cubic meter, and engine specific impulse was assumed to be 460 seconds, approximately that of a Space Shuttle main engine. The horizontal line denotes the propellant capacity of one Shuttle external tank.

Figure 2-6: Propellant Required for Rocket Engine Deflection of a Threat Object



If one external tank's worth of propellant is any measure, a 1 cm/s deflection seems to be fairly achievable (or at least not horribly unreasonable) even for objects up to 600 meters in diameter. However, there is still the consideration of the enormous propulsive, guidance, control, and remote operations challenges of getting an engine, its attending structure, and that much propellant first into Earth orbit, then accelerating it out to and decelerating it at the threat object, then getting it landed, assembled, and operating on the surface of a rotating or perhaps even tumbling object, all in a reasonable amount of time.

This task appears especially challenging when it is remembered that the Shuttle uses essentially all of that three-quarters-of-a-million kilograms of external-tank propellant plus two very powerful solid-propellant strap-on rockets just to get itself to orbit.

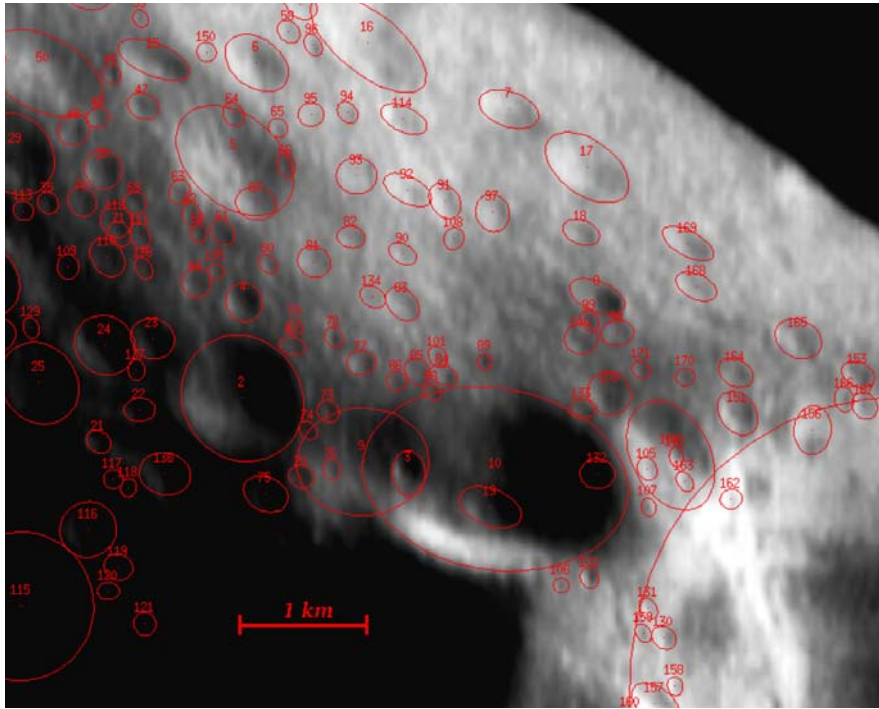
2.8 Threat Structure and Response

Having convinced ourselves at least for the purposes of this discussion that some sort of preventive action is the appropriate response when an Earth impact threat is identified, and having discussed several ways of depositing into a threatening object effective levels of deflection energy, it becomes necessary to consider threat object structure and its effect on how the threat can be expected to react to our efforts.

The common assumption of asteroid structure is that of a solid mass of rock, metal, or perhaps some fusion of the two. Fairly large specimens have been encountered that, upon the closest possible examination, indeed appear to be single pieces of rock, one of these being 33-kilometer-long Eros, one of only two asteroids onto which a spacecraft has successfully landed [13]. It is more likely, however, that any randomly selected asteroid might better resemble a flying pile of rubble [30]. The challenge presented by such objects is that when you deposit deflection energy into them you face the possibility of producing nothing more than a mild and ineffective dispersal, where the object absorbs the energy by simply reshuffling its parts or perhaps by dispersing them by a small and temporary amount. Depending on how much material and gravitational cohesive strength such rubble piles have, a series of smaller imparted velocities might be a more successful approach than attempting one big shove.

There is also a potential that even if a body appears to be monolithic, unseen weaknesses in the internal structure could give way under the force of an aggressive deflection attempt, likewise absorbing significant portions of the deposited energy. A catch 22 of the planetary defense trade space is that when imparted energy is increased in an attempt to gain margin in threat object displacement, there is a commensurate increase in the risk of adding too much energy and winding up with an object that does nothing more than distort by a small amount before proceeding on to a full and devastating Earth impact. That said, many asteroids have been found to have on their surfaces relatively large impact craters, indicating that they have already had deposited into them and, more importantly, *survived* some fairly extreme energies. One example is the aforementioned Eros. Figure 2-7 shows where NASA scientists have marked the locations and sizes of impact craters on what is only a small piece of the asteroid's surface. (Note the 1-kilometer size scale.)

Figure 2-7: Highlighted Impact Craters on Eros [20]

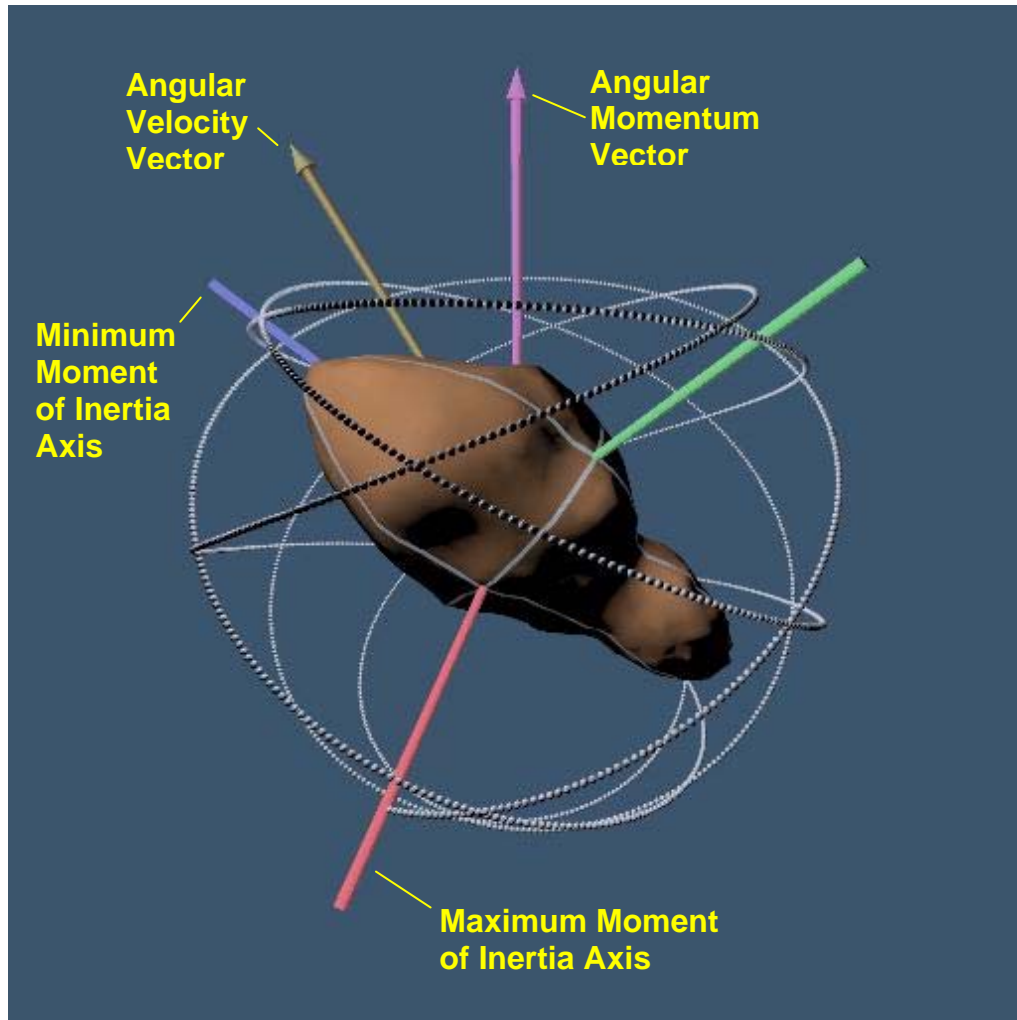


Comet structure, as was the case with comet surveillance, is more problematic. First, because comets are aggregates of rock and frozen gases, their base materials are inherently weaker than those of monolithic stone and metallic asteroids. Also, they are thought to suffer the same potential structural faults as do asteroids, making them additionally vulnerable to fracture and dispersion when undergoing a deflection event. However, this situation may have a positive side, as it may be that the softer cometary materials will be more easily separated from the host body in the form of ejecta, theoretically producing more impulse for a given kinetic or nuclear energy deposition and perhaps evidenced by the enormous debris cloud produced by the Deep Impact event [14]. Likewise, it would seem that directed energy techniques (again, laser or focused sunlight) would be more successful at vaporizing the methane and water ices of a comet than they would be at vaporizing rock or stainless steel, and thus would be capable of

producing higher thrust levels against a comet than against an asteroid. All of this is encouraging, but much more encouragement will be needed against a cometary impactor, as it will likely be larger than and will almost certainly be approaching faster than an asteroid threat.

With threat object structure and composition accounted for, the next challenge in the design of a deflective mitigation mission is to account for the offending object's rotational behavior. Many asteroids spin about their axis of greatest moment of inertia, which is certainly expected if they have internal structures that dissipate energy (i.e., if they are rubble piles). However, while consistent with the laws of rigid-body motion, single-axis rotation cannot be taken as proof positive that an object is actually fragmented. Further, it is by those same laws that more solid threat objects of truly irregular shape are in general not principal axis spinners: they tumble. Figure 2-8 shows the asteroid 4179 Toutatis, a 4.6-kilometer-long object that was the subject of an Earth-based radar examination. Resulting theories vary as to its exact internal structure. It may have a smaller object strongly but still only gravitationally attached to a larger parent body or it may be a single piece of rock that underwent some very selectively-shaping impacts. Whatever its internal makeup, Toutatis exhibits markedly non-principal-axis motion. The small spheres shown encircling the object in Figure 2-8 trace the path of the body-fixed, maximum moment of inertia axis, with one dot applied every 15 minutes for a total of 20 days. Counting the spheres to determine the body's rate of rotation would be a waste of time: the path that the Sun takes through the Toutatis sky never repeats itself, so the concept of a constant-length Toutatis "day" has little meaning [39].

Figure 2-8: Rotational Motion of Toutatis



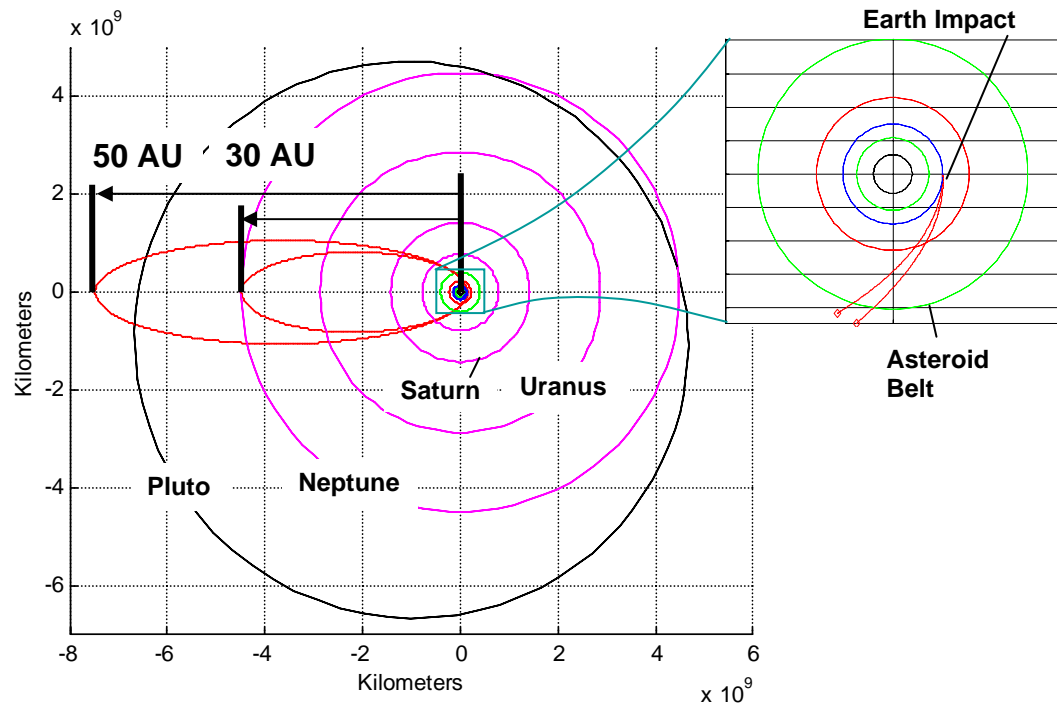
The implications of a tumbling asteroid target are severe. In order to ensure that imparted deflection energy produces the maximum possible displacement of the threat object (as opposed to wasting a portion of that energy in simply altering the body's spin state), the line of action of the deflection force must be made to pass directly through the body's center of mass. Because a tumbling body presents to an approaching interceptor a constantly-changing scene of apparently random new topographies, the timing of the interceptor's arrival and selection of the final aim point present a significant challenge,

especially when the closing velocities are likely to be many tens of kilometers per second. It is not just threat mass distribution or topography, however, that will cause concern. Many asteroids have been determined to have moons orbiting them, and some asteroids are actually two similarly-sized, self-orbiting but unconnected bodies [48], further complicating the task facing what would have to be at least a semi-autonomous interceptor.

2.9 Near Earth Object Orbits: Comets

The simplest short-period comet orbits that dip low enough to become of concern to this discussion (i.e., those that satisfy the criteria for NEOs of having perihelia less than 1.3 AU) will often maintain their originating aphelia in the Kuiper Belt, somewhere between 30 and 50 AU. In order to be able to reach down toward the Sun just enough to strike the Earth at 1 AU, the mathematics of conic sections dictates that their eccentricities be approximately 0.9355 and 0.9608, respectively. These two extremes are shown in Figure 2-9. The inset shows the geometry of approach to Earth impact taken by these two threats.

Figure 2-9: Common Orbits for Short Period Comets



When comets from the Oort Cloud are considered, the characteristics of conic sections push eccentricities even closer to unity. If an Oort object originating from a nominal 1-light-year circular orbit enters an elliptical orbit that brings its perihelion down to exactly 1 AU, the resulting eccentricity would be approximately 0.9999683. To enter this orbit, however, the object would have to lose nearly all of its circular orbit velocity; some random interstellar perturbation will have to slow it from approximately 118 m/s down to approximately 67 cm/s. By observation of the relative rarity of inner-planet cometary passage, it might be deduced that such perturbing interactions do not often happen. It may also be that they do not often happen with sufficient accuracy: if some perturbing force aims to accomplish just the velocity reduction from 118 m/s to 67 cm/s required to achieve an Earth impact by way of an elliptical orbit, but happens to fall short

by only 1%, the resulting perihelion would be at approximately 350 AU, well beyond the outer rim of the Kuiper belt.

Direct passage to the inner planets from the Oort Cloud or Kuiper Belt, regardless of the earlier deduction, is not the only mechanism by which comets can come to threaten the Earth. If the aforementioned perturbing force was a bit more accurate and came to within 1% of the required velocity change, the Earth would still be safe from a direct trajectory impact, but at perihelion the threat object would find itself at about 7.5 AU, between the orbits of Jupiter and Saturn. Just as the gas and ice giants, especially Jupiter, drove into exile the comets of the early solar system, they likewise often drive the dynamics of such returning comets, pulling them from their otherwise intended paths, often dramatically. Such was the case for the aforementioned comet Shoemaker-Levy-9, which entered Jupiter's gravitational influence perhaps as late as 1970 but did not succumb completely by way of impact with Jupiter until half way through 1994 [22]. Had the comet originally entered Jovian space on a slightly different path or with slightly different timing the result of the first encounter might easily have been a foreshortened heliocentric path across Earth's orbit.

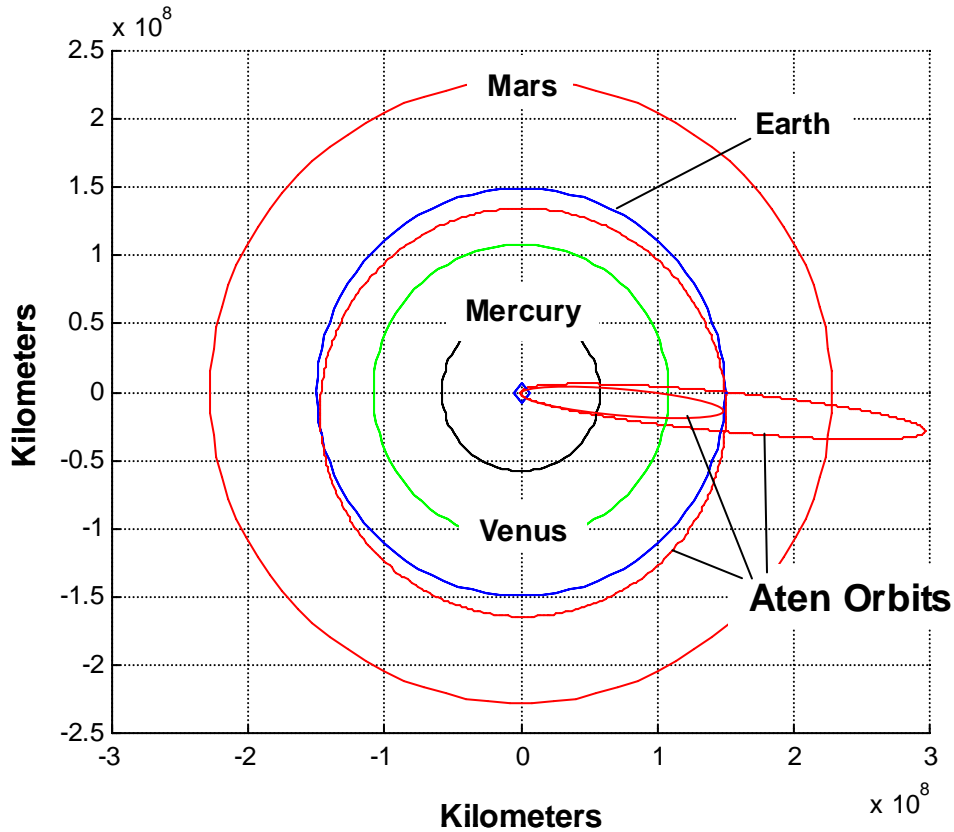
2.10 Near Earth Object Orbits: Asteroids

Thankfully, Sun-approaching comets spend the vast majority of their time well away from the Sun and thus well away from Earth. Even when they transit the orbits of the gas and ice giants, those planets have such large periods that the probability of a meaningful encounter is quite small. Near-Earth asteroids, however, residing as they do almost exclusively among the higher-paced inner planets, can encounter planetary gravitational

fields much more frequently and thus have a much greater chance of being forced into complex and perhaps threatening orbits. Further, such encounters do not have to produce radical orbit changes to be of interest. As mentioned earlier, errors in estimates of known gravitational influences along with unknown influences cause extended predictions of threat position to become extremely inaccurate. Although longer-term calculations are often made as in the case of the aforementioned asteroid 2004 MN4 and its close-Earth passage in 2029 (about 27 threat orbits from now), a more conservative projection would expect to hold accuracy up to only about 10 threat orbits [27].

In spite of the potential for perturbing encounters, the prediction of an asteroid's motion is quite correctly generalized in terms of a regular, repeating, heliocentric orbit. Those objects with orbits that qualify them as NEOs are placed into one of three distinct orbital groups: Atens, Apollos, and Amors. Atens (named after asteroid 2062 Aten) have the smallest possible orbits for objects that are still considered to be NEOs. They are distinguished by semi-major axes that are smaller than that of the Earth, but they have aphelia greater than 0.983 AU, the smallest Earth-to-Sun distance on our planet's not-quite-circular orbit. Atens are also notable because with periods of less than one year (dictated by the semi-major axis constraint), they spend most of their time inside Earth's orbit, making them more difficult to spot due to the solar exclusion restrictions of ground-based surveillance systems. The extremes of allowable Aten orbits are shown in Figure 2-10.

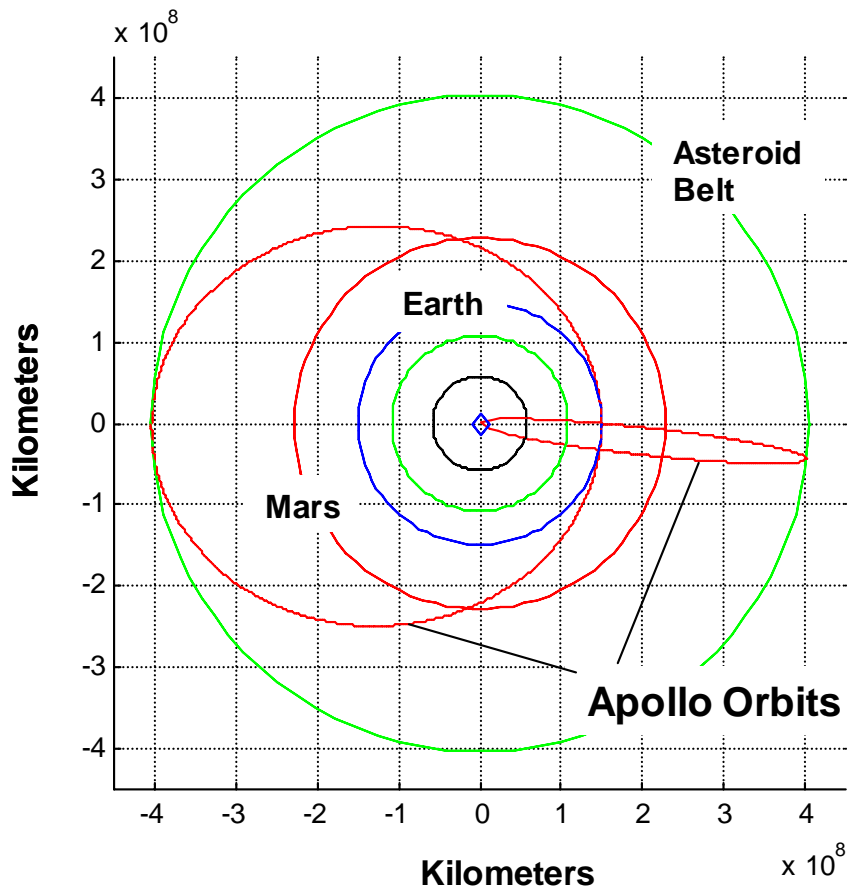
Figure 2-10: Extents of Example Aten Orbits



The larger of the two elongated Aten orbits has an eccentricity of slightly over 0.9953, resulting in an aphelion of slightly less than 2 AU. Higher eccentricities are mathematically allowed, but would place the object's perihelion inside the radius of the Sun. The smaller but still highly-eccentric ellipse represents an orbit reaching just to the 0.983-AU limit. The more circular orbit represents an Aten that is essentially co-orbiting with the Earth. (The orbit plot shown is actually slightly more eccentric than mathematics dictates, but was chosen so as to provide a visual separation from Earth's orbit at this scale.)

An asteroid with an orbit that reaches just beyond that of the Atens, which would make its period equal to or greater than that of the Earth, is termed an “Apollo,” after asteroid 1862 Apollo. As the period constraint implies, these objects have semi-major axes greater than or equal to that of Earth, but their perihelia are restricted to be less than or equal to 1.017 AU, the farthest distance that the Earth attains from the Sun. Representative Apollo orbits are shown in Figure 2-11. Note that the view is still from above the ecliptic, but it is now from a point that is farther away from the Sun so as to see more of the inner solar system.

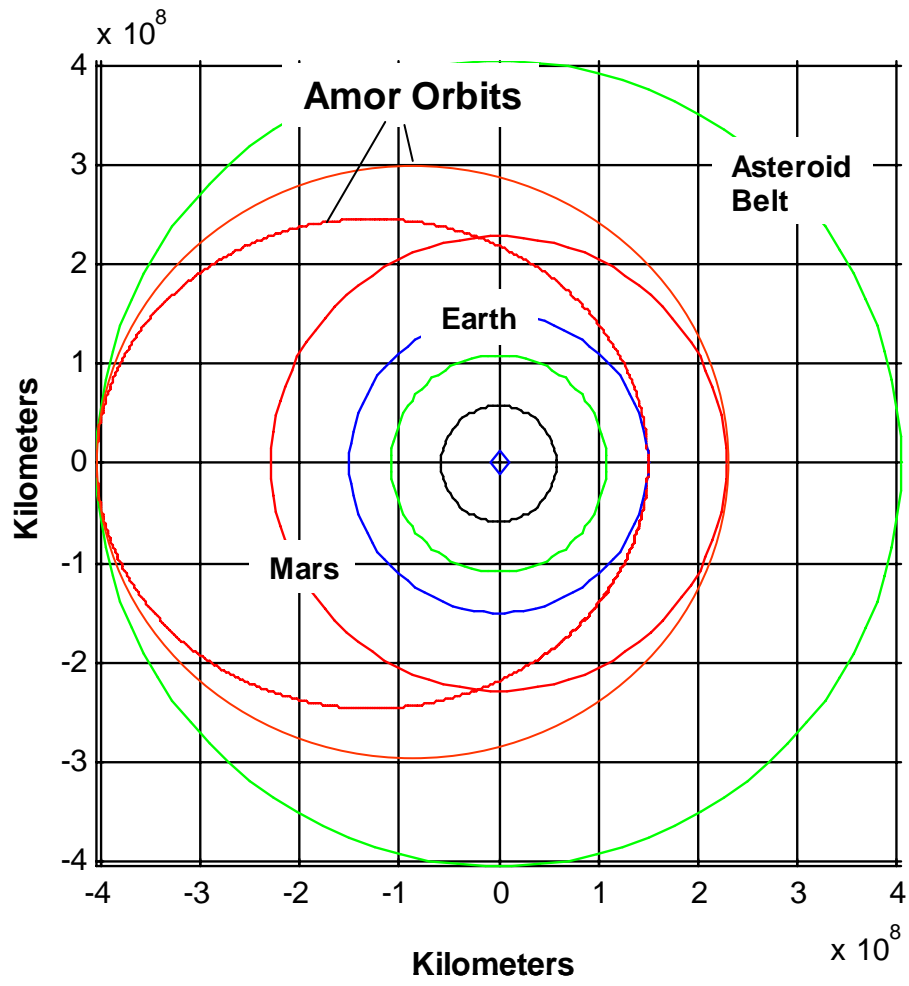
Figure 2-11: Range of Example Apollo Orbits



By virtue of their perihelion-based definition, Apollos can have theoretically infinitely large aphelia. However, the probability is very small that any object that starts its life in the Asteroid Belt will experience the complex sequence of gravitational encounters necessary to achieve extremely large aphelia. The objects in Figure 2-11 represent two limiting cases for an Apollo population with more reasonable orbits; each is shown to reach out to but go no farther than the Asteroid Belt, giving additional emphasis to the Belt as the source for the threat objects in question. For the more eccentric of the two examples, $e = 0.996$ (limited by the Sun's radius); for the moderately-elliptical orbit, $e = 0.453$. If this particular object's eccentricity was any smaller, its perihelion would rise above the 1.017-AU limit, making 0.453 the approximate lower limit on eccentricity for Apollos originating in the Belt. That said, many Apollos exist that do not have their aphelia in the Asteroid Belt, and these do possess eccentricities below 0.453. If that eccentricity is reduced further, aphelia drops and eventually a lower limit is met where Apollos have orbits almost identical to but lying just outside that of the Earth.

The third and final category of NEA is the "Amors," all of which have their perihelia lying strictly between the orbits of Earth and Mars (i.e., between 1.017 AU and 1.3 AU). Named after asteroid 1221 Amor, such objects have no limit on aphelia, as was the case with the Apollos, but more typical Amors have their aphelion in or near the Asteroid Belt, as shown for the two orbits in Figure 2-12. These two objects would be Amors of great concern, as their perihelia bring them perilously close to Mars or Earth, increasing the risk of a destabilizing encounter or a terrestrial impact.

Figure 2-12: Representative Amor Orbits



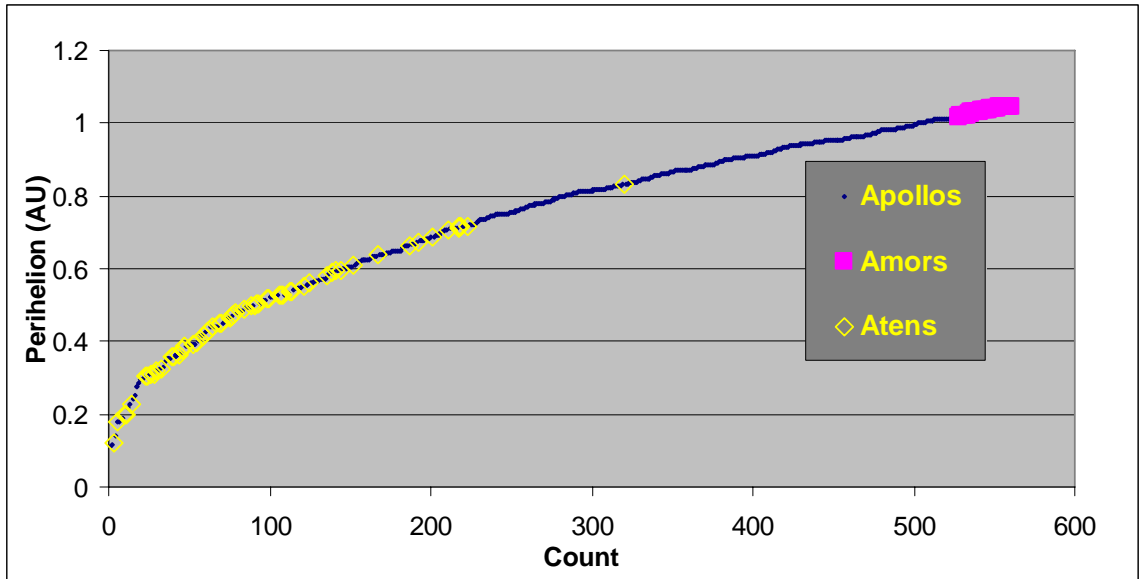
Chapter 3 - Mitigation Modeling

3.1 Representative Threat Set

In general, regardless of whether the threat in question is planetary in nature or otherwise, a parametric, representative threat set is desirable to assure a broadly-applicable assessment of defense system performance. In order to be sufficiently representative, that set must cover a broad portion of the observed threat, but must not draw the performance analysis too far into low-probability excursions. To this end, because comet impactors have been deduced to be much rarer (as was discussed in the previous chapter and by observation), a representative asteroid threat set was developed as the focus of this paper. The cometary threat will be addressed, but by specific cases only. The goal is not to shy away from a difficult portion of the threat, but rather to address a more numerous and more frequently-seen portion of it, and one wherein there is at least a possibility of successful near-term mitigation.

A representative asteroid threat set was created by assessing orbital element distributions obtained from actual observation data of PHAs – again, asteroids that can pass within 0.05 AU of the Earth, of which 662 were known as of the completion of this analysis [28]. Figure 3-1 begins this process by showing the full distribution of observed perihelia for all known PHAs, subdivided for clarity into Atens, Apollos, and Amors.

Figure 3-1: Distribution of Perihelia for Observed PHAs

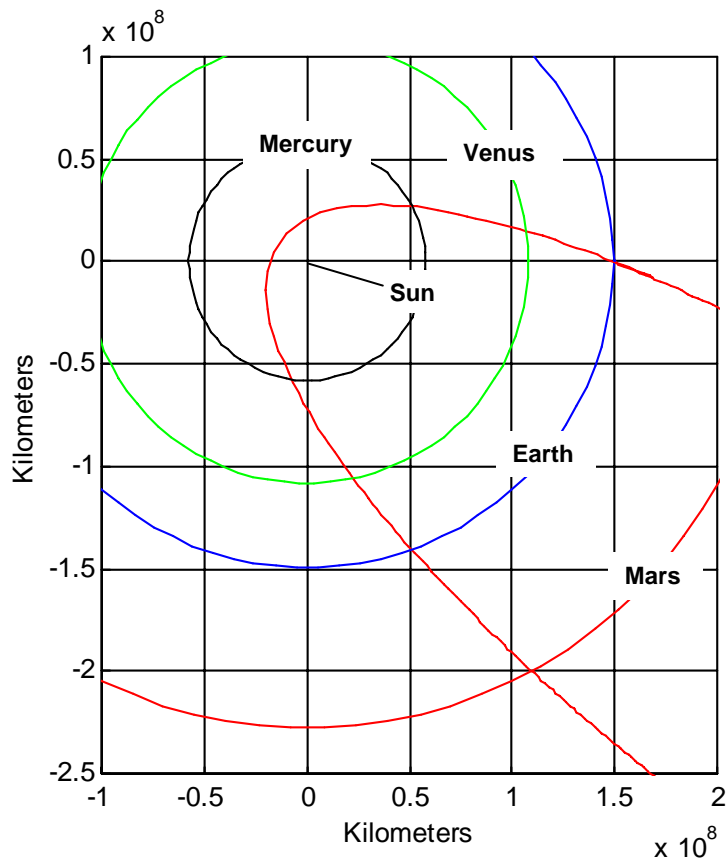


Of immediate note is that the PHAs depicted in Figure 3-1 do not include all existing Amors. While Amors are permitted to possess perihelia out to 1.3 AU, those with perihelia beyond approximately 1.05 AU do not qualify as PHAs and so are not included in the threat set. Further, because of their perihelion-based definition, Amors should be and quite obviously do end up being segregated from the Apollos and Atens at the high-perihelion end of the scale.

At the low end of the scale there is a steady trail off of objects down toward what presents itself as a “functional” perihelion limit of about 0.093 AU. Note, however, that there is no immediately obvious reason that this particular perihelion value, which belongs to asteroid 2004 UL as shown in Figure 3-2, should be a limit. The perihelion of 2004 UL is not coincident or even nearly so with the orbit of any planet (the figure shows that this object crosses well inside of Mercury’s orbit), and it is well outside the Sun’s radius, which, at about 1/90 the diameter of Mercury’s orbit, would not quite be visible

on the scale of this figure. As was the case with potential orbits for long-period elliptical comets, part of the reason for the lack of objects with perihelia smaller than 2004 UL's is the extremely low probability that an object will randomly happen upon the exacting gravitational encounters needed to place it into the narrow orbital corridor bounded by on the high end by perihelia of 0.093 AU and on the low end by orbits that pass within the radius of the Sun. Figure 3-2 shows the rather extreme eccentricity that 2004 UL had to adopt to achieve as low of a perihelion as it did. In fact, at $e = 0.927$, this object also has the third highest eccentricity of all observed PHAs.

Figure 3-2: Inner Orbit of PHA 2004 UL



The distribution of aphelia values within the PHA population is similar to that displayed by perihelia. While Amors and Apollos are moderately well scattered across the range of possible values, Atens are restricted by conic section mathematics to values below 2 AU (actually, below approximately 1.995 AU to account for the Sun's radius). However, as seen by the Aten data points in Figures 3-3 and 3-4, the workable aphelia upper limit exhibited by that portion of the threat is approximately 1.7 AU. The actual figure is 1.696 AU, possessed by asteroid 1995 CR, which, as fits the pattern of a limiting-case threat, also possesses the largest eccentricity of all hazardous Atens ($e = 0.869$). These trends are best seen in Figure 3-4, which excludes the single outlying object from Figure 3-3 so as to give a more appropriate scaling.

Figure 3-3: Distribution of Aphelia for Observed PHAs

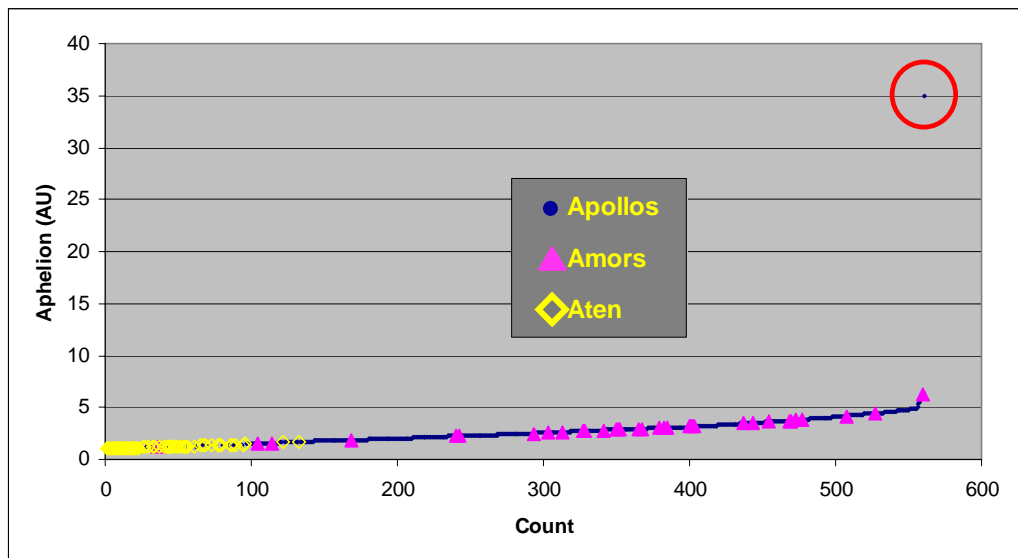
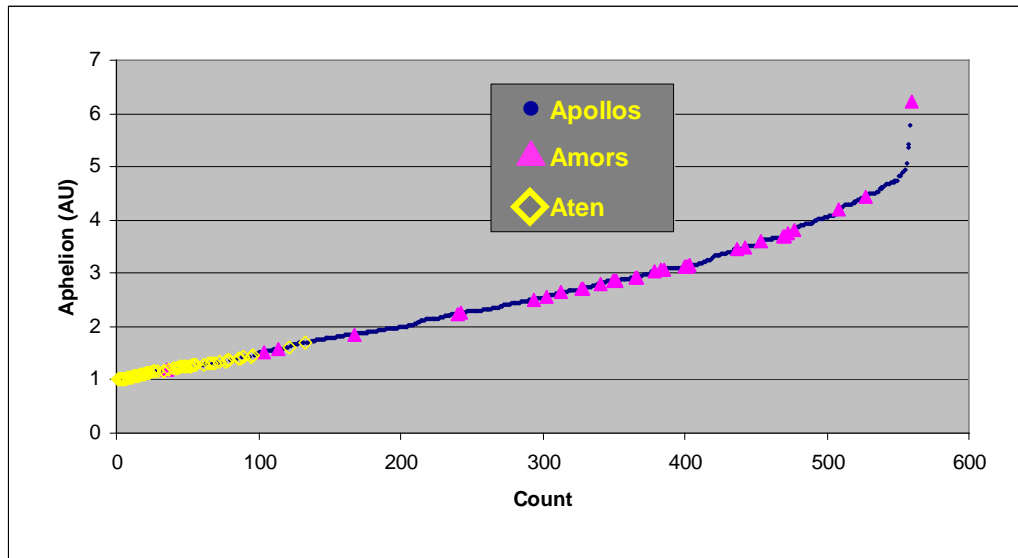


Figure 3-4: Distribution of Aphelia for Observed PHAs Less Outlier



Regarding the aforementioned outlier, it is the Apollo designated 1999 XS35, and has a period of a little over 76 years with an aphelion of over 34 AU. Its orbit, viewed from above and then at a more oblique angle, is plotted in Figures 3-5 and 3-6, respectively. While this object has never been known to exhibit a tail, it has all the orbital characteristics of the depleted core of a short-period comet, but, because it has a perihelion of 0.952 AU, it is classified as an Apollo “asteroid.”

Figure 3-5: Orbit of Apollo 1999 XS35 Looking Down on Ecliptic

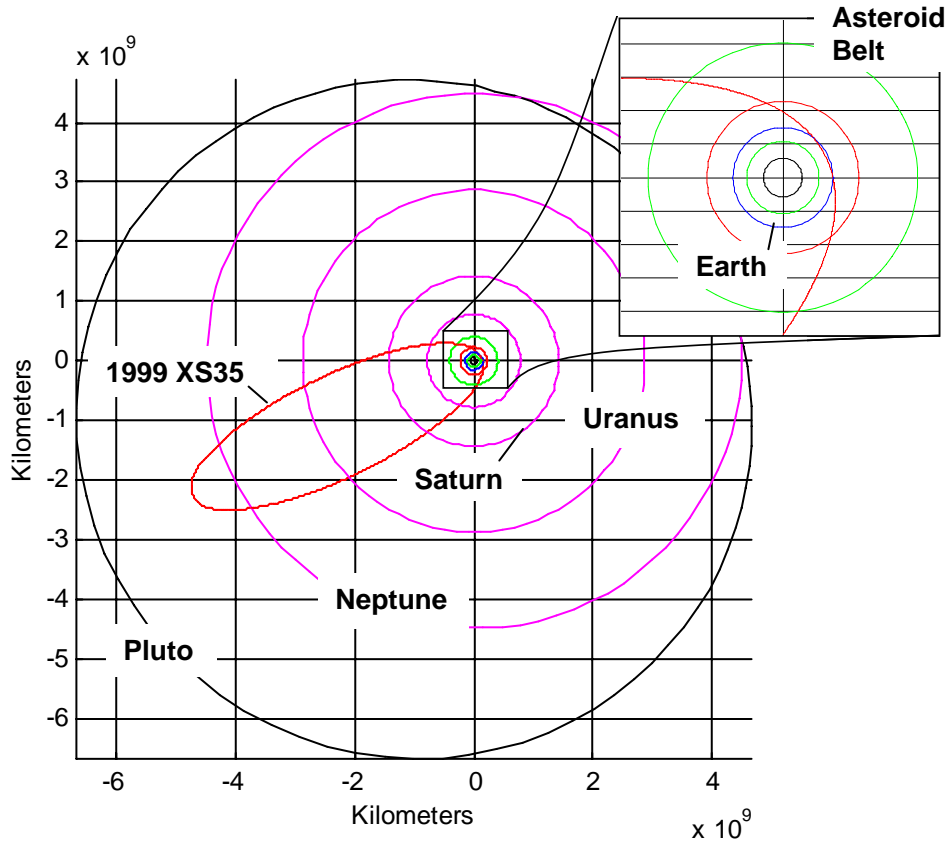
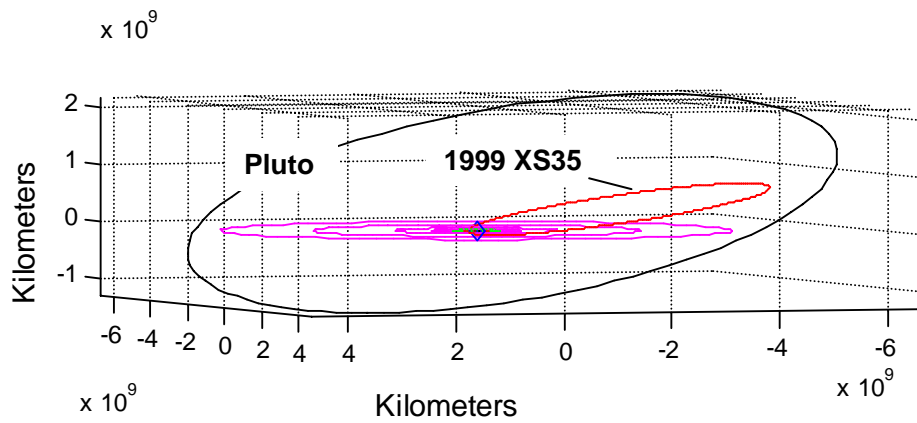
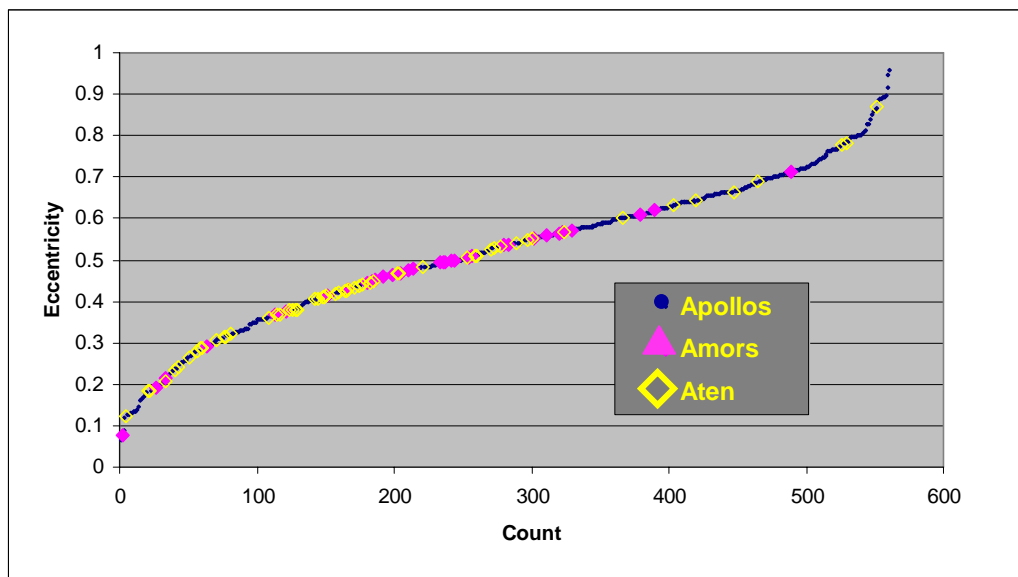


Figure 3-6: Orbit of Apollo 1999 XS35 – Oblique View



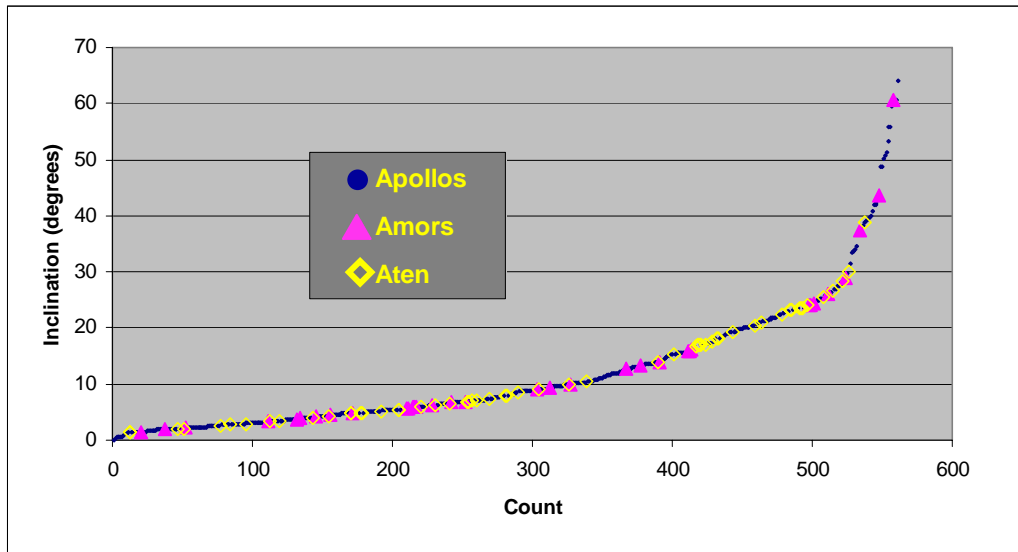
Eccentricity is the best behaved of the PHA elements. Its distribution, shown in Figure 3-7, even takes on the recognized shape of a true cumulative distribution curve and exhibits a fairly even population along the continuum of possible values. Each of the three threat types likewise has modestly broad representation, clumping mostly around the values at the middle of the scale and thinning out as values become more extreme.

Figure 3-7: Distribution of Eccentricity for Observed PHAs



Finally, Figure 3-8 shows the distribution of observed PHA inclinations, which, as with eccentricity, is rather well behaved, being moderately smooth along the continuum of possible values and having broad representation among the three PHA categories.

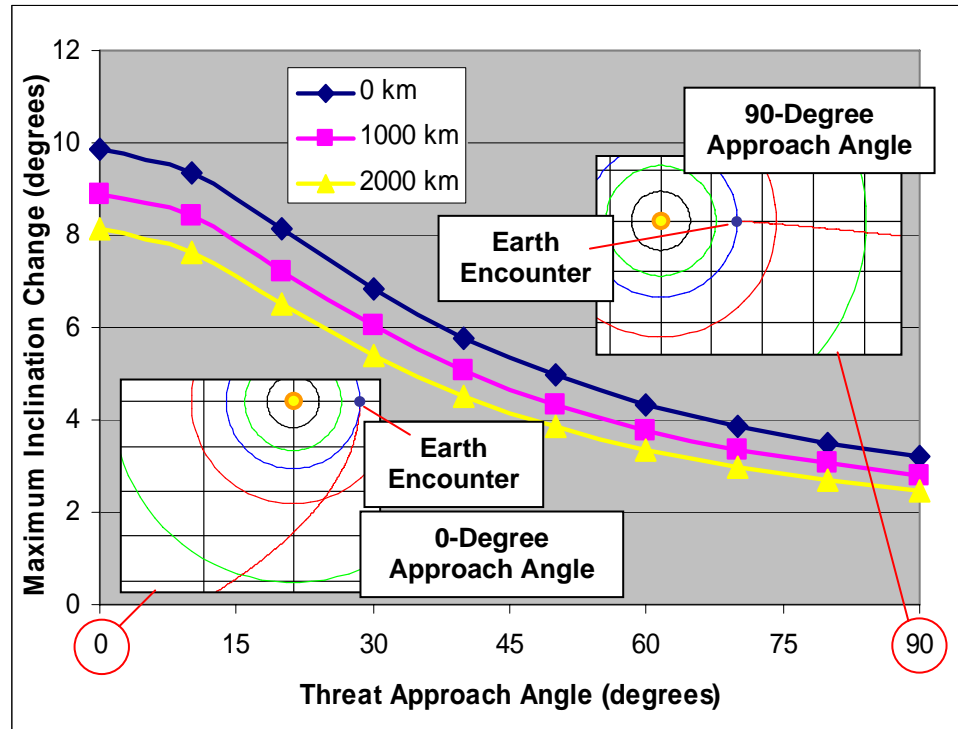
Figure 3-8: Distribution of Inclination for Observed PHAs



Note that the inclination curve becomes sparse only in its extreme upper regions, and understandably so, as the higher an asteroid's inclination, the more intense the gravitational encounter or encounters must have been in order for it to have suffered so radical a change in its orbital plane. Such extremely intense encounters themselves require very close but, of course, non-colliding passage to the perturbing body. The lowest possible heliocentric velocity for an Earth-encountering object is approximately 2.9 km/s for an object with an aphelion of 1 AU and a perihelion at the radius of the Sun. For this extreme case, the maximum inclination change from an atmosphere-skimming Earth encounter is just over 53 degrees. However, taking the limits of the observed PHAs as a measure of more nominal objects, the maximum inclination change drops to approximately 17.7 degrees, indicating that single-encounter plane changes to high inclination should be rare, and that additive series of smaller encounters should be exceedingly rare, especially since inclined objects spend most of their time away from the

ecliptic and therefore likewise away from the planetary causes of these gravitational encounters. For the comet threat, available inclination change is also small, as seen in Figure 3-9. This gives the maximum inclination change attainable by way of an Earth encounter for a posigrade Kuiper object originating at 50 AU. The “Threat Approach Angle” is a measure of the threat’s velocity vector direction as it approaches the Earth: an approach angle of 90 degrees corresponds to a threat moving essentially at the Sun, while 0 degrees corresponds to a threat that travels in the same direction as the Earth, overtaking it during the encounter. The smallest distance shown from Earth at hyperbolic passage is 6488 km, which accounts for the Earth’s radius plus 110 km of substantive atmosphere: this atmosphere-grazing passage is the “0 km” line in Figure 3-9, with the other plots lines giving attainable inclination change for incrementally-increasing altitudes.

Figure 3-9: Attainable Single-Passage Inclination Changes for a Kuiper Object Encountering Earth



To help complete the process of establishing the representative threat, histograms were developed to provide discretized approximations of the distributions just presented for perihelia, eccentricity, and inclination. Of note is that while the forthcoming analysis of post-deflection orbital behaviors deals with the full set of six elements, only these three are needed to define the orbits of interest, as will be discussed in more detail in the next section. These histograms are shown in Figures 3-10, 3-11, and 3-12, and were derived from the same hazardous object observations that were used to generate the referenced distributions.

Figure 3-10: Histogram of Radii of Perihelion for Observed PHAs

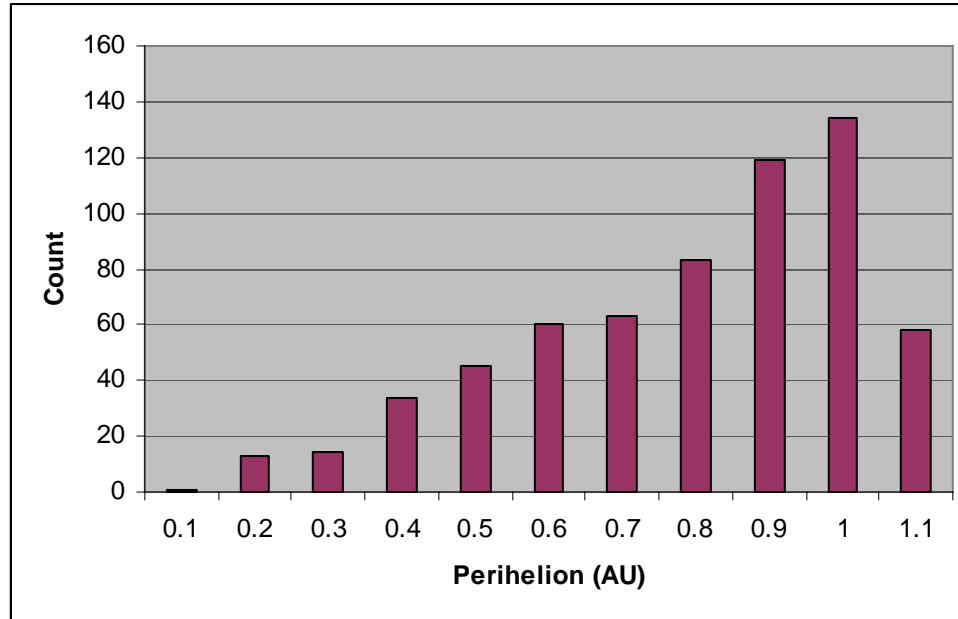


Figure 3-11: Histogram of Eccentricities for Observed PHAs

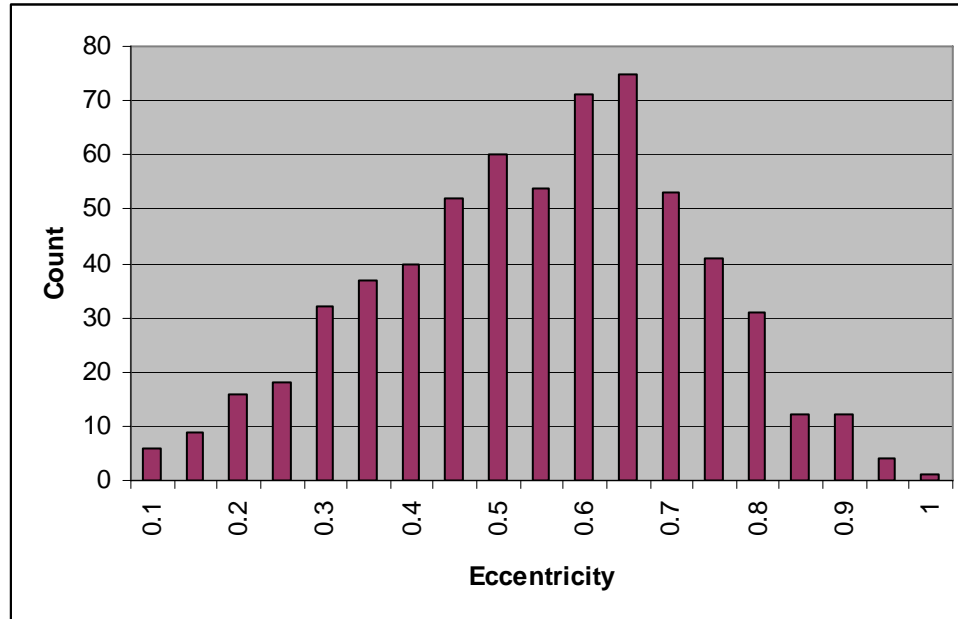


Figure 3-12: Histogram of Inclinations for Observed PHAs

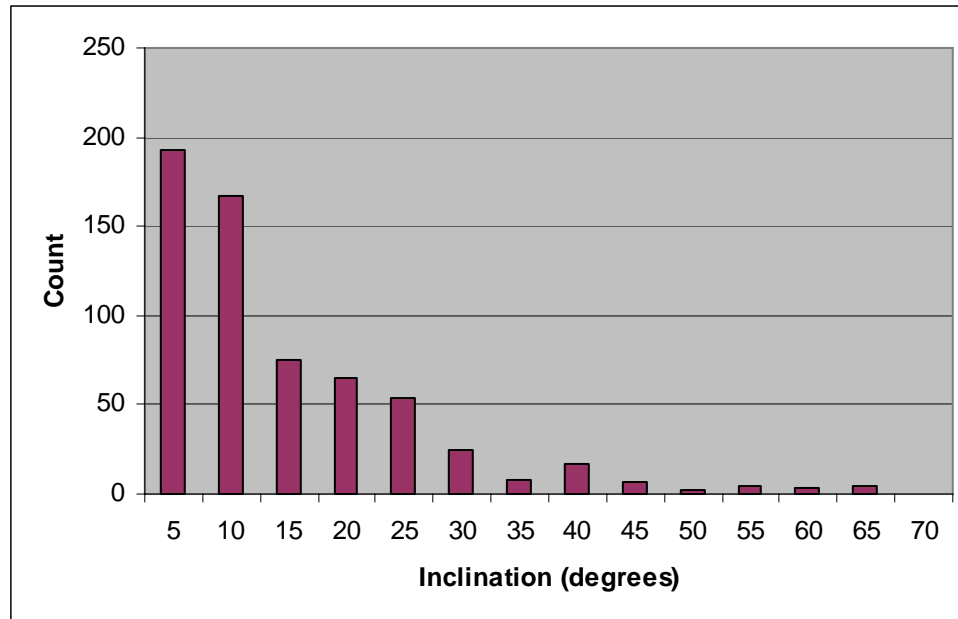


Figure 3-10 shows perihelion to fall off fairly steadily from a high population point at just above 1 AU to a low that approaches 0.1 AU, making system performance conclusions more readily applicable to threats at the higher end of the scale. The fall off in eccentricity in Figure 3-11 is roughly linear on either side of a central peak, showing a lessening of applicability at extreme values, both high and low. Finally, Figure 3-12 confirms that deflection behaviors particular to low-inclination threats are significantly more broadly applicable than those of threats with higher inclinations.

Based on the element distribution data presented earlier and the histogram trends just described, the bounding values and associated parametric step sizes contained in Table 3-1 were selected as the representative asteroid threat set for the analysis of threat system performance. That analysis will deviate from these bounds only to handle special cases such as when performance at the threat set boundary is explored.

Table 3-1: Asteroid Threat Orbital Element Extents

Orbital Element	Value Extents	Baseline Step Sizes
Radius of Perihelion	0.1 AU to 1.0 AU	0.1 AU
Eccentricity	0.1 to 0.99	0.1 + 0.99
Inclination	0 degrees to 70 degrees	0, 5, 10, 15, 25, 40, 70

Step size for perihelia and eccentricity are based on the observation that the distributions of these elements among observed PHAs was moderately well behaved so no drastic limitations in the use of those elements is indicated. As such, these two variables are handled with evenly-spaced step sizes. Inclination, however, displaying as it is in Figure 3-12 a rather non-linear trend toward zero at higher values, demands a slightly more specialized treatment. While high inclination values are included in the analysis, the selected parametric values are weighted toward the lower inclinations. Figures 3-13 and 3-14 show inclination behavior across the other two key orbital elements, where the increasing sparseness of object count with increasing inclination is obvious.

Figure 3-13: Scatter Plot of Eccentricity vs. Inclinations for Observed PHAs

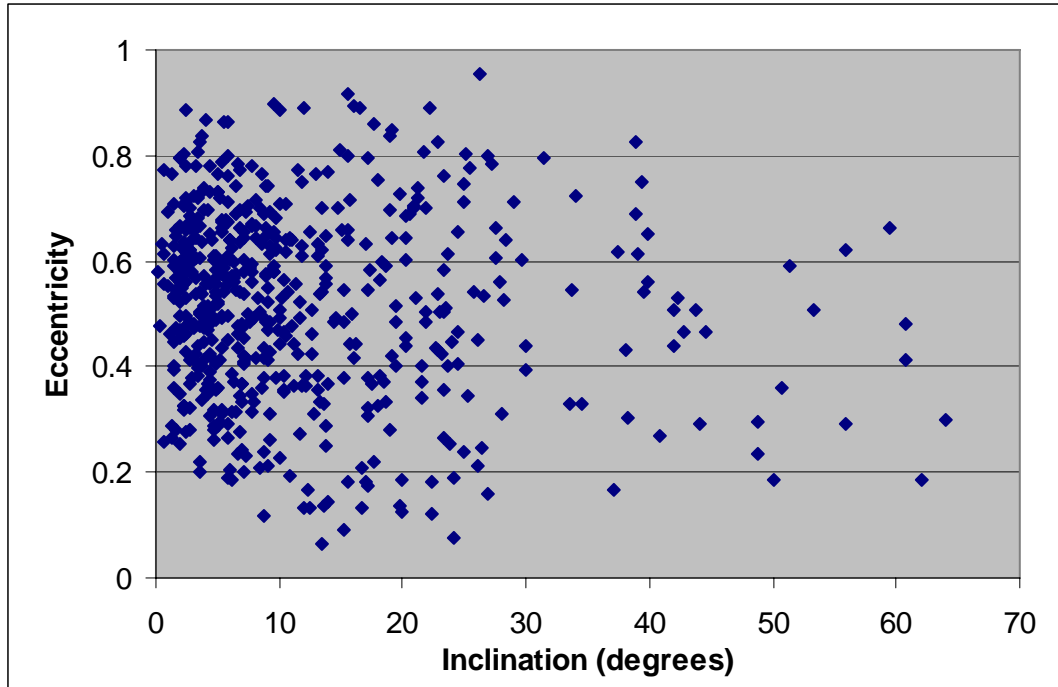
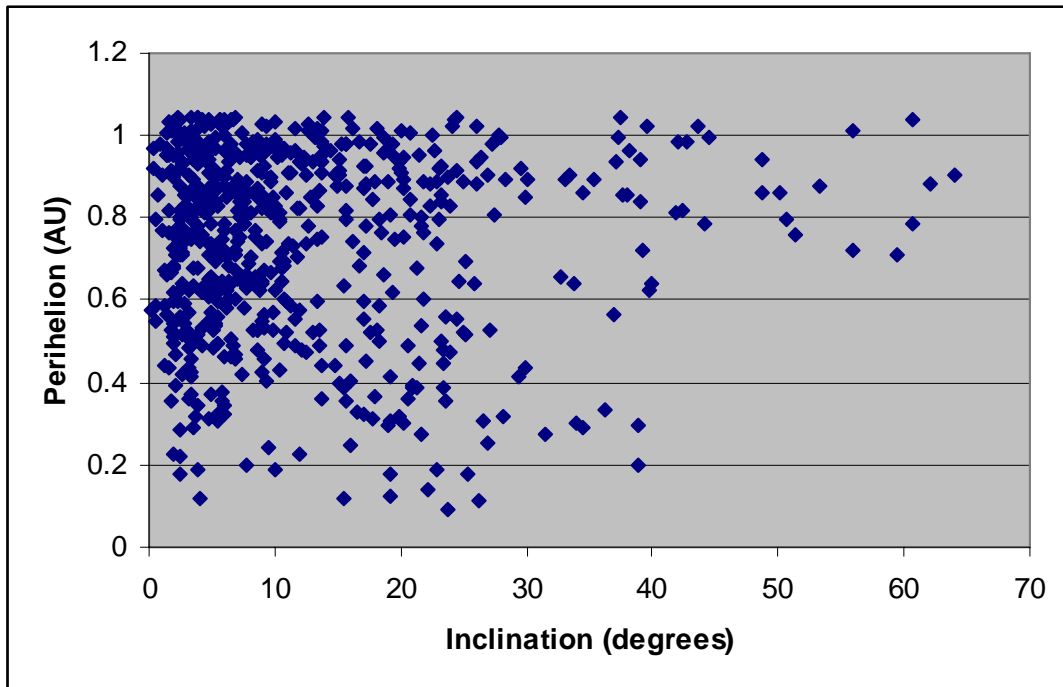


Figure 3-14: Scatter Plot of Perihelion vs. Inclination for Observed PHAs



3.2 Threat Displacement Simulation

Several bodies of work exist that make varied attempts at describing the post-deflection orbits and Earth-relative motions of impulsively-deflected threat objects. The earliest efforts, while applicable many orbits in advance of an impending Earth impact, were strictly linear in nature [2]. Extrapolated from circular-orbit solutions, these asserted merely that the velocity change to be inflicted on the threat object varied inversely with the amount of time left before that impact. A more complex, non-linear closed-form approach was developed to estimate near-optimal deflection solutions [12], but was not applicable more than one orbit prior to impact, and was further hampered by its inability to account for Earth's gravity. In addition, the threat reaction that was calculated was simply the object's displacement relative to its pre-deflection position: Earth motion around the Sun was not accounted for in determining the offset distance. A subsequent work, however, was successful at developing numerical solution techniques for estimating minimum required velocity changes for engagements occurring many threat orbits prior to Earth impact [41]. While this work did discover the finer structure that exists in the deflection data (as will be discussed in detail in Chapter 4), Earth gravitational effects were still neglected.

The simulation codes developed for this paper were designed to be more accurate and more broadly applicable than the historical efforts, although the historical work was valuable to a successful benchmarking of the codes. Increased accuracy was attained through a modeling of the aforementioned Earth gravitational effects, where the Earth-to-Sun gravitational sphere of influence is that suggested by Laplace, as shown in Equation 3.1 [6]:

$$R = D \left(\frac{m_{Earth}}{m_{sun}} \right)^{2/5} \quad (3.1)$$

In this equation, R is the sphere of influence radius, D is the distance between the Earth and the Sun (i.e., 1 AU), and the Earth-to-Sun mass ratio is as shown. The resulting Earth-to-Sun sphere of influence has a radius of just less than 925,000 km or about two and a third times the Earth-Moon distance.

Multi-orbit heliocentric solutions were attained through iterative numerical solution of Kepler's Equation, shown as Equation 3.2 [43]:

$$t_2 - t_1 = \sqrt{\frac{a^3}{\mu}} [E_2 - E_1 - e(\sin E_2 - \sin E_1)] \quad (3.2)$$

The left side of this equation is the time from deflection to that of Earth impact, a is the threat orbit's semi-major axis, μ is the Sun's gravitational parameter (equaling, by definition, the Sun's mass multiplied by the Universal Gravitational Constant), E is the threat orbit's eccentric anomaly at the times of interest, and e is the threat orbit's eccentricity.

The Kepler solution itself was carried out by Newton iteration wherein one side of Equation 2 was subtracted from the other and designated to be $F(E)$, a function of eccentric anomaly E . The derivative of this function was then taken and designated $F'(E)$, and values of E were iteratively substituted in and solved for according to the construction shown in Equation 3.3 [43]:

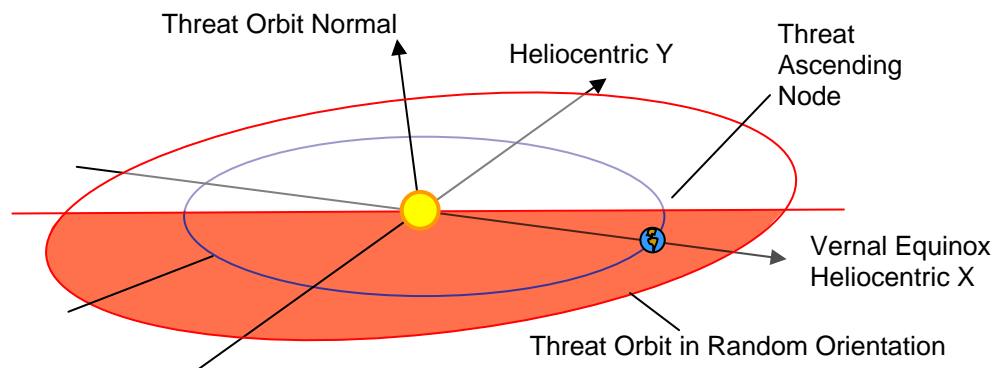
$$E_{k+1} = E_k - \frac{F(E_k)}{F'(E_k)} \quad (3.3)$$

The subscripts track the relation between functional values of the current ($k+1$) and the previous (k) iteration step. The solution was assumed to be converged when subsequent iterations closed to within a tolerance of 1×10^{-8} , producing a maximum positional error of less than 1 km at 1 AU. It should be noted that while numerical solutions of Kepler's Equation suffer instabilities for eccentricities approaching unity and that several approximating procedures exist that do not suffer such instabilities or at least suffer them less badly, it was determined during the development of the simulation codes that the eccentricities associated with the threat orbits of immediate interest do not cause such difficulties over the selected span of the representative threat set.

The simulation itself, which is described in greater detail in Appendix B, begins with the selection of values for the three key threat orbital elements of interest described earlier: perihelion radius (rp), eccentricity (e), and inclination (i). Characteristics of the velocity change that is be imparted to the threat object are also selected, such as its magnitude, its direction, and the time before Earth impact at which it will be applied. Orbital modeling begins as shown in Figure 3-15, with placement of the Earth at autumnal equinox, selected because of convenience of sign convention: this point is located at an assumed 1 AU out along the direction of the *vernal* equinox, which, conveniently, is the positive-X direction of the heliocentric inertial Cartesian coordinate system. Because threat orbital elements are selected parametrically, no reduction in the applicability of the representative threat set is suffered from ignoring the slight eccentricity of Earth's orbit.

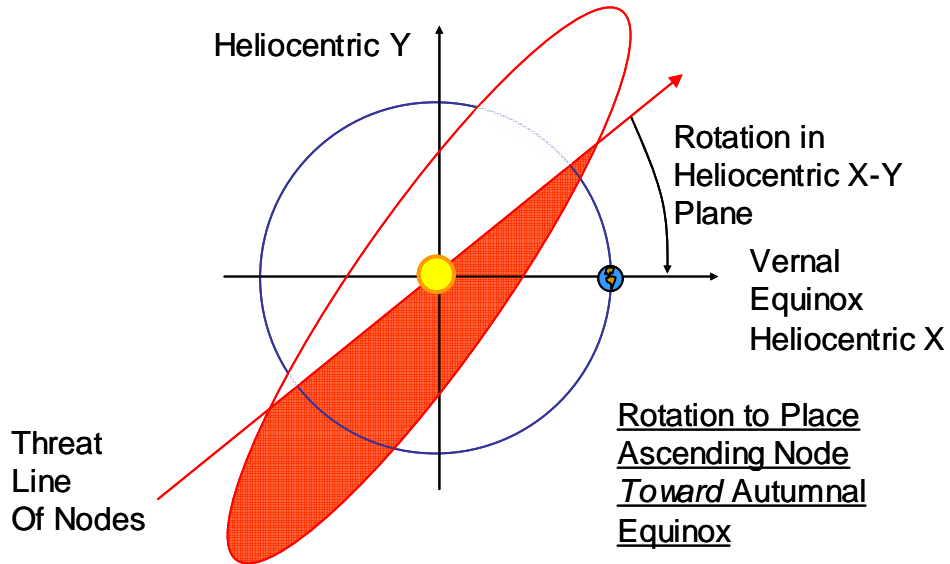
Next, conic equations are applied to calculate threat semi-major axis and radius of aphelion, with the threat's orbit at this point still in essentially a random orientation. The shading of the threat orbit indicates the portion that is below the ecliptic.

Figure 3-15: Representation of Process for Generating an Earth-Impact Threat: Step 1



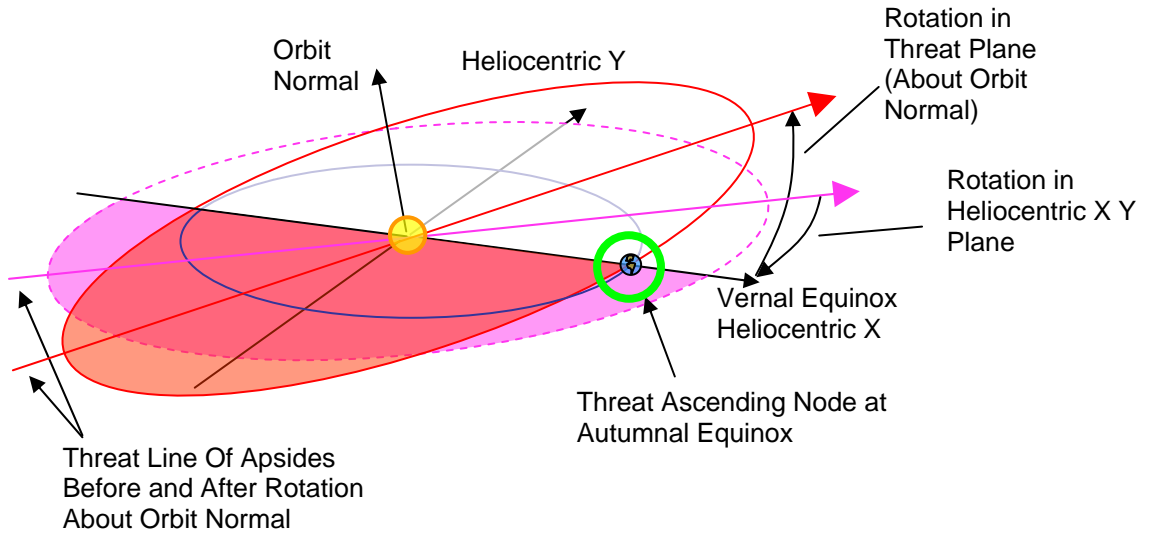
With the threat orbit size, shape, and tilt thus determined, the inertial orientation required for Earth impact is then established by rotating the orbit in the heliocentric X-Y plane so as to place ascending node along the direction of vernal equinox, as shown in Figure 3-16.

Figure 3-16: Representation of Process for Generating an Earth-Impact Threat: Step 2



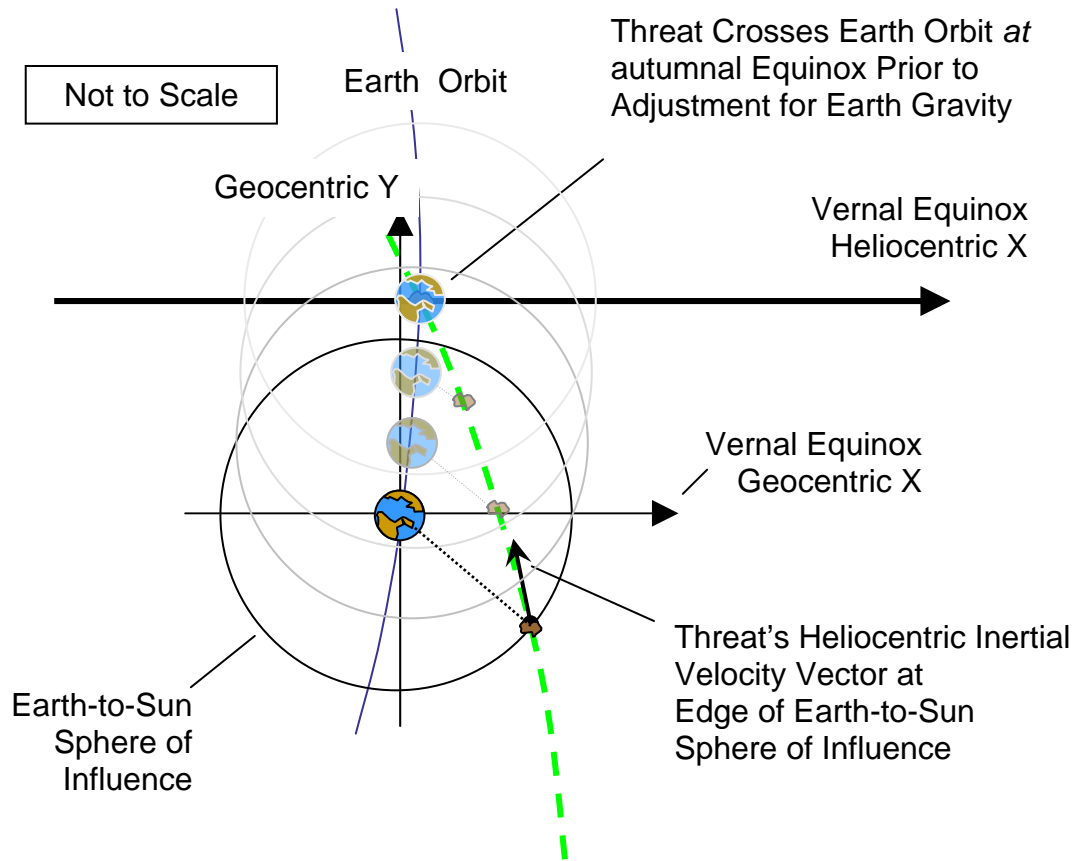
The threat orbit is next rotated about its own normal axis until the orbit crosses the ecliptic at a range of 1 AU. This is accomplished mathematically by zeroing out longitude of ascending node and then solving for the value of argument of perihelion that forces threat ecliptic crossing at that desired 1 AU. The result is a threat orbit that pierces the Earth's postulated 1-AU orbit, again, at autumnal equinox. This final rotation is shown in Figure 3-17 along with an oblique view of the previous rotation.

Figure 3-17: Representation of Process for Generating an Earth-Impact Threat: Step 3



Having arranged for the centers of both the Earth and the threat object to arrive at autumnal equinox at the same time, the code now simultaneously back propagates both bodies until the threat arrives at the edge of the Earth-to-Sun sphere of influence. The back propagation from impact to the sphere of influence is shown in Figure 3-18.

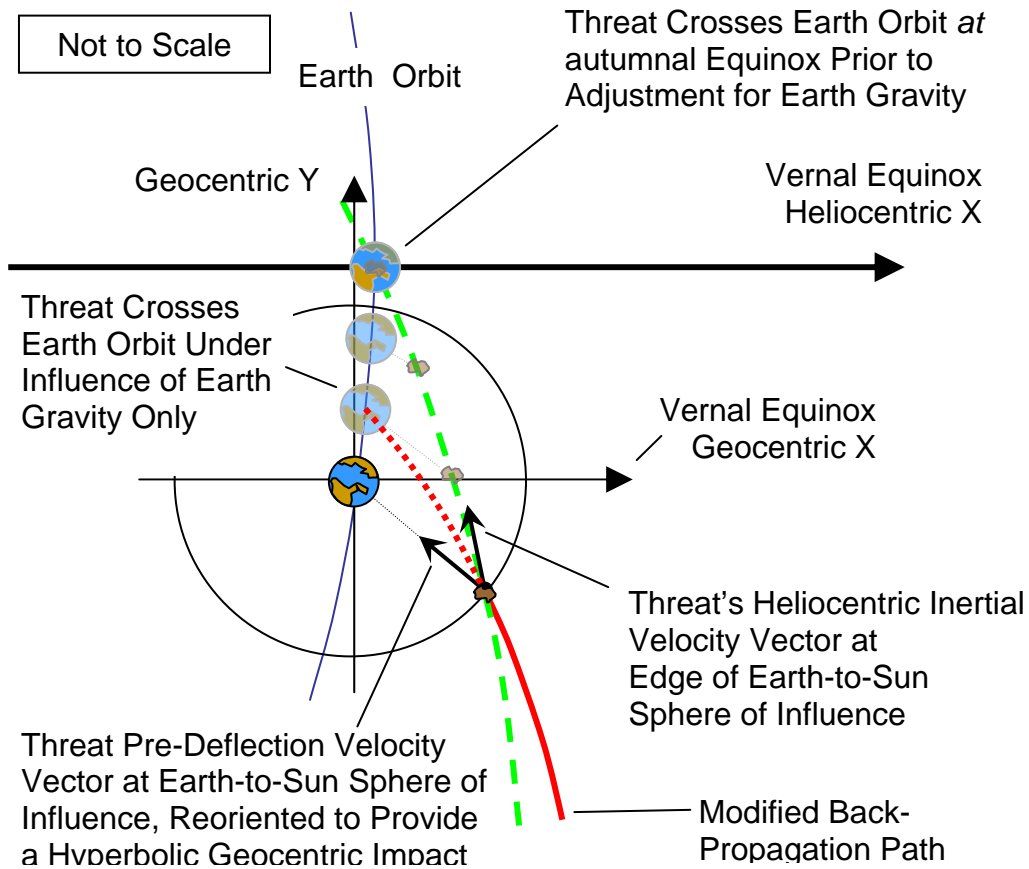
Figure 3-18: Use of Sphere of Influence in Modifying Pre-Deflection Threat Orbit: Step 1



The threat is now temporarily frozen at the edge of the sphere of influence. From this point in the analysis, whenever the threat is inside this sphere it moves solely under Earth's gravity, generally along hyperbolic paths in geocentric space. However, the threat velocity vector at its present position on the SOI is still that which was calculated to deliver the threat to a center-to-center Earth impact along an elliptical path in heliocentric space, that path being along the dashed line in Figure 3-18 leading to and indeed passing through the equinox. The velocity vector that the threat needs to possess is that which places it on a path leading to a dead-on impact under the influence of Earth's gravity only. To make the needed modification, the velocity portion of the state vector is

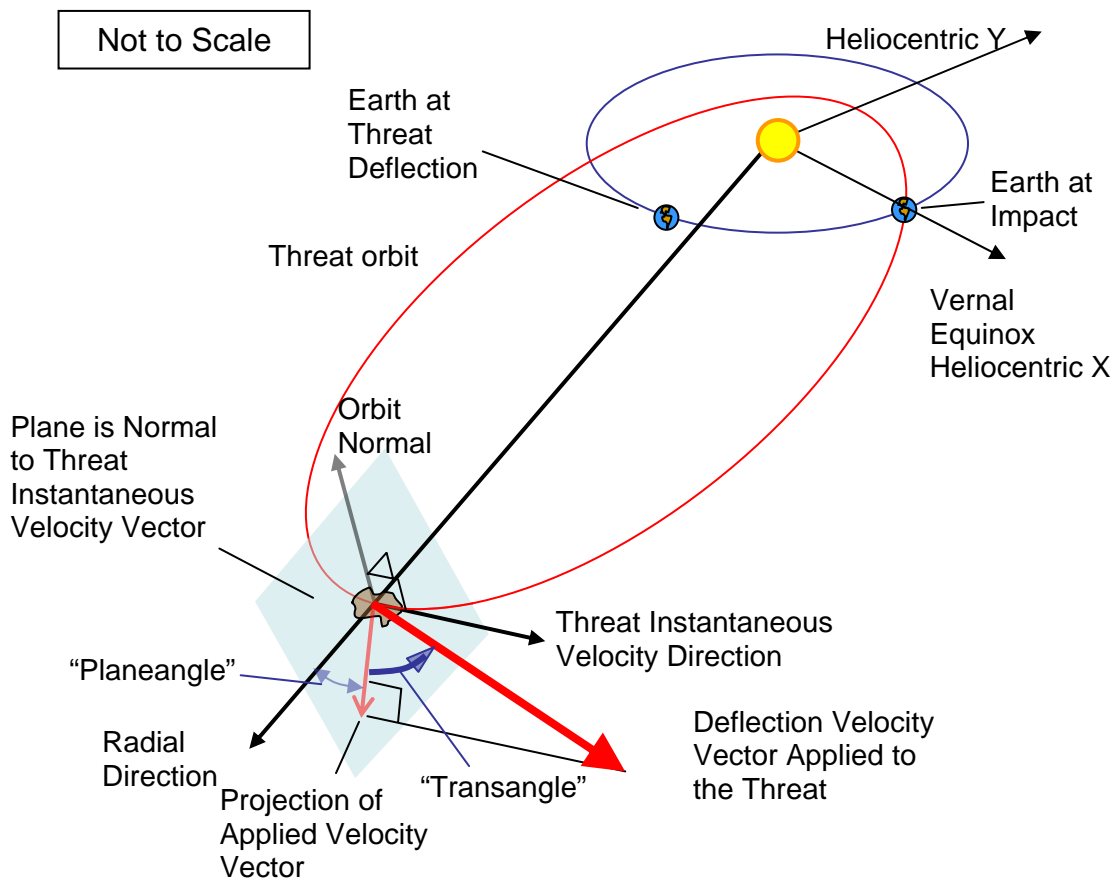
realigned so as to point directly at the Earth's center, thus guaranteeing a "dead-on" hit for continued propagation under the influence of Earth gravity only. This modified path is represented by the dotted line in Figure 3-19. Note that the actual time of impact is allowed to change slightly to account for a small difference in hyperbolic/geocentric versus elliptical/heliocentric time of flight from the edge of the sphere of influence. The angular separation of the two vectors has been exaggerated for graphical clarity: actual velocity vector realignments are small in magnitude; at worst on the order of five thousandths of a degree for long-period comets.

Figure 3-19: Use of Sphere of Influence in Modifying Pre-Deflection Threat Orbit: Step 2



With an Earth-gravity dead-on impact now assured, the modified threat state vector is back-propagated along the solid orbit line in Figure 3-19 to its position at the time prior to Earth impact at which a velocity change is to be imparted. With the threat back propagated, the code transforms the threat state into threat-local coordinates and applies the desired deflection according to the geometries shown in Figure 3-20, where the largest and noticeably out-of-scale vector represents the desired, user-selected velocity increment that is to be added to the threat's instantaneous velocity. The apparent vector magnitudes shown are not to relative scale; their relative sizes were selected for graphical clarity.

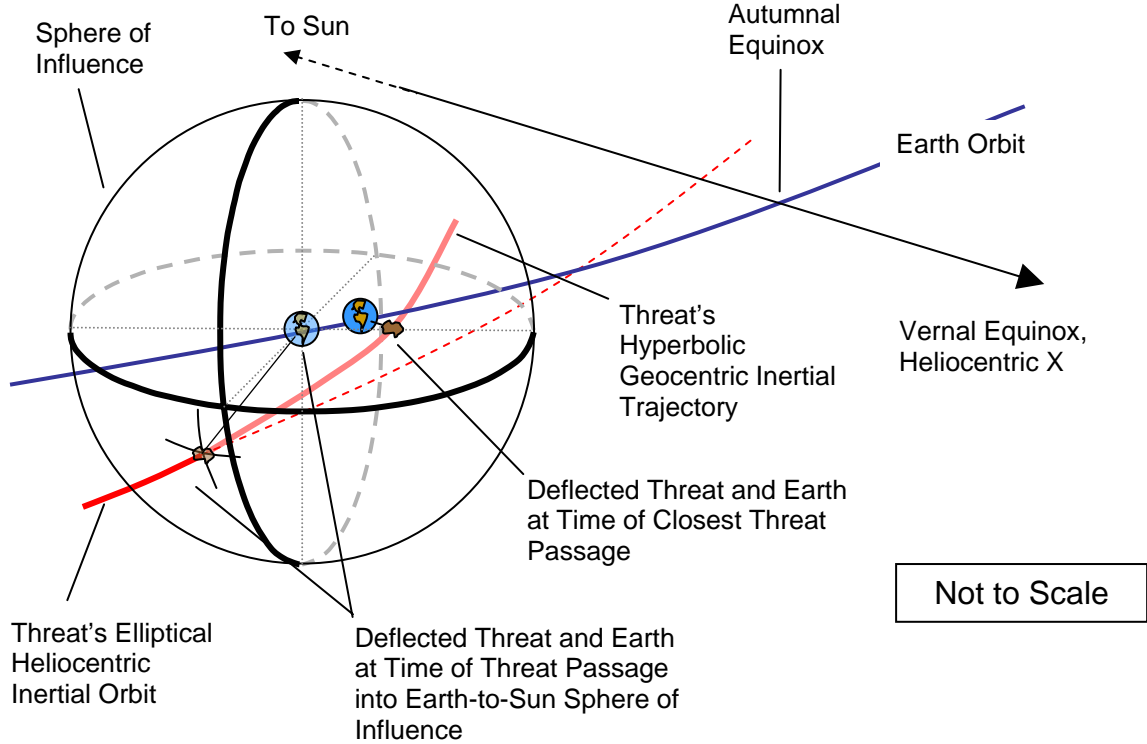
Figure 3-20: Geometry of Applied Deflection Velocity



The direction in which the velocity change is to be imparted is described by way of two independent angles that are measured relative to the threat's heliocentric position and velocity vectors. The first angle, termed the "Transangle," is the measure between the imparted velocity vector and the plane normal to the threat's instantaneous orbital velocity vector, making it essentially a local elevation angle of the imparted velocity. As with topographic elevations, Transangle can possess values between positive and negative 90 degrees. The second angle, termed "Planeangle," is the separation between the threat's orbital radial direction and the projection that the applied velocity makes onto the normal plane previously described. This construction makes Planeangle essentially an azimuth measure, its datum being coordinate axis in the orbital plane, and its values ranging between positive and negative 180 degrees. This construction allows the imparted velocity change to be applied in any desired direction.

With the threat's velocity modified as desired, the code transforms the threat's state from threat-local coordinates back to heliocentric coordinates, and then forward propagates the threat along its altered orbit. When the altered inbound threat again approaches the Earth, it is refrozen at the edge of the sphere of influence, and its new heliocentric inertial state vectors are re-translated into geocentric inertial coordinates, making the orbit again hyperbolic/geocentric in nature. Finally, threat displacement is in the form of closest passage of the centers of the Earth and of the threat is calculated as hyperbolic miss distance. (The fact that a real threat would have to be deflected by at least 1 Earth radius to actually achieve "passage" is acknowledged and will be addressed in Chapter 4.) These last two steps are depicted in Figure 3-21.

Figure 3-21: Use of Sphere of Influence in Calculating Threat Displacement at Earth



The modeling process described is implemented by way of a series of linked MATLAB codes [26]. This code set is structured such that a subset of “control” programs, each specialized to allow tailored manipulation of the various performance variables of interest, sweeps through the full ranges of desired deflection times and directions, and, one at a time, feeds each combination to a core displacement calculation code, which, again, is described in greater detail in Appendix B. It is the displacement calculation code that performs the actual back propagation, deflection, forward/re-propagation, and, finally, calculation of the threat displacement at closest hyperbolic Earth passage. For each deflection time, the control code collects the displacements achieved at the various Transangle and Planeangle directional settings, searches through them to locate the peak attainable threat displacement, and records it along with its

associated directional settings. The code set was run so as to execute this process at a variety of discrete points throughout the previously-described representative threat set, with deflection opportunities generally assumed to start at 50 days prior to impact and reaching back to just over 10 full threat orbits, again, a conservative number.

With respect to the general behavior of deflected threats, those that undergo a velocity change that is applied in the threat orbital plane and transverse to the threat's instantaneous velocity will experience a maximum spatial displacement at 90 degrees of eccentric anomaly from the point of velocity application. Because transverse changes do not change semi-major axis, the object returns to that deflection point and does so at the same time that it would have arrived had it not been deflected. Deflections applied in the threat orbital plane but along the threat's instantaneous velocity will, in general, experience a change their semi-major axis, and thus also their orbital period and eccentricity. Such deflections are therefore expected to be oscillatory with a secular component that grows with successive orbits [2], a pattern that is in fact seen in the deflection data presented in the next chapter. A more complete treatment of the generalized behavior of deflected objects is presented in Appendix A.

While the codes themselves are capable of designating a deflection vector in any desired direction, out-of-plane deflections in general do not add significantly to the attainable threat displacement, and were therefore not included in the main analysis. This conclusion is supported by a simple examination of the velocity change required to alter a nominal threat object's inclination enough to achieve an Earth miss. Regardless of the threat in question, the maximum displacement available from an inclination change is achieved when the threat is deflected at a point 90 degrees in true anomaly prior to the

expected Earth impact. Taking as the threat in question an Aten in the ecliptic with an orbit nearly coincident with that of the Earth, achieving an Earth miss distance of the aforementioned 6488 km solely with an inclination change requires a post-deflection threat inclination of a seemingly small 0.0025 degrees. However, because the threat object is traveling at approximately 30 km/s, turning that velocity vector by 0.0025 degrees requires approximately a 1.3 m/s velocity change, three orders of magnitude larger than the 1-cm/s figure discussed earlier. The portion of a threat displacement attributable to threat inclination change is therefore assumed to be negligible; as such, Planeangle was universally set to zero, and only Transangle was varied in the production of the data for this paper.

Chapter 4 - Threat Displacement Simulation Products

4.1 Asteroid Example Case

The post-deflection threat displacement data obtained from the described simulation codes are now introduced by way of a step-by-step treatment of calculations made for a single, nominal point in the representative threat set. The key orbital elements selected for this example threat are $rp = 0.7$ AU, $e = 0.4$, and $i = 0$ degrees. Figure 4-1 plots this threat object as it moves through one orbit over its approximately 460-day period. Note again the direction of the threat's orbit as it approaches Earth impact and that the threat happens to be an Apollo.

Figure 4-1: Example Threat Orbit for One Period

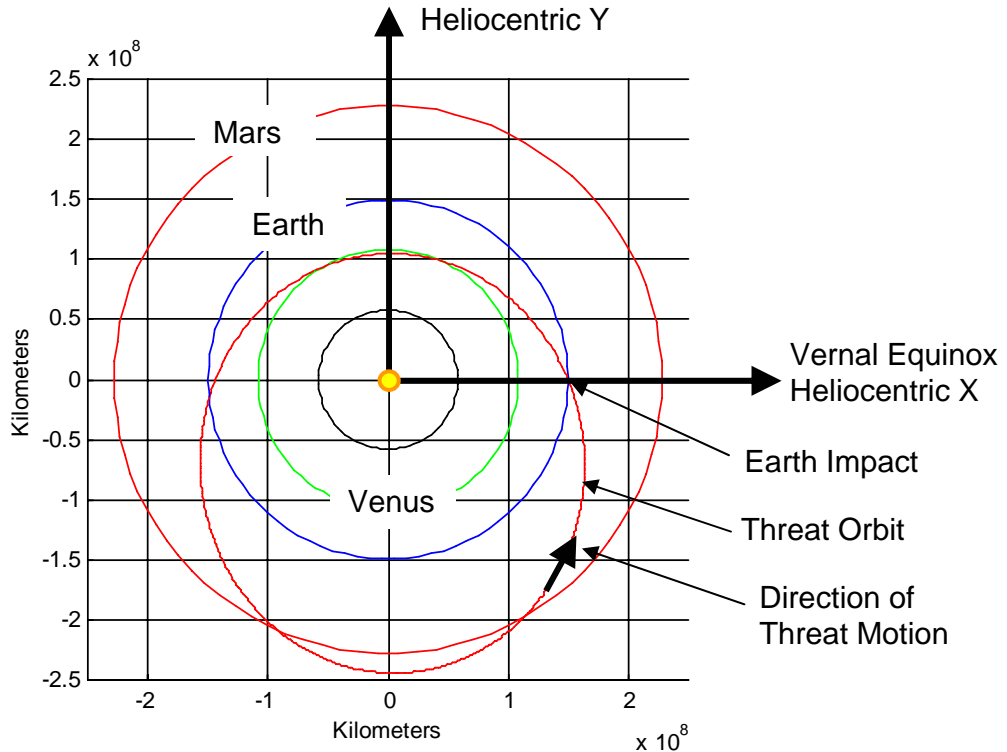
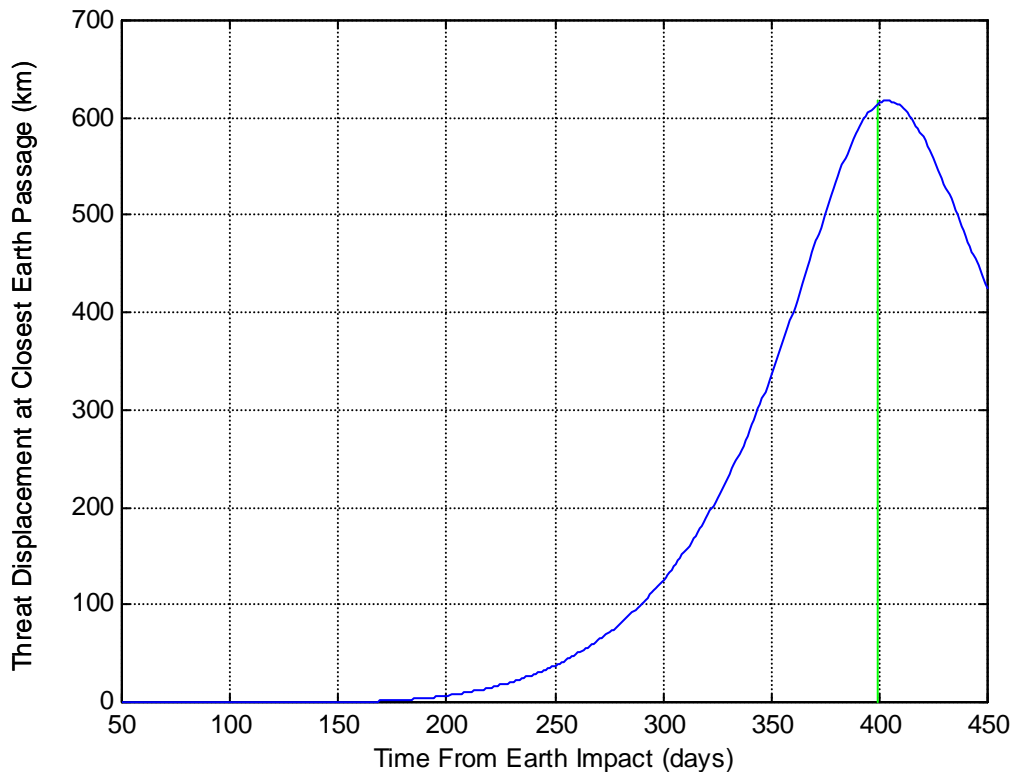


Figure 4-2 shows the principal form of output obtained from the code set: achievable threat displacement at closest Earth passage, measured center-to-center with the threat object, and developed as a function of how long before impending Earth impact that the threat object is deflected. This example case uses a nominal 1 cm/s impulsive velocity change, described earlier as being that generally accepted by the planetary defense community as achievable in the near-term; all other cases that follow likewise use a 1 cm/s velocity change unless specifically noted. For the plot shown, threat displacements were calculated for deflections aligned with the threat’s instantaneous velocity vector (i.e., for “Transangle” as defined in Figure 3-20 set to zero). The code was run at 1-day increments with deflections performed at times between 50 and 450 days before Earth impact.

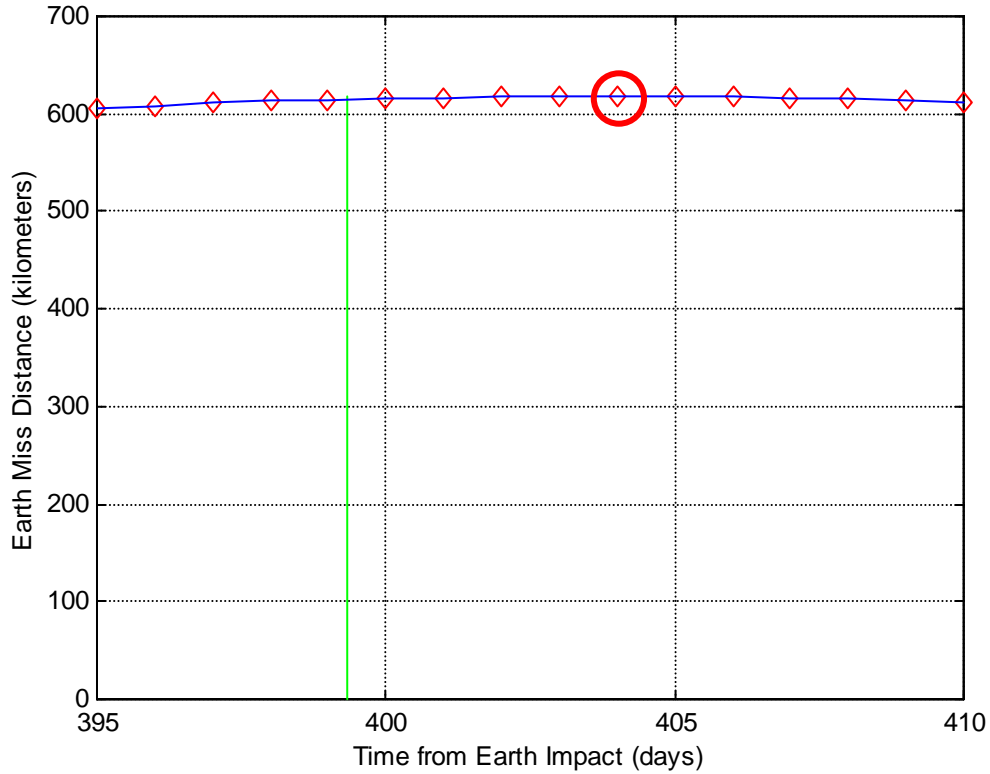
Figure 4-2: Example Threat Displacement Plot



As might be expected, the plot shows that the earlier this threat is deflected (i.e., the farther to the right on the x-axis), the larger the achievable threat displacement, at least as far back as about 400 days before Earth impact. Of particular note is that the ascending section of the plot is not linear: the portion of the curve reaching back to approximately 325 days before impact shows an increasing rate of payoff for performing deflections earlier and earlier. For deflections occurring prior to that, displacement still increases but the rate of payoff flattens and then diminishes, eventually reaching a peak of just over 617 km at about 404 days before impact.

Unfortunately, the achievable threat displacement for this peak (i.e., the local optimum in the displacement curve) is not nearly enough to provide an actual Earth “miss,” at least not against a threat that would have otherwise been a center-to-center hit. That detriment accepted, it is also of note that the peak displacement shown does not occur exactly at perihelion, which is marked in Figure 4-2 by a solid vertical line, as it is in all subsequent charts of this type, when appropriate. Figure 4-3 is a close up of the displacement curve peak of Figure 4-2, with the day-by-day deflection events marked with diamonds and the peak deflection itself circled. It is seen that for the example threat object, achieving peak threat displacement requires that the threat be engaged almost five days prior to perihelion.

Figure 4-3: Example Threat Maximum Deflection Offset from Perihelion



This offset from perihelion runs contrary, albeit slightly, to the common opinion within the planetary defense community that the orbital location at which the greatest displacement is possible is exactly at an object’s perihelion [49]. This standard rule is derivable by applying variation of parameters to the energy equation, as shown in Equations 4.1 and 4.2. First the energy equation is solved for the velocity term:

$$\varepsilon = \frac{v^2}{2} - \frac{\mu}{r} = \frac{-\mu}{2a} \quad \rightarrow \quad v^2 = \mu \left(\frac{2}{r} - \frac{1}{a} \right) \quad (4.1)$$

In this equation, ε is the asteroid's orbital energy, r is the asteroid's distance from the Sun (i.e., its radius), v its velocity at that position, μ is the Sun's gravitational parameter (equaling, by definition, the Sun's mass multiplied by the Universal Gravitational Constant), and a is the asteroid's semi-major axis. Letting radius r be constant, differentiation of both sides of Equation 4-1 yields:

$$da = \frac{2a^2}{\mu} v dv \quad (4.2)$$

This implies that the maximum increase in semi-major axis is obtained by deflecting when the threat's velocity v is greatest, a condition that occurs at perihelion. Also implied is that the optimal direction for the deflection is that which results in the largest velocity change dv , which, for action taken at perihelion, is either aligned with or in the opposite direction of the threat's instantaneous velocity. If these two conditions are satisfied, semi-major axis will experience the maximum change possible, with the location of maximum displacement from the original orbit being exactly at aphelion. However, the Earth will not, in general, be at threat aphelion except for only the most specialized Aten threats. For more general threat geometries, it is not unreasonable to think of deflections as changing both the point at which a threat crosses the Earth's orbit and the time at which it crosses [9], in accordance with the discussion at the end of the last chapter. To better illustrate this and the perihelion offset, an analysis was run using a simplified code that models just the threat's closest passage relative to its pre-deflection location (i.e., the closest passage to autumnal equinox for a deflected threat that otherwise would have passed through the equinox, but without involving Earth-relative distances or Earth

gravity). For this scenario, deflections applied exactly at perihelion indeed produced the maximum displacement. However, when displacement was then measured relative to a moving Earth for the same deflections applied to the same threat, the perihelion offset appeared. The offset was found to be merely a manifestation of the relative motions of the change in threat arrival time combined with Earth motion (see Appendix A).

Returning to the example threat, Figures 4-4 and 4-5 show the threat's motion through perihelion, with day-by-day progress marked in Figure 4-4 with diamonds, and the perihelion offset shown in Figure 4-5 against the full scale of the threat orbit. The offset distance is over 15 million kilometers, about 40 times the Earth-Moon distance.

Figure 4-4: Example Threat Perihelion Passage

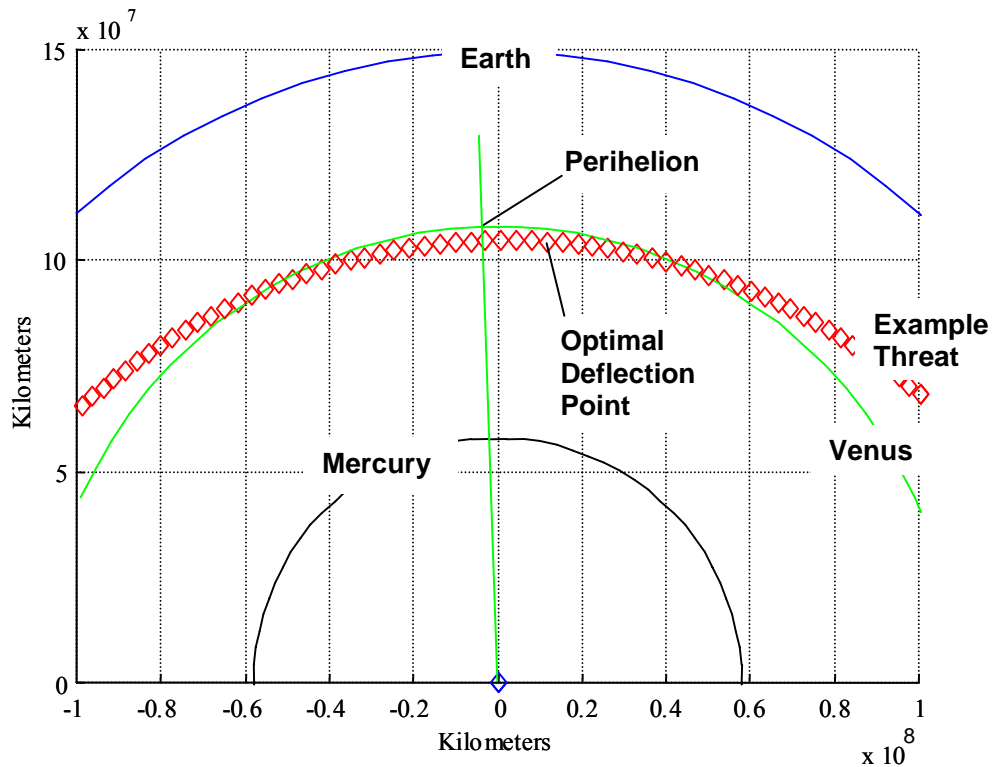
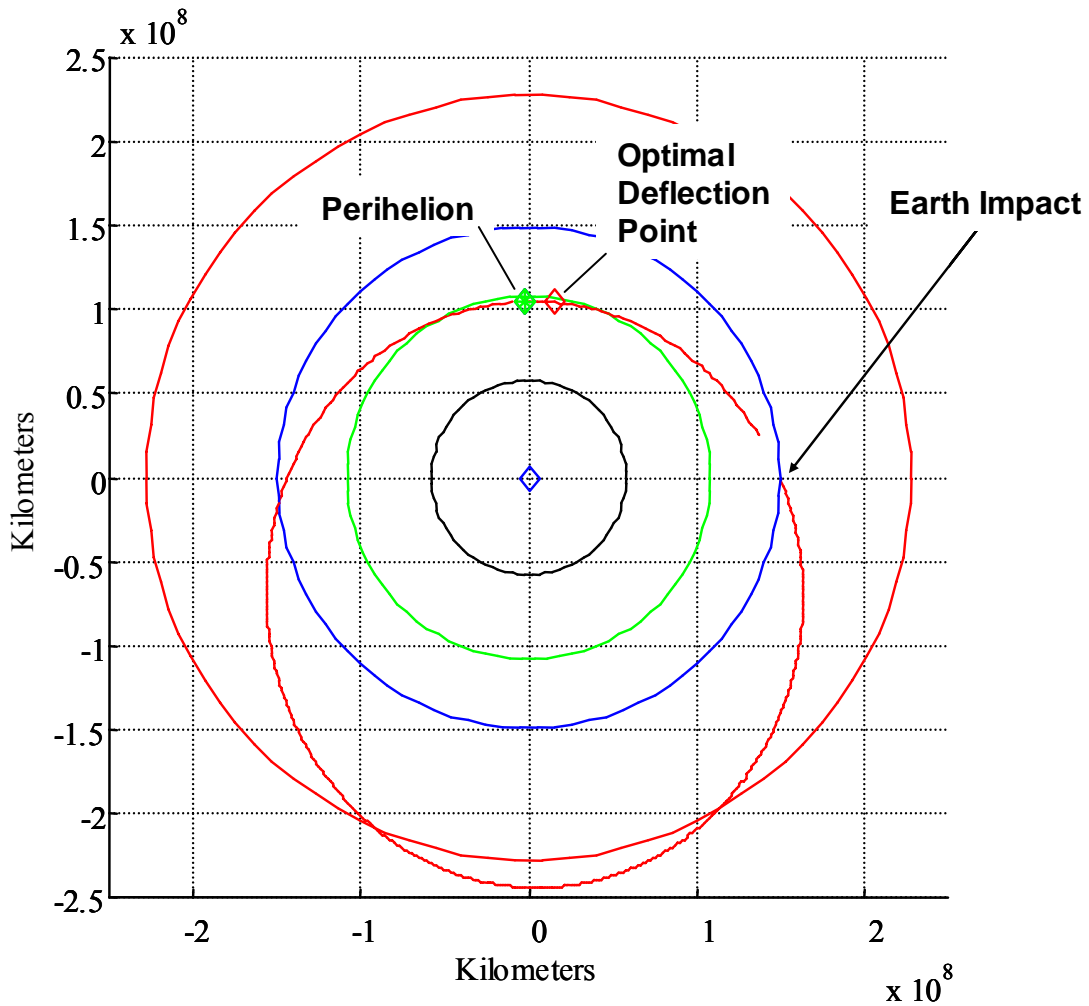
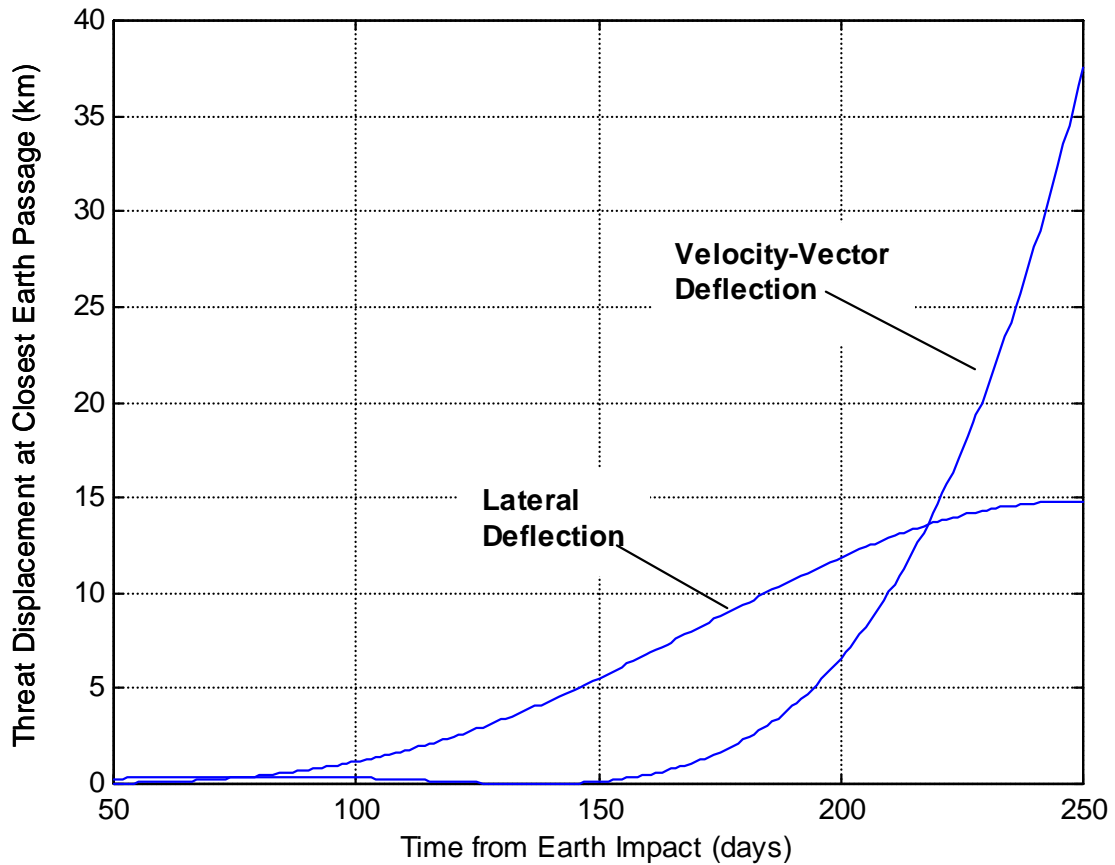


Figure 4-5: Example Threat Orbital Plot with Perihelion and Optimal Deflection Point



It is a common assumption in the planetary defense community that for threats that are not deflected until they are on their final approach to Earth (i.e., threats that have already passed their final pre-impact aphelion), optimal threat displacement is achieved by deflecting the object perpendicular to the threat's velocity vector [49]. Figure 4-6 shows the calculated threat displacement for lateral deflections as they are applied to the example threat, with that data superimposed over the associated velocity-aligned threat displacement data from Figure 4-2.

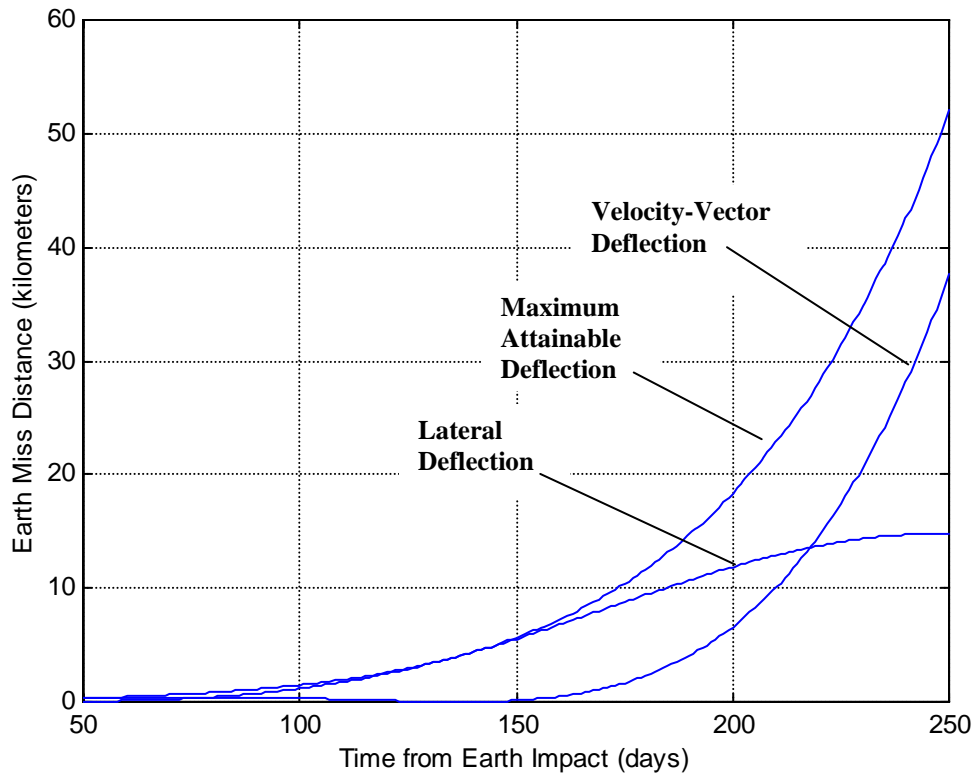
Figure 4-6: Comparison of Achievable Displacement for the Example Threat – Lateral vs. Velocity-Vector-Aligned Deflection



It is seen that for this threat lateral deflections of the example threat indeed produce larger displacements than do those that are aligned with the velocity, but only for mitigation attempts made within approximately 220 days of Earth impact. At about the 220-day mark the trend reverses, and by 240 days a velocity-aligned deflection offers twice the displacement of a lateral one. Neither of these, however, necessarily represents the maximum attainable threat displacement. That maximum displacement curve, obtained by varying Transangle over its full range of values and extracting the largest

resulting threat displacement, is shown in Figure 4-7, again superimposed over the established data.

Figure 4-7: Example Threat Maximum Attainable Deflection at Earth



Lateral deflections do produce the maximum threat displacements possible, but only for engagements taking place within about 150 days of Earth impact. For engagements that can be made earlier than that, neither lateral nor velocity-aligned deflections are optimal. Figure 4-8 expands this data back to the 450-day point, and is followed immediately in Figure 4-9 with a plot of the Transangle values that produced this maximum displacement curve.

Figure 4-8: Example Threat Maximum Attainable Deflection at Earth to 450 Days Before Impact

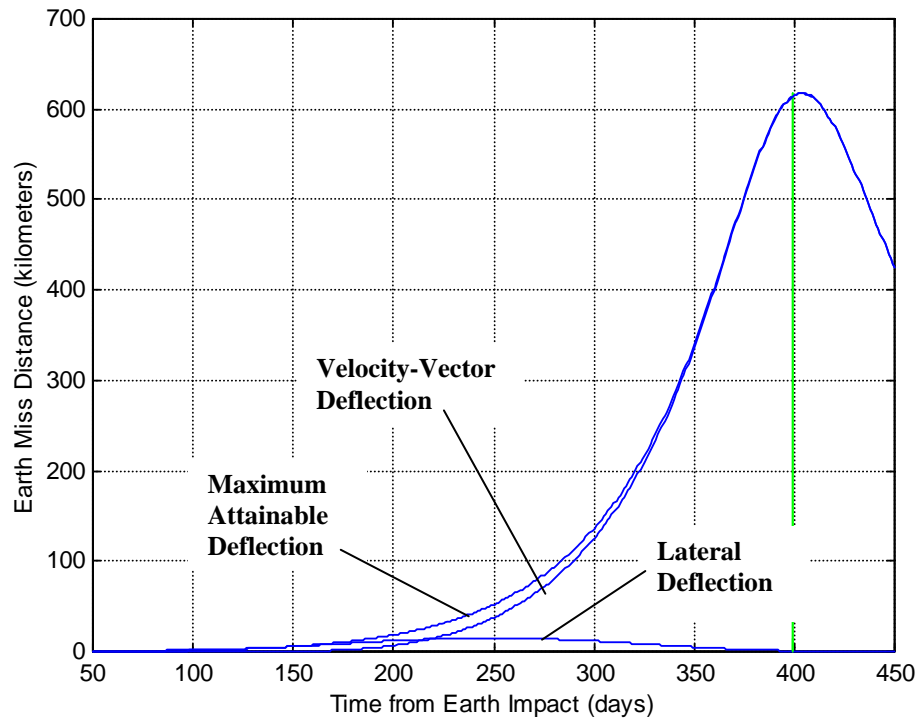
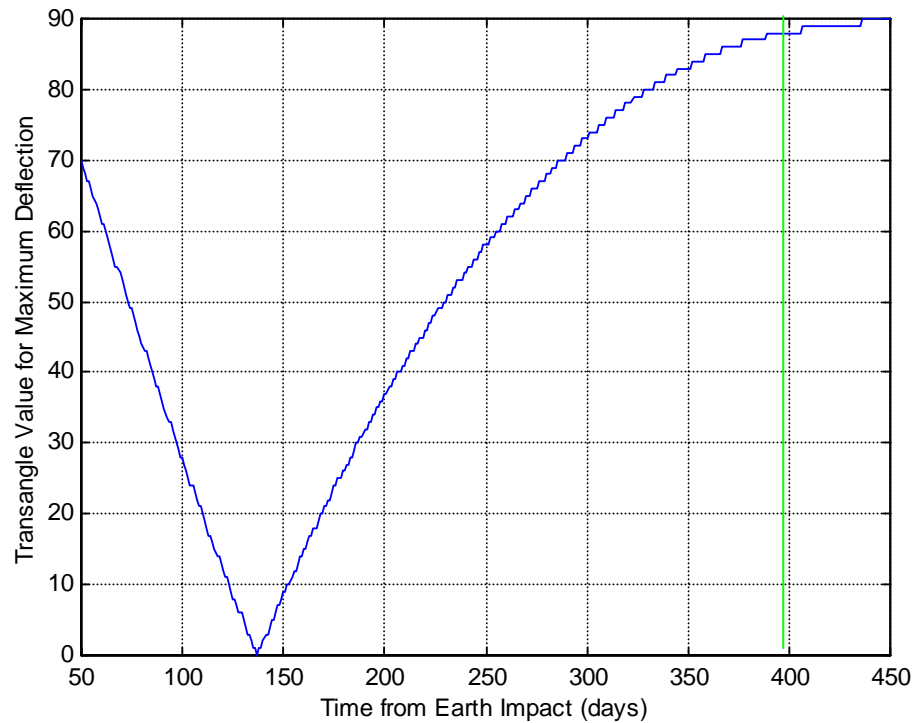


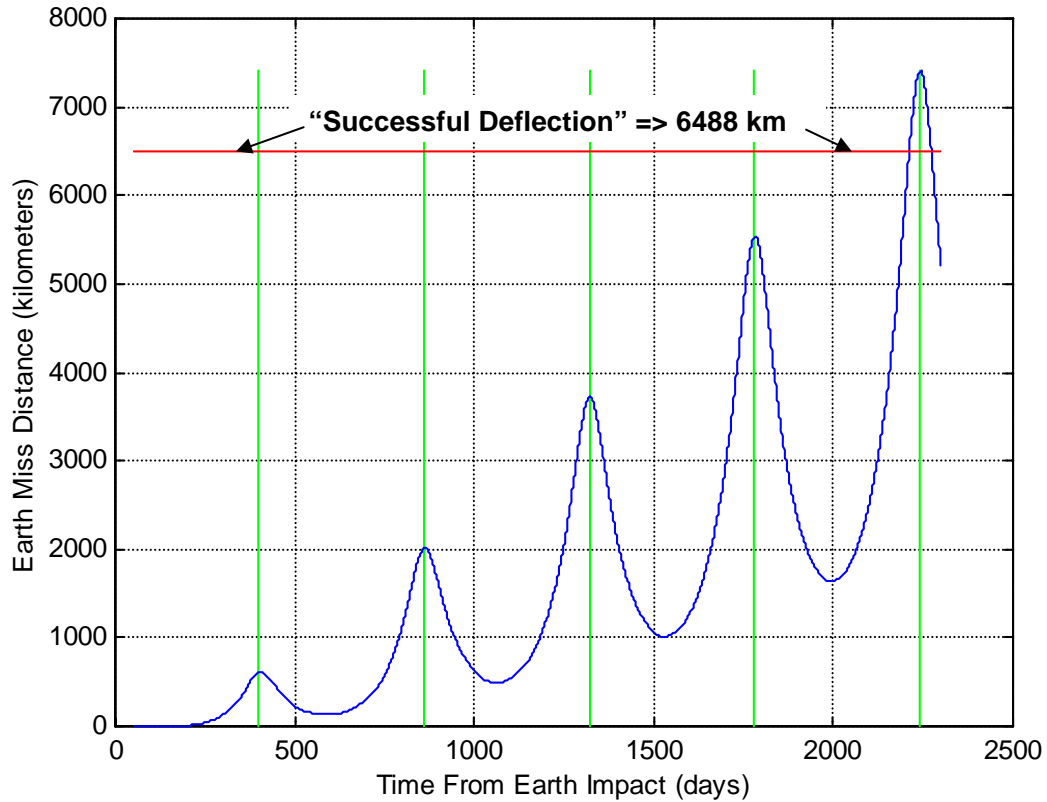
Figure 4-9: Example Threat Transangle Values for Maximum Threat Displacement



The first feature of note is the slope discontinuity that occurs in Transangle just prior to the 150-day mark in Figure 4-9. This reversal is simply a manifestation of the angle accounting processes used in the control codes: rather than having the plot ordinate range all the way from 70 down to negative 90 degrees, the code selectively chooses the threat displacements associated with *positive* Transangle values. It was determined that positive and negative Transangles give virtually identical threat displacement results; this will be demonstrated for the example threat in Section 4.6. Also of note is that although the threat displacement curve in Figure 4-8 approaches its maximum as Transangle approaches the 90-degree mark in Figure 4-9, neither the threat perihelion nor the point of maximum threat displacement for the timescale shown occurs quite at a 90-degree Transangle.

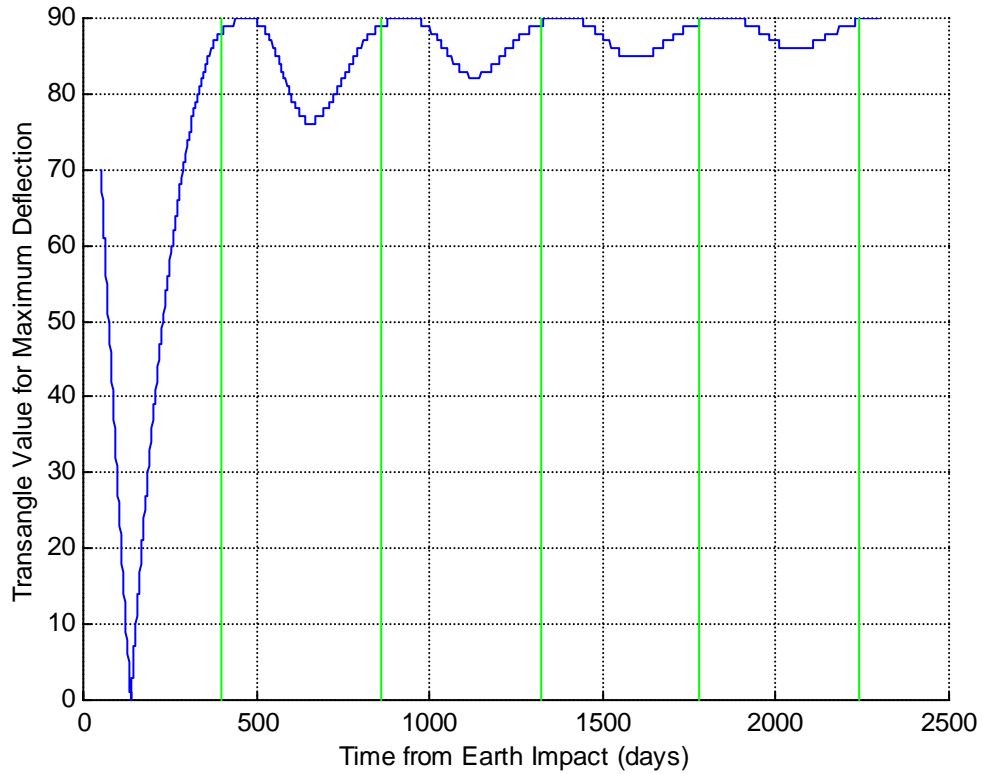
Figure 4-10 shows maximum 1-cm/s displacement of the example threat for multiple threat orbits prior to Earth impact. This data set was run so as to reach back in time far enough to find a displacement peak that would result in a successful “Earth miss,” which shall from here forward be defined as a threat displacement of at least the Earth’s radius plus 110 km of substantive atmosphere. (It is assumed that the preference is to have no chance of the threat depositing any of its energy or material in the atmosphere). This “successful deflection” threshold is marked in Figure 4-10 by a horizontal line.

Figure 4-10: First Successful Mitigation for Example Threat Case



The plot shows that in order to achieve a zero-margin Earth miss against the example threat, the 1-cm/s deflection must be applied approximately 6 years and 21 days before Earth impact. If displacement margin is desired, the deflection would have to take place about 30 days earlier at the local deflection peak. The largest margin available in this timeframe, however, is only about 1000 km. It should also be noted that the offset between perihelia (again, marked by the solid vertical lines) and the times of peak deflection shrinks to less than a day, although this effect is not observable at the plotting scale of Figure 4-10. The deflection directions required to produce these maximum threat displacements are shown in Figure 4-11.

Figure 4-11: Example Threat Transangle Values for Maximum Threat Displacement



Clearly Transangle does not simply settle in at 90 degrees, as the emerging trend from Figure 4-9 might have indicated. There is, in fact, a markedly cyclic but convergent behavior. Of particular note is the continuous offset of just over 70 days between threat perihelion and the time from Earth impact at which a 90-degree Transangle deflection produces a maximum threat displacement.

Finally, Figures 4-12 and 4-13 show achievable displacement of the example threat out to a full 10 threat orbits. Note that the ordinate of Figure 4-13 (i.e., the Transangle needed for maximum threat displacement) is truncated to make the vertical scale more useful.

Figure 4-12: Example Threat Maximum Threat Displacement Values

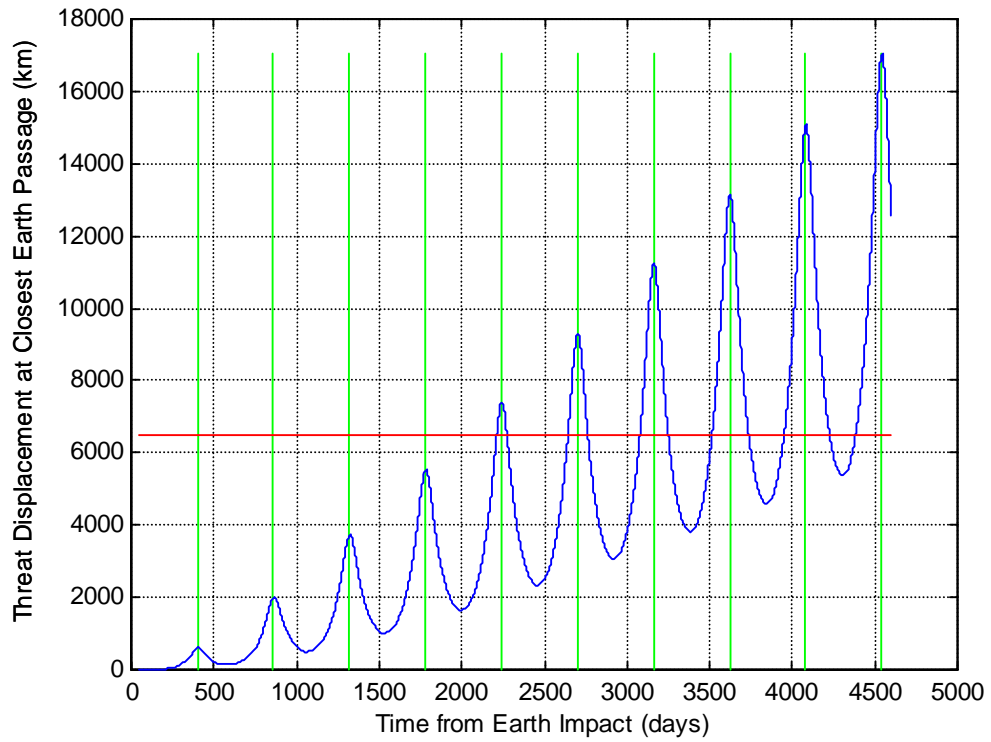
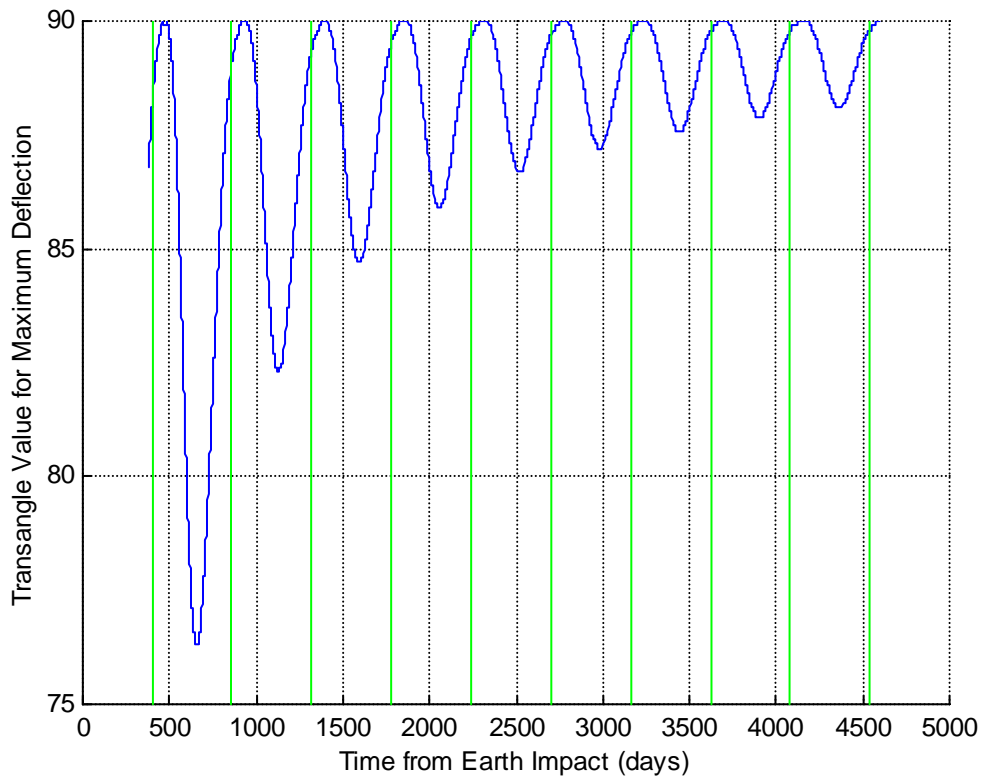


Figure 4-13: Example Threat Transangle Values Associated with Maximum Threat Displacement



The most prominent feature in these plots, at least as they relate to system and mission design, is that at no point in the timescale shown is a true Earth miss obtainable at all points in any one threat orbit. That said, there are deflection opportunities that do start to offer a reasonably-high displacement margin. These start at the 8th perihelion before impact, where the peak threat displacement is twice that required to make the threat miss the Earth. Within the 10-orbit limit, however, the highest displacement margin that could be achieved would be a factor of approximately 2.5, that being for a near the 10th peak, and occurring well over 12 years before Earth impact. Regarding the required deflection directions, the assumption that deflections directed along the threat's velocity vector (i.e., at a Transangle of 90 degrees) produce maximum threat displacements appears to be a fairly good rule of thumb for deflections occurring long before the impending Earth impact, but it cannot be applied absolutely.

4.2 Representative Threat Set Analysis Points

Table 4-1 lists the values of asteroid perihelion and eccentricity that were selected as the representative threat set for this effort. The bulk of the values were developed by matching whole-decimal values of perihelion from Table 3-1 to a range of eccentricities, also from Table 3-1 and also in whole-decimal steps. Next, appropriate boundary cases were developed by holding perihelion strictly to its whole-decimal values and then varying eccentricity until the resulting semi-major axis and aphelion reflected the values possessed by the observed threat (i.e. the 662 PHAs discussed in Section 3.1). In addition, because the geometric modeling used in the threat displacement calculation code is efficient for threat orbits that are Earth-crossing but not for those that are

osculating, the largest perihelion value was set at 0.99 AU instead of the 1.0 AU listed in Table 3-1.

Finally, so as not to waste analysis effort in the evaluation of trends that might apply only to small, unsuccessful threat displacements, low-end limits on eccentricity were established such that at least the 10th deflection peak resulted in an Earth miss. That said, assessments of the capability to address the overall PHA threat are indeed made against the entire representative threat set.

Table 4-1: Case Run Summary

Radius of Perihelion r_p (AU)	Eccentricity e	Limit Case Description (if applicable)
0.1	0.846, 0.9, & 0.956	Low: limit on semi-major axis High: limit on eccentricity
0.2	0.7065, 0.8, 0.9, & 0.944	Low: limit for deflection of 1 Earth radius High: limit on aphelion
0.3	0.593, 0.6, 0.7, 0.8, 0.9, & 0.918	
0.4	0.494, 0.5, 0.6, 0.7, 0.8, 0.890	Low: limit for deflection of 1 Earth radius High: limit on semi-major axis
0.5	0.407, 0.5, 0.6, 0.7, 0.8, 0.863	
0.6	0.333, 0.4, 0.5, 0.6, 0.7, 0.8, 0.836	
0.7	0.271, 0.3, 0.4, 0.5, 0.6, 0.7, 0.8, 0.808	
0.8	0.225, 0.3, 0.4, 0.5, 0.6, 0.7, 0.781	
0.9	0.209, 0.3, 0.4, 0.5, 0.6, 0.7, 0.753	
0.99	0.357, 0.4, 0.5, 0.6, 0.7, 0.729	

Each of the perihelion/eccentricity combinations captured in Table 4-1 was analyzed at inclinations of 0, 5, 10, 15, 25, 40 and 70 degrees as was stipulated in Table 3-1. This produces a representative threat set containing 420 discrete threat members made up of

60 perihelion/eccentricity pairings each evaluated at the 7 discrete inclinations. The core analysis product developed for this paper is a collection of displacement curves like that of Figure 4-12, calculated for each of these 420 combinations, and each reaching back to a full 10 threat orbits before Earth impact. With those curves each starting at 50 days prior to Earth impact and progressing in 1-day increments, the number of discrete deflection events represented in this analysis totals approximately 630,000. However, this represents only about 60% of the total runs made; approximately 420,000 supporting runs were executed to confirm that deflection performance was continuous out to and along the edges of the threat set.

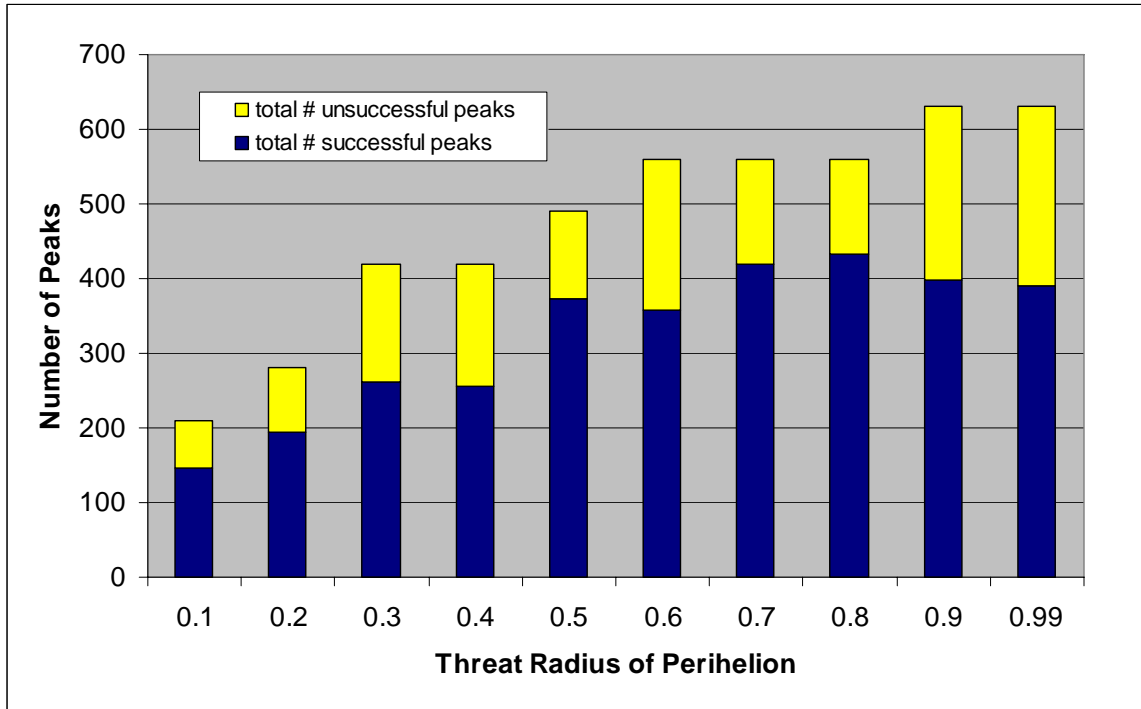
4.3 Overall Asteroid Deflection Opportunities

The first metric of interest in assessing threat deflection opportunities is a straightforward measure of how much of the representative threat set can be successfully deflected at the 1-cm/s level. This metric was calculated as the percentage of the total number of deflection peaks that break through the Earth-miss threshold (i.e., the horizontal lines at 6488 km that are featured in Figures 4-10 and 4-12). However, to prevent the outcome from being biased in its tallying of opportunities for successful deflection, the constraint discussed earlier that eliminated unsuccessful perihelion/eccentricity pairings was temporarily lifted. If it had not been, the more challenging portion of the threat set would have been underrepresented.

With the unsuccessful cases temporarily added back in, the resulting “unconstrained” set possesses 4760 peak deflection opportunities, made up of 68 perihelion values, 7 inclinations, and 10 peaks per combination. All of these are represented in Figure 4-14,

which shows the relationship of successful to unsuccessful 1-cm/s peak deflection opportunities.

Figure 4-14: Total and Successful Deflection Peaks by Perihelion for Unconstrained Representative Threat Set

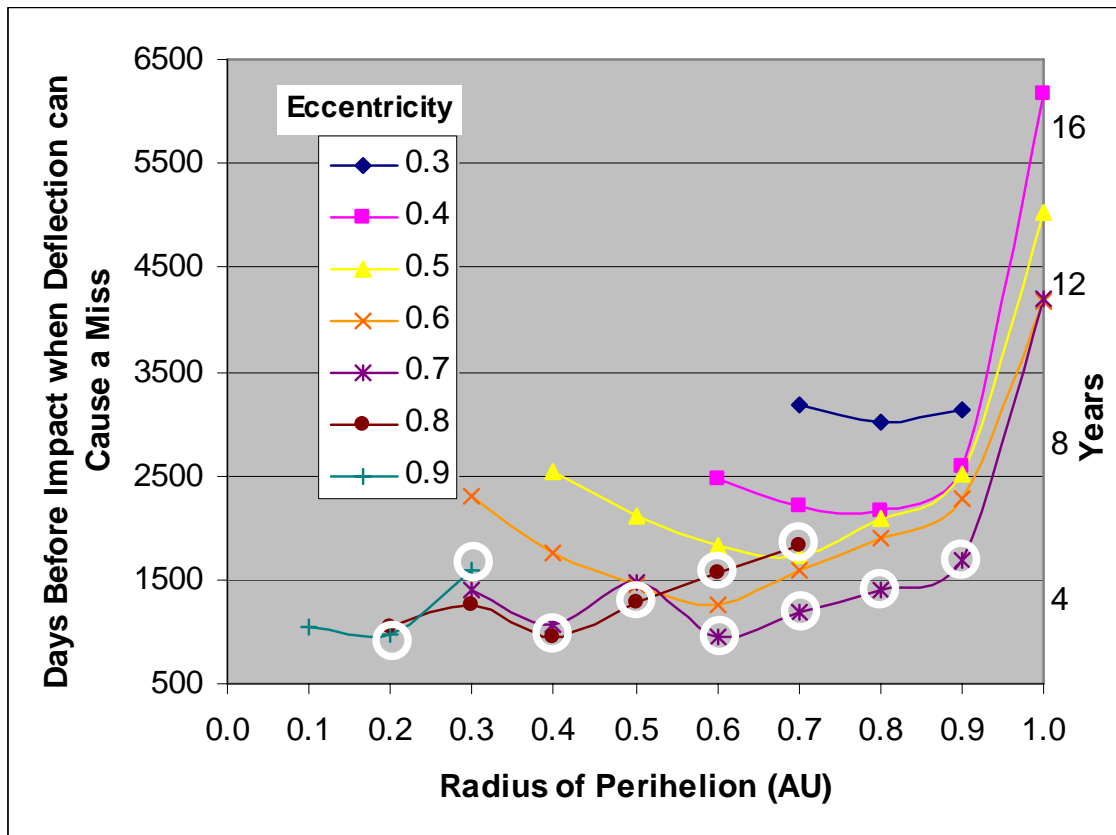


With the unconstrained threat set used as a basis, it is found that 68% of the 1-cm/s peaks produce successful Earth misses. By all accounts and assumptions made thus far, there should be significant opportunities to conduct a successful planetary defense. Further, if it is assumed that the 10-threat-orbit assumption can be expanded to 20 orbits, then nearly 80% of peak opportunities could be successful at 1-cm/s.

4.4 Latest Possible Asteroid Deflection Before Earth Impact

Building on the conclusion that many opportunities should exist to successfully deflect threatening asteroids, the next metric of interest would be how late of a deflection would still achieve an Earth miss against the objects in the representative threat set. The plot in Figure 4-15 gives the latest possible times for achieving zero-margin deflections against threats with zero-degree inclination with a 1 cm/s threat velocity change. Note that these data points do not represent “peak” deflection opportunities; they are the first times that each displacement curve rises above the 6488-km “Earth miss” threshold. For graphical clarity, only whole-decimal eccentricity values from Table 4-1 are presented.

Figure 4-15: Latest 1 cm/s Earth-Miss Deflection Opportunities



The data in Figure 4-15 show that for the conservative deflection level, no successful deflection opportunities exist earlier than about 2.6 years prior to Earth impact, and only one-third of the threat can be successfully deflected if addressed within 5 years of their individual impacts. However, a surveillance and mitigation system structured so that it can acquire threats, confirm that they are hazardous, and fly out and engage them with at least 10 years before impact would be able to consummate over 93% of the latest-deflection opportunities.

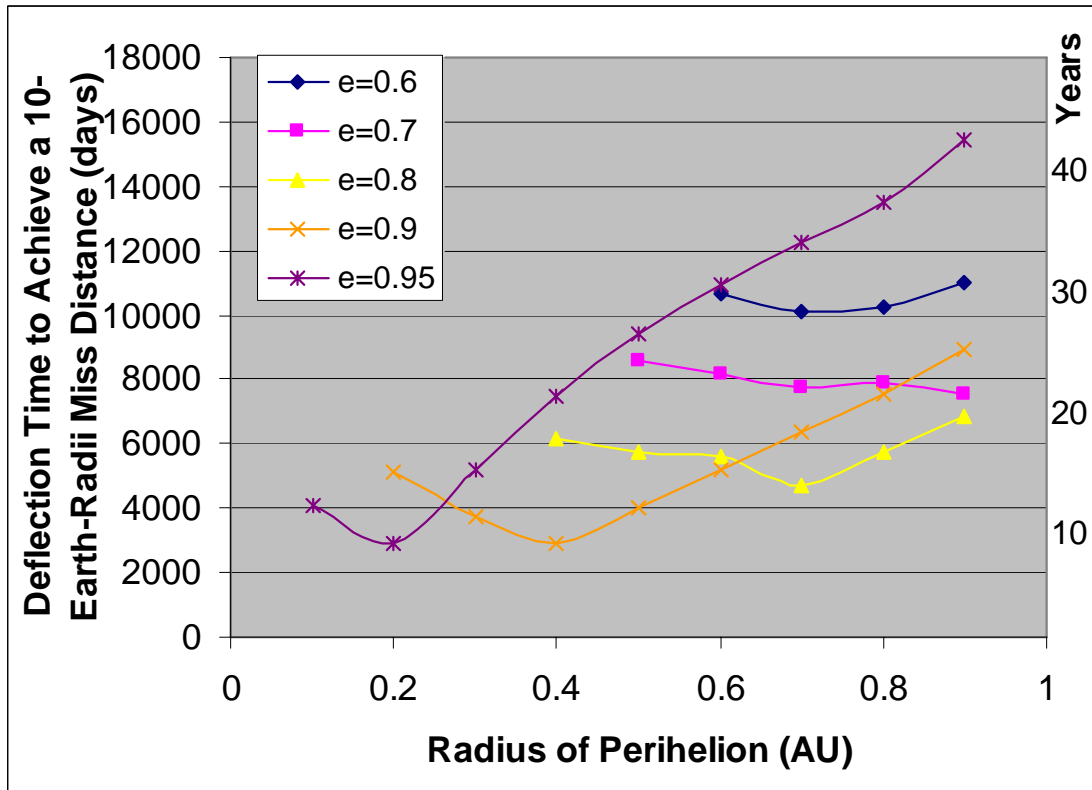
The circled points scattered along the bottom of Figure 4-15 are of particular interest, as they represent those deflection opportunities that occur after the threat's last pre-impact perihelion, contradicting the conventional wisdom within the planetary defense community that deflection events will always have to occur numerous threat orbits in advance. It should be noted, however, that none of the circled data points provides an Earth miss after the threat has passed its last pre-impact *aphelion*: conservative levels of impulsive deflection do not work when the threat is on its "final approach."

4.5 Threat Displacement Margin Through Earlier Asteroid Deflection

While opportunities for last-minute deflections exist, it should be assumed that in a real planetary defense engagement every attempt will be made to maximize threat displacement margin. The general form of the threat displacement curves makes it clear that the earlier Earth impactors are located and acted on, the greater the achievable margin and, perhaps more importantly, the more deflection opportunities exist. Figure 4-16 was developed by assuming that a large appetite for displacement margin demands

that the stock 1-cm/s threat velocity change be able to displace a threat object by a full 10 Earth radii and an equal number of atmosphere thicknesses.

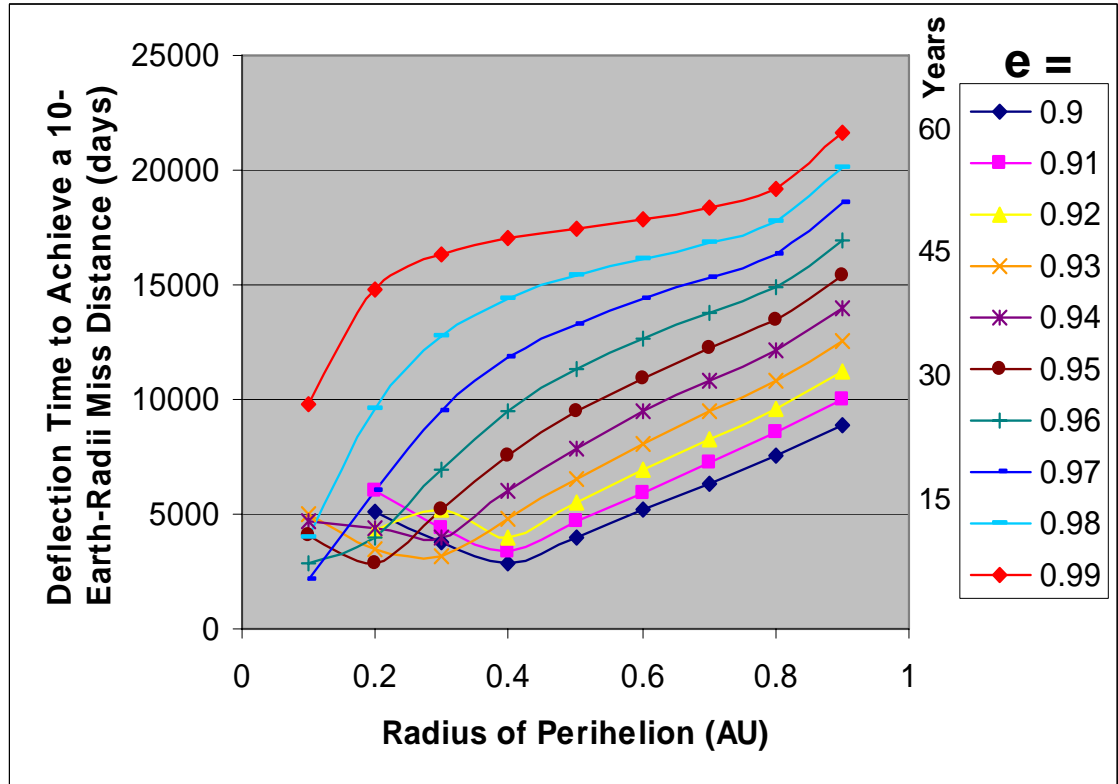
Figure 4-16: Deflection Times to Achieve Threat Displacement of 10-Earth Radii with a 1 cm/s Deflection



Of immediate interest is that while this data set shows a reasonable trend as eccentricity descends from 0.6 to 0.8, reason seems to be absent for $e = 0.9$ and higher. Note that this departure actually started to appear in the zero-margin threat displacement data plotted in Figure 4-15. To determine whether this data set is really discontinuous, Figure 4-17 was plotted at a higher eccentricity resolution and for a more focused

eccentricity band where $e = 0.9$ to 0.99 , the region where the behavior in Figure 4-16 appears to change most radically.

Figure 4-17: Deflection Times to Achieve Threat Displacement of 10-Earth Radii with a 1 cm/s Deflection at High Eccentricities



From Figure 4-17 it is concluded that the trend is sufficiently continuous inside of this eccentricity interval. Also, returning to the real issue at hand, it appears that there are a fair number of high-margin deflection opportunities, although many of them demand long lead times (i.e., early threat engagements). Also of note is that there are no high-margin opportunities against threats with eccentricities below 0.6. This is because large margins require time for the threat object displacement to accumulate after deflection; because

threats with smaller eccentricities have smaller periods, the time required to accumulate a displacement large enough to achieve the described margin can turn out to be longer than allowed by the 10-threat-orbit limit.

Figures 4-18 and 4-19 present a broader view of achievable threat displacement margins across the entire representative threat. The figures map out the availability of displacement margin, with the vertical “Miss Factor” dimension being the number of Earth-radii-plus-atmosphere distances (i.e., 6488 km) that are attainable beyond that needed for a zero-margin Earth/atmosphere miss (e.g., for a threat that can be displaced by 12,976 km – twice the minimum displacement of 6488 km – Miss Factor equals 1). Miss Factor for each perihelion/eccentricity pairing was calculated at zero degree inclination for the 1st, 5th, and 10th peak deflection opportunities, and the data were grouped by threat perihelion; the dotted vertical lines are merely section dividers between groups with differing values of perihelion radius r_p . Note also that eccentricities at the lower limits of Table 4-1 are not included in this data: as described earlier, those cases were designed to have deflections explicitly at 6488 km, so including them in this treatment would be misleading.

Figure 4-18: Threat displacement Margin in Terms of Miss Factor; Low Perihelia

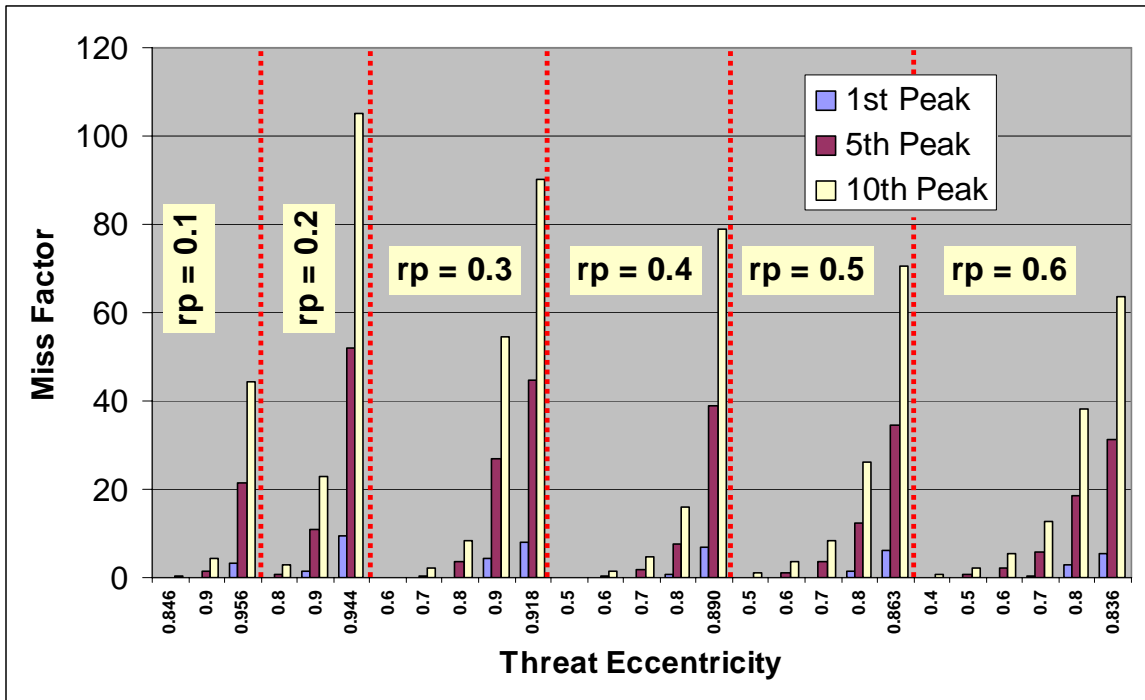
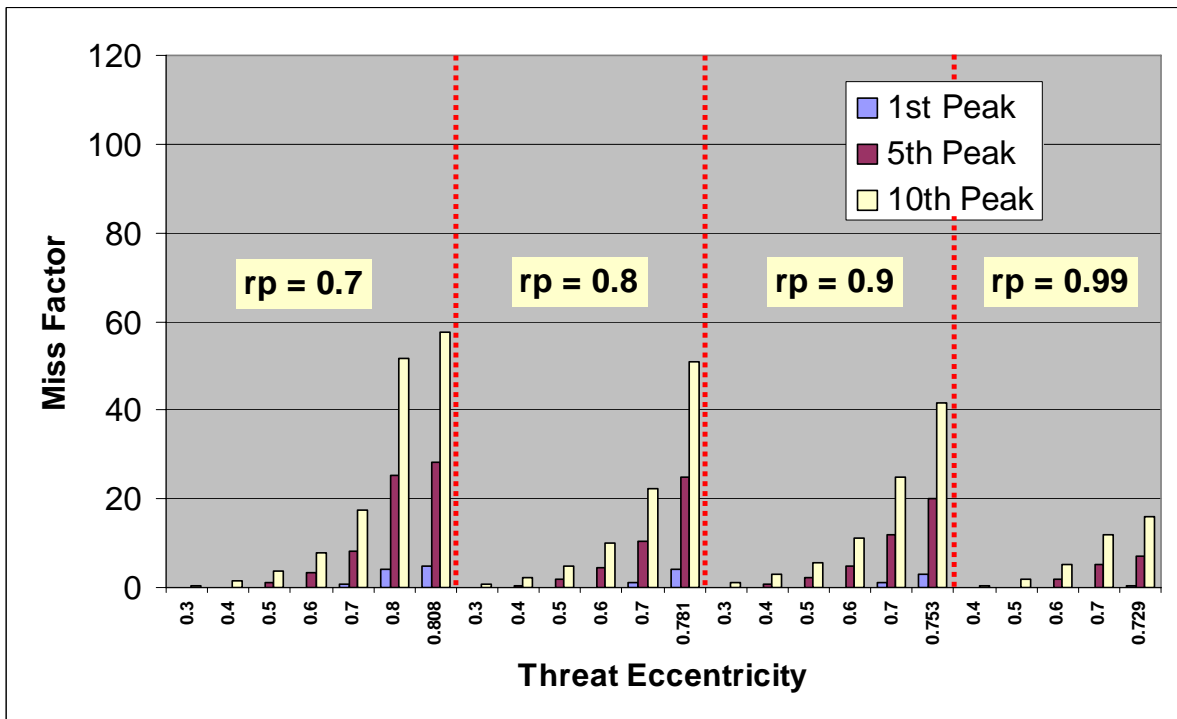


Figure 4-19: Threat displacement Margin in Terms of Miss Factor; High Perihelia



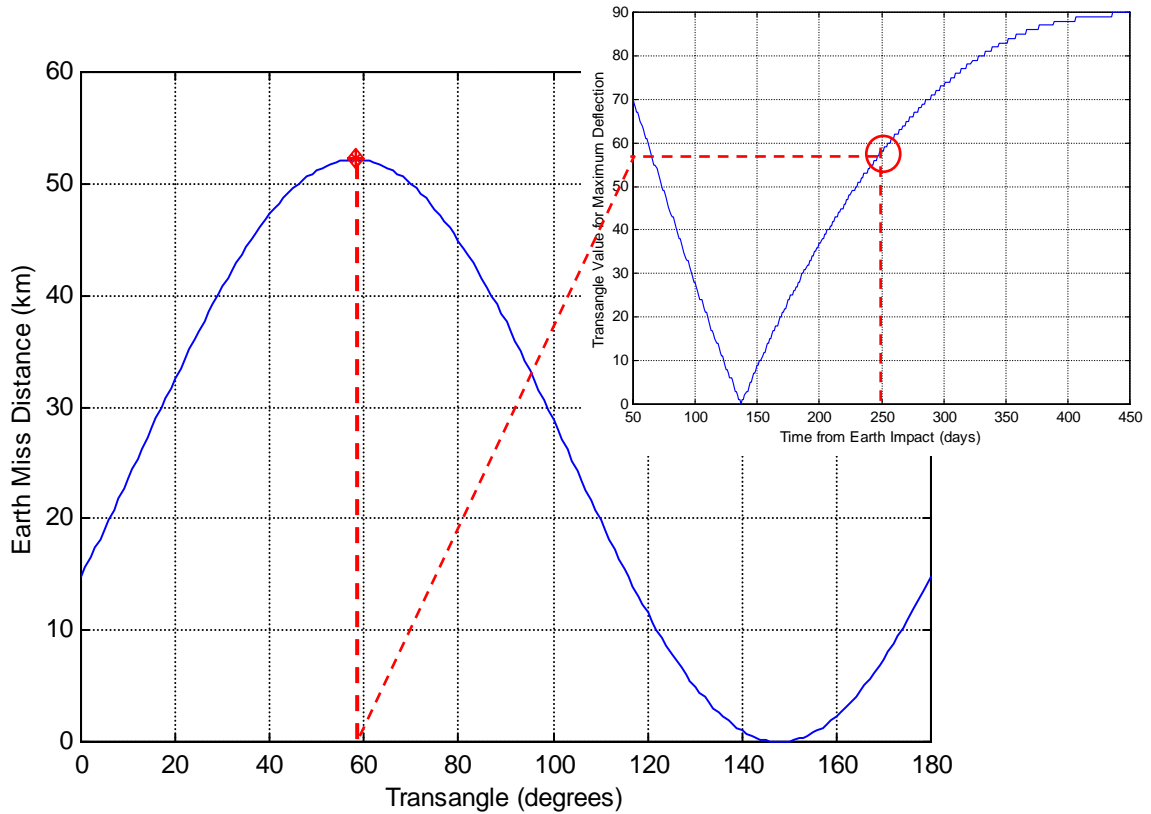
Of first note is that as threat perihelion increases, miss factor clearly shrinks. This is unfortunate, as Figure 3-10 showed that there are a greater number of threat objects at the high end of the perihelion scale. Also note that successful deflections occurring on the tenth peak always produce at least twice the margin as those occurring on the fifth peaks, and at least eleven times the margin as do first-peak deflections. Late deflections (i.e., those occurring closer to Earth impact) are possible, but again there is a clear motivation with respect to displacement margin to deflect as early as possible.

4.6 Optimal Deflection Direction

Figures 4-9, 4-11, and 4-13 showed that to maximize threat displacement for early engagements (i.e., those with long lead times) the deflection should be applied in a direction that is essentially aligned with the threat's orbital path. This, again, follows the planetary defense community rule of thumb, but does not do so in a strict fashion. This section explores the degree to which that rule of thumb can be applied.

The main plot of Figure 4-20 shows achievable threat displacement as it varies over the full range of Transangles for deflections of the example threat at 250 days prior to Earth impact. The corresponding optimal Transangle values for a broader timescale (from Figure 4-9) are repeated as an inset. Following the dashed lines from the peak of the curve in the main plot to the corresponding time in the inset plot demonstrates that the data indeed represent a deflection at 250 days before impact.

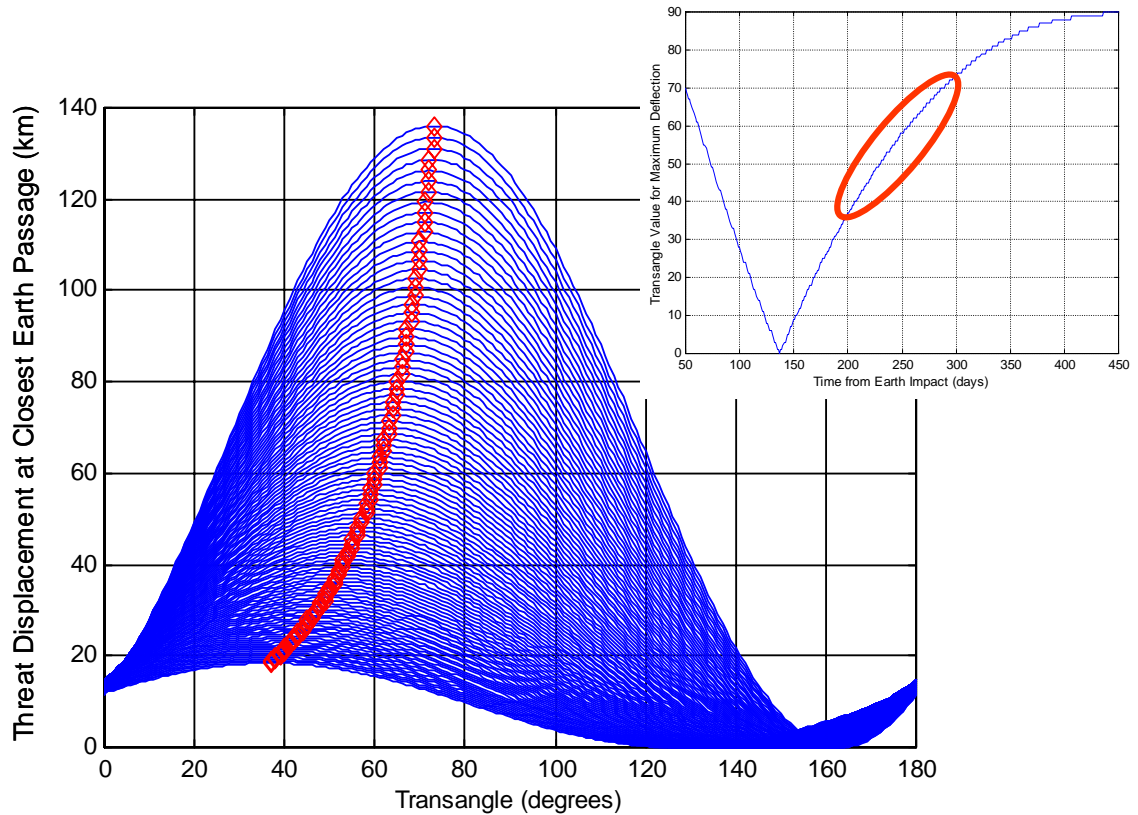
Figure 4-20: Example Threat Displacement over Transangle at 250 Days Before Earth Impact



Because 250 days is well after the last aphelion before impact, the peak deflection direction “rule of thumb” is not expected necessarily to apply: the deflection peak, marked by a diamond, occurs at a Transangle just below 60 degrees, well shy of the 90-degree rule-of-thumb value. Note also that the main plot of Figure 4-20 shows that a Transangle of around 150 degrees results in zero threat displacement: it is possible to go through all of the bother and expense of developing and deploying a perfectly viable defense system and wind up having absolutely no effect except perhaps to change slightly the time of Earth impact.

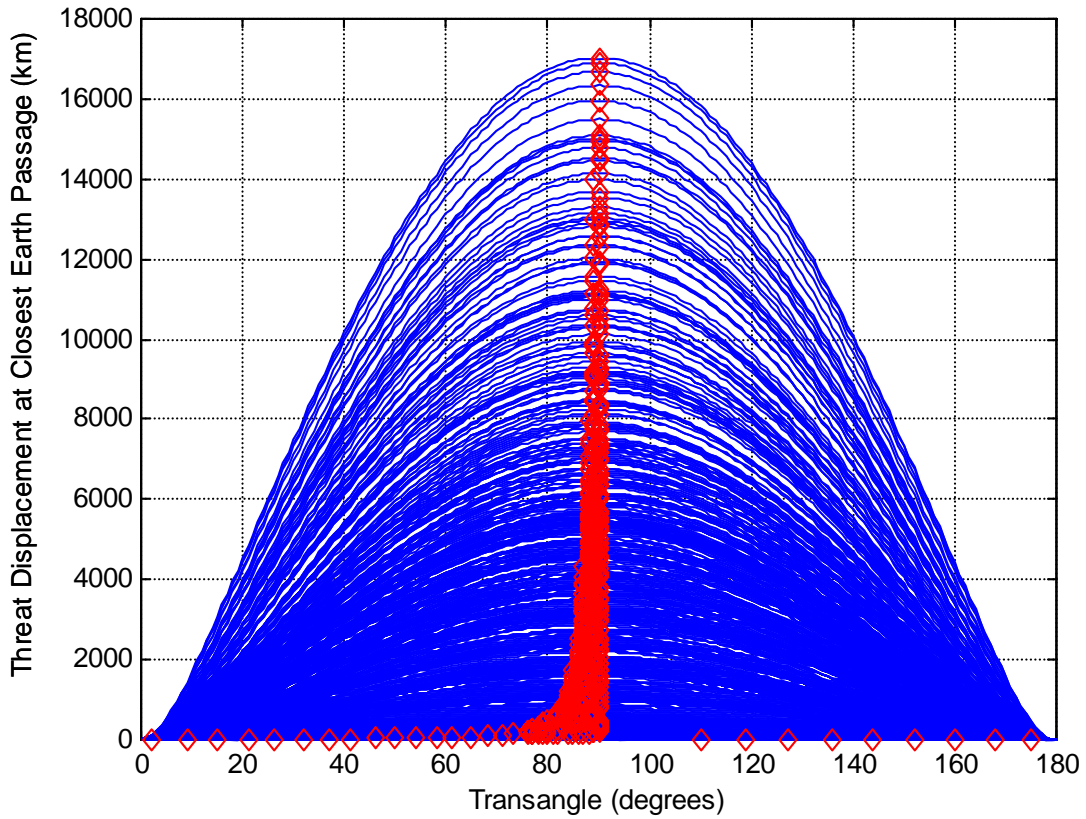
Running the simulation code that generated the main plot in Figure 4-20 over a range of deflection times and in 1-day increments results in the plot in Figure 4-21, and the local trend in maximum deflection direction begins to emerge.

Figure 4-12: Example Threat Displacement over Transangle from 200-300 Days Before Earth Impact



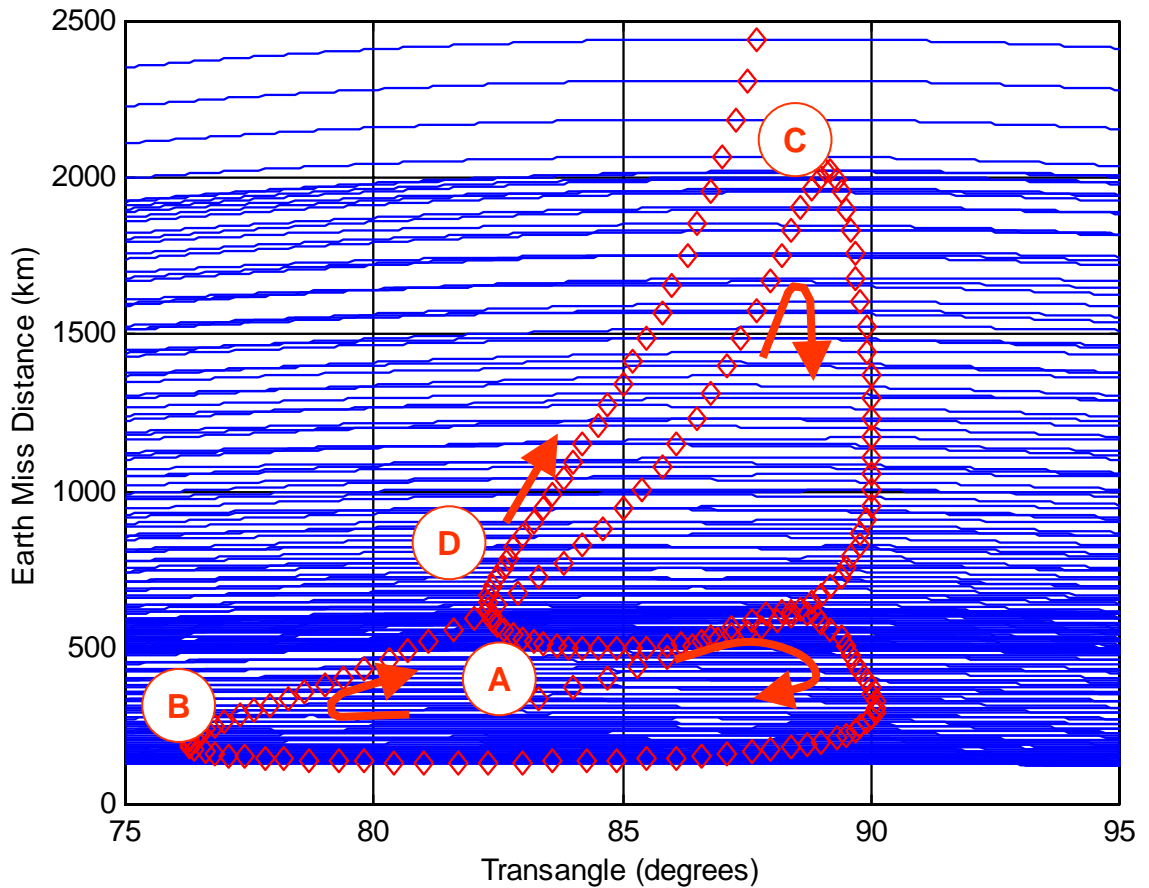
The trend continues to conform to that shown in Figure 4-9 (again supplied as an inset), and it holds over the entire 10-peak deflection period, as shown in Figure 4-22. Note that the “wrap around” of the peak points (i.e., the string of overlapping diamonds) along the bottom right of Figure 4-22 is a manifestation of the same angle accounting processes that caused the plotting discontinuities of Figure 4-9.

Figure 4-22: Example Threat Displacement over the Full Ten-Peak Range



The Transangles for early deflections clearly tend to cluster around 90 degrees, implying that the deflection-direction rule of thumb can be assumed to apply fairly well. However, with Figure 4-23 supplying a closer look at the data, a more varying pattern emerges. This data set was calculated so as to span only the last and second-to-last deflection peaks before Earth impact. It was run in 5-day increments, but at Transangle steps of 0.1 degrees to achieve a higher angular resolution.

Figure 4-23: Example Threat Displacement Over a Two-Peak Period



The point in Figure 4-23 marked with an “A” corresponds to the maximum deflection that can occur at 350 days before Earth impact, which, it is seen, demands a Transangle of around 83 degrees. With arrows indicating the direction along the trace for longer times before Earth impact, the maximum attainable displacements are seen to increase slightly at first, but then actually decline in spite of Transangle’s approach to 90 degrees. Continuing back in time along the path, the maximum-deflection Transangle drops rapidly toward a low value of around 76 degrees, marked with a “B” and occurring just before threat aphelion. Moving toward still earlier deflections, attainable displacement

again starts to rise and does so fairly precipitously as Transangle again drifts toward 90 degrees. Again, however, a threat displacement peak at point “C” is reached before a Transangle of 90 degrees is actually required, and again there is a rapid fall-off of attainable displacement. This trend of threat displacement bottoming-out followed by a retreat of Transangle repeats as the path moves back through point “D,” where Transangle reaches a local minimum of around 82 degrees, and continues again up toward the next-earlier peak, which is not viewable on this scale. It is concluded that the rule of thumb in question can be applied in the macro sense only. The pattern displayed in Figure 4-23 holds not only for the rest of the peaks of the example threat but also for the entirety of the representative threat set.

4.7 Angular Deflection Window

It is notable from Figure 4-23 that the overall attainable threat displacements at any one time before impact (i.e., the individual blue curves) are relatively flat over the 20-degree Transangle scale, indicating that close-to-optimal deflections might be achievable over what could be a fairly broad range of Transangle values. With the angular deflection window defined as that full-angle measure within which a deflected threat can be made to achieve at least 90% of the optimal threat displacement, Figure 4-24 gives the allowable angular error in deflection direction for a broad sampling of the representative threat set, including threats across the full range of inclinations.

Figure 4-24: Sorted Distribution of Angular Deflection Window

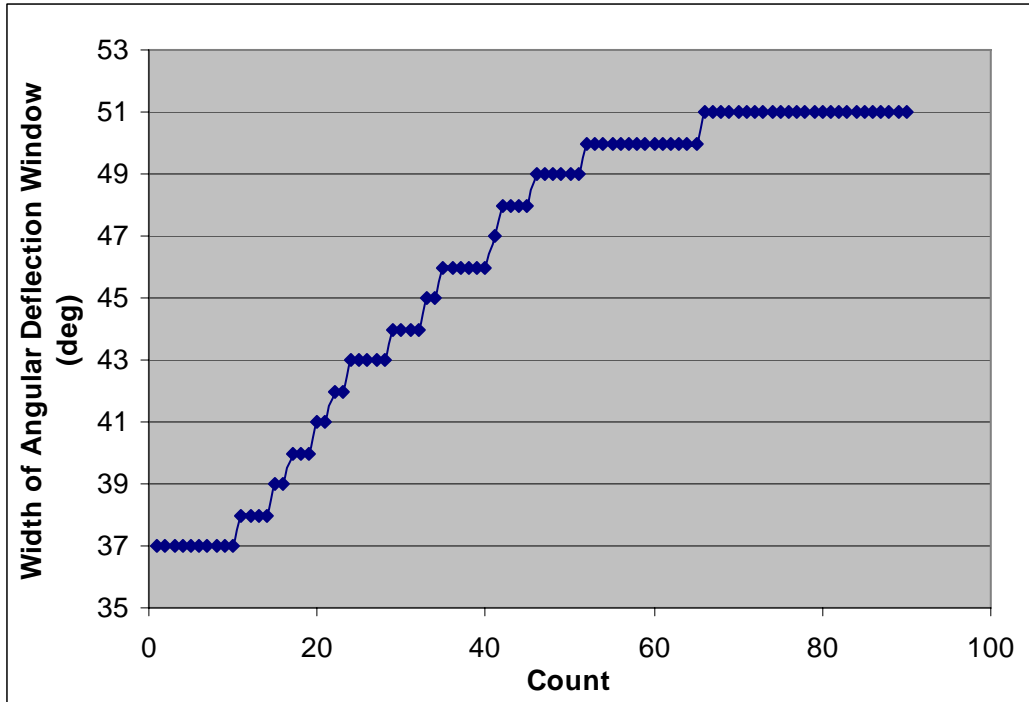
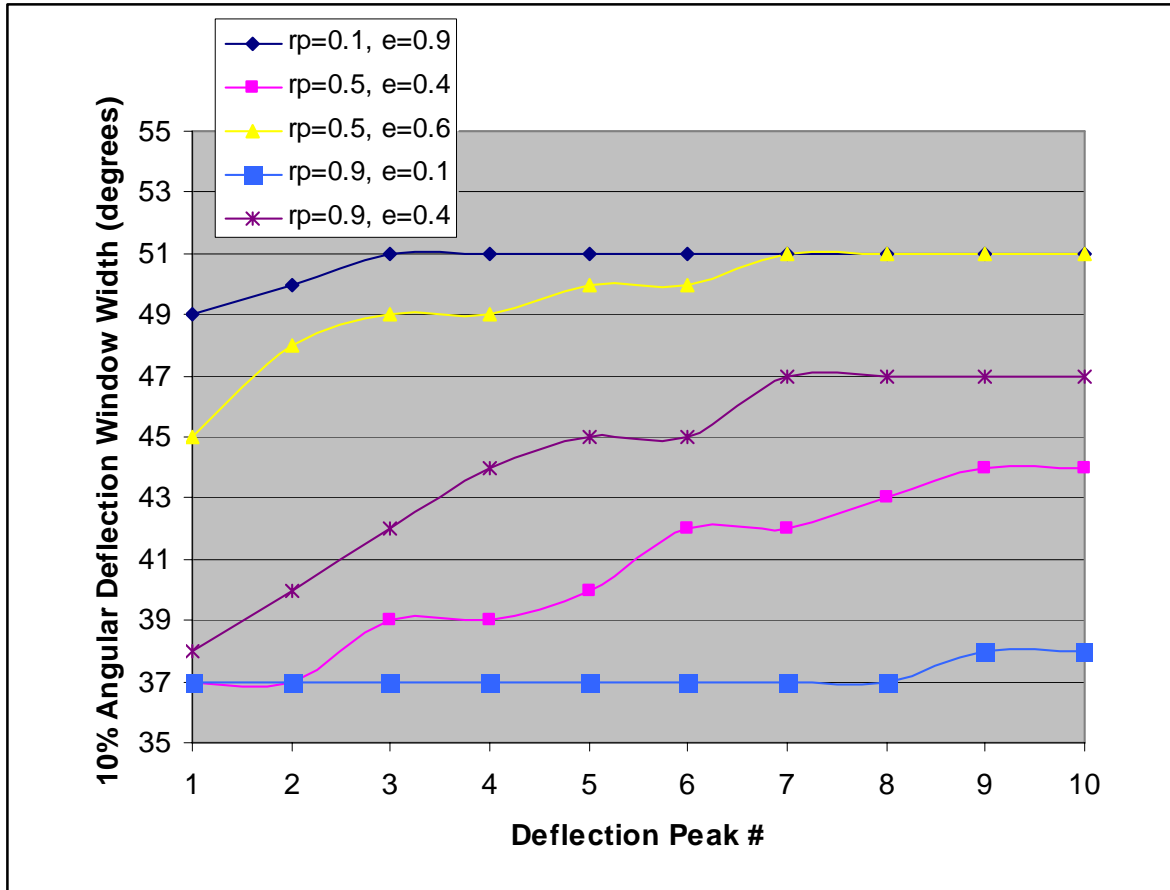


Figure 4-25 goes on to show the break out of required deflection angle among the perihelion/eccentricity pairings. For graphical clarity, this data set is presented for only zero-degree threat inclinations.

Figure 4-25: Angular Deflection Window Widths for Zero-Degree Threat Inclination



It is seen that angular windows are larger for threats with smaller perihelia, and that within any one perihelion-based threat family the angular window is likewise larger for both increasingly earlier deflections and for larger eccentricities.

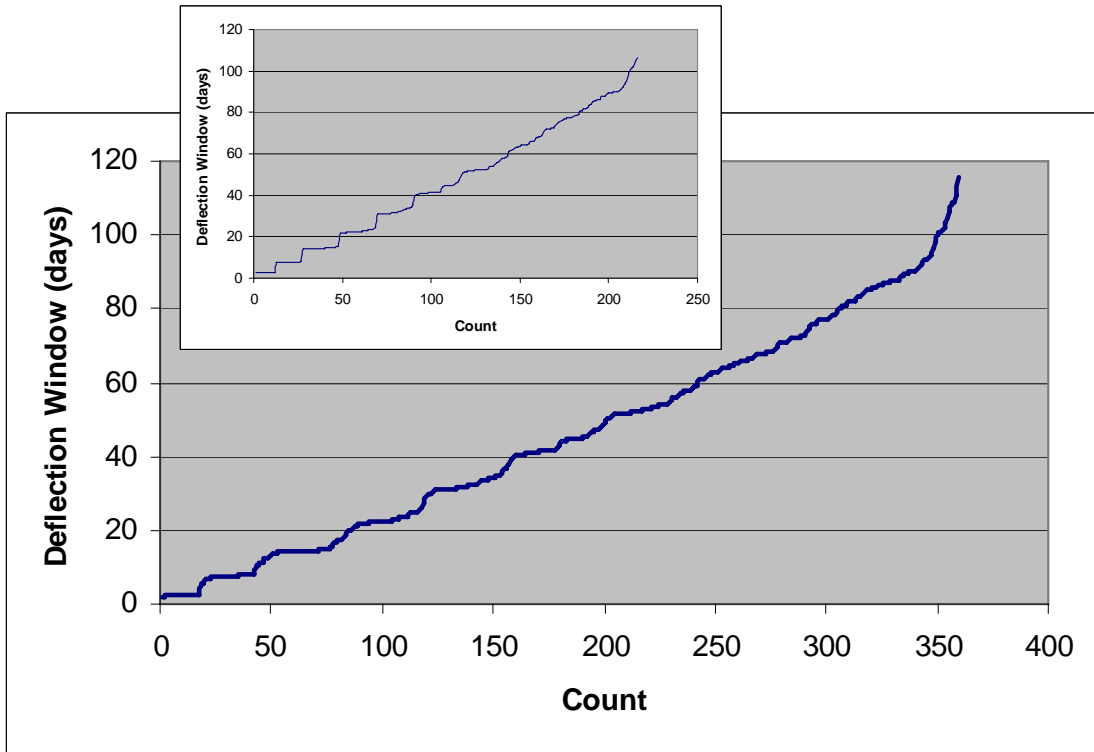
In general, the directional accuracy required of these deflections is seen to be fairly and perhaps even comfortably large across the entirety of the representative threat set, but only if the unknown nature of threat physical properties and behaviors is temporarily ignored. In actuality, the threat's topography, rotational or tumble dynamics, and internal makeup will most likely not be known to any great degree, producing considerable uncertainties as to the placement of the line of action of a deflection impulse and

therefore at least equal uncertainty in the ultimate direction of motion of the deflected object. These factors may well conspire to overtake any advantage that would have been gained from the flatness noted in the deflection direction curves.

4.8 Deflection Window Duration

To explore the deflection window's temporal bounds, deflection window durations were calculated at the first and tenth displacement peaks and for threat inclinations of 0, 25, and 70 degrees. All involved threat objects were included in the analysis regardless of whether the case at hand successfully generated an Earth miss. The sorted distribution of these window durations is shown in Figure 4-26, with the inset showing comparable behavior of the distribution if only successful cases are counted. The temporal window itself is defined as the duration within which a threat can be deflected and still result in at least 90% of the optimal threat displacement.

Figure 4-26: Sorted Distribution of Temporal Deflection Window



For the definition given, there are clearly numerous cases where the deflection window has a fairly comfortable duration. In fact, 95% of the threat has windows that are longer than 5 days. The stepped nature of the inset (i.e., the fact that there are no large fall-offs) shows that unsuccessful cases are represented fairly evenly throughout the field.

Figures 4-27 and 4-28 show the breakout of the temporal deflection window data, grouped according to the threat perihelion families, and show the duration of deflection opportunities at the latest and earliest (i.e., 1st and 10th) pre-impact deflection peaks, respectively.

Figure 4-27: Deflection Window Distribution for First Deflection Peak

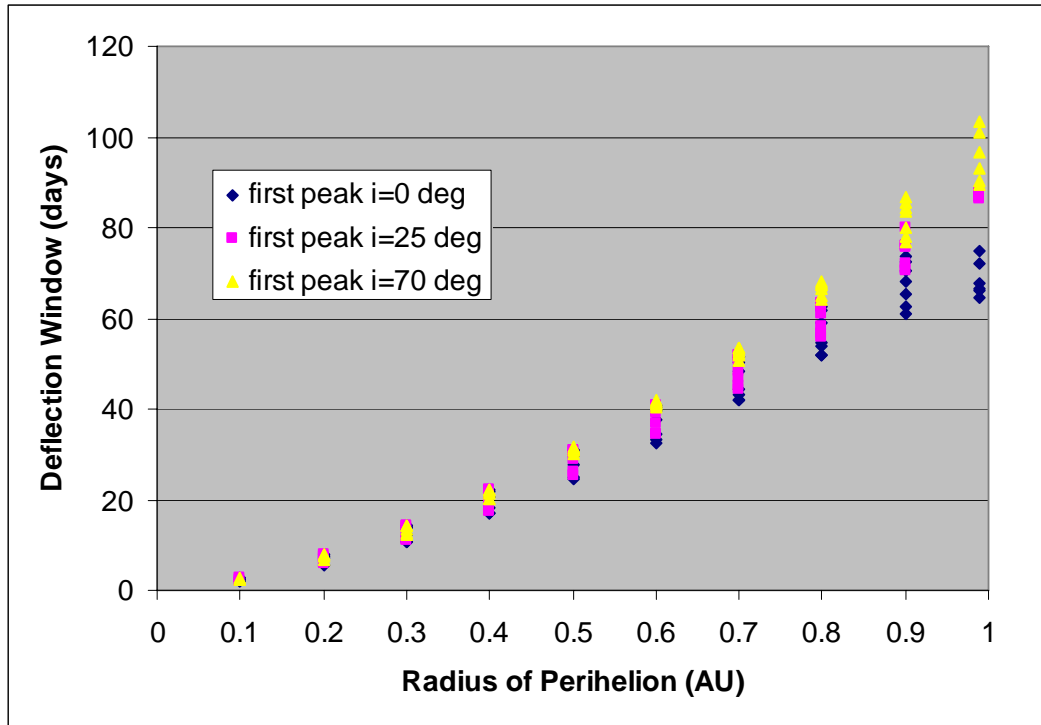
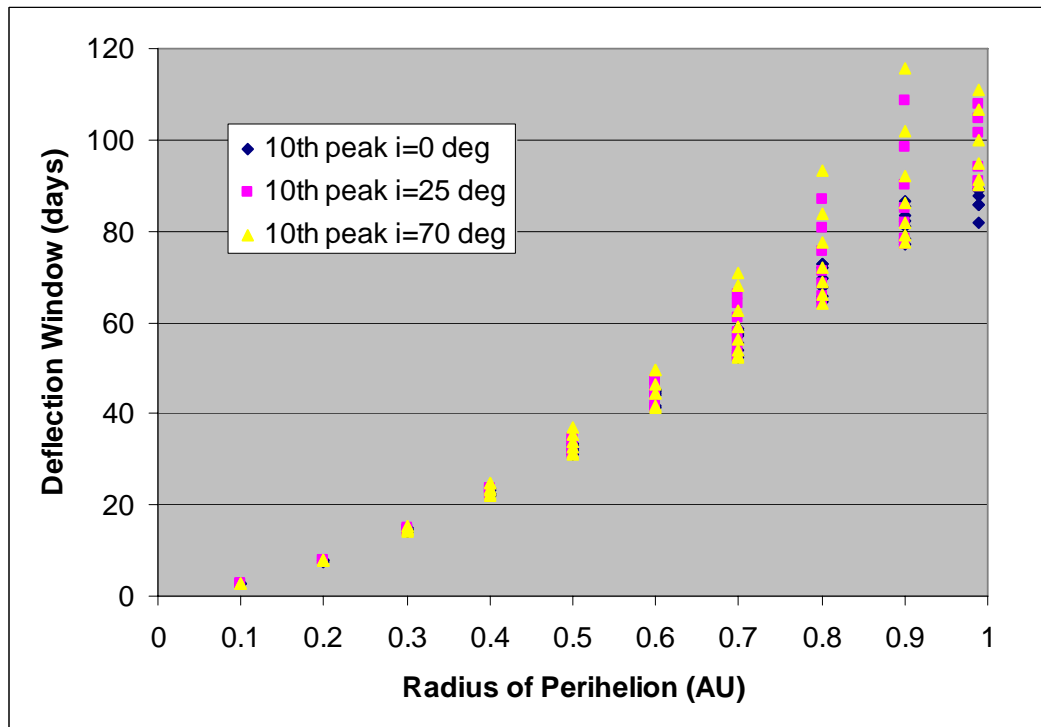


Figure 4-28: Deflection Window Distribution for Tenth Deflection Peak



Clearly the required accuracy of mission timing relaxes for threats of increased perihelion. Figures 4-29 and 4-30 delve farther into the behavior of threats with the most challenging (i.e., smallest) deflection windows. These figures show deflection window behavior over a smaller range of eccentricity, grouped according to inclination for the two smallest representative threat perihelia of 0.1 and 0.2 AU, respectively.

Figure 4-29: Deflection Window Behavior for Perihelion of 0.1 AU

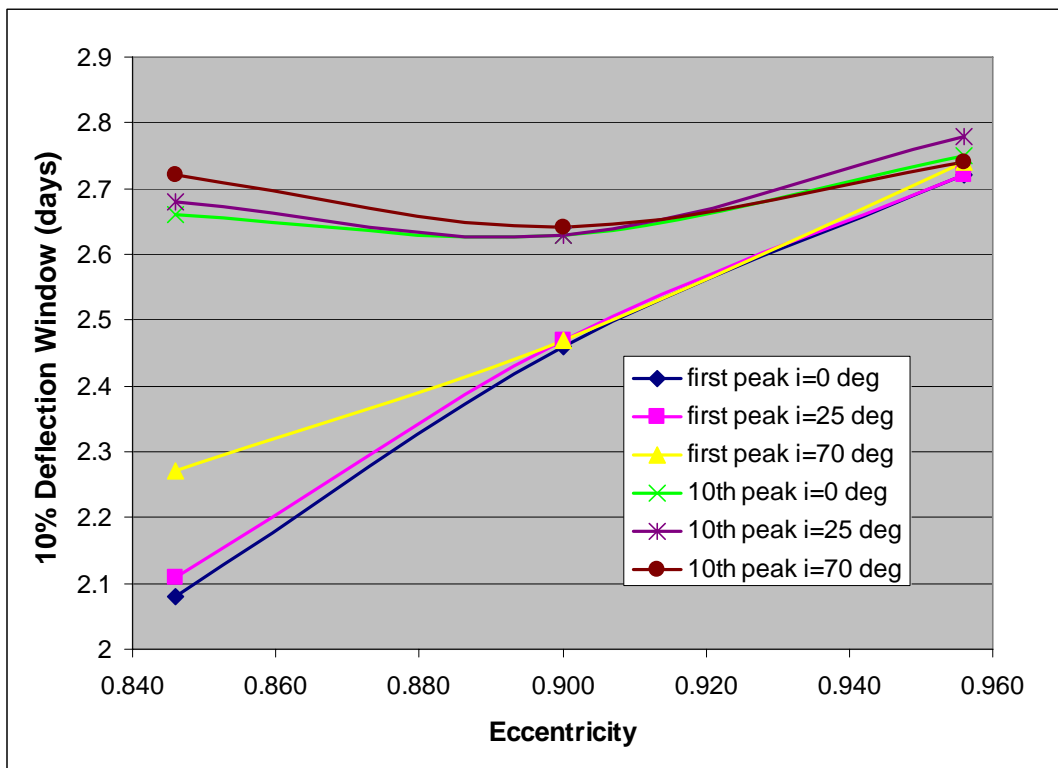
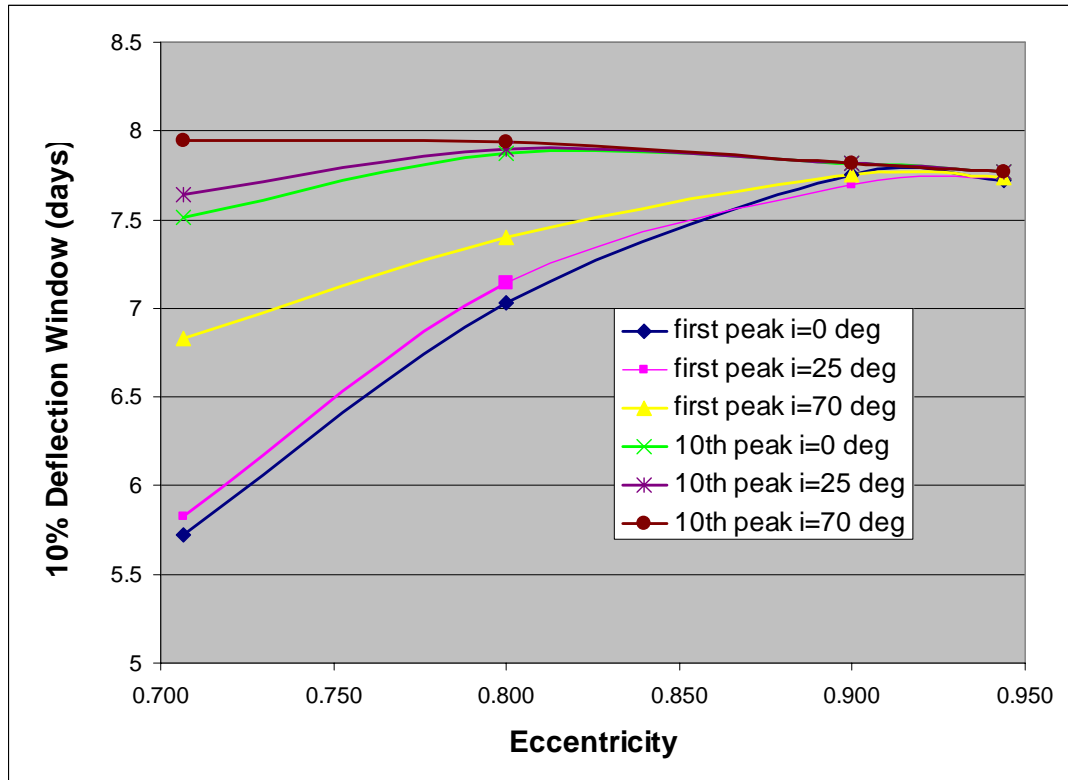


Figure 4-30: Deflection Window Behavior for Perihelion of 0.2 AU

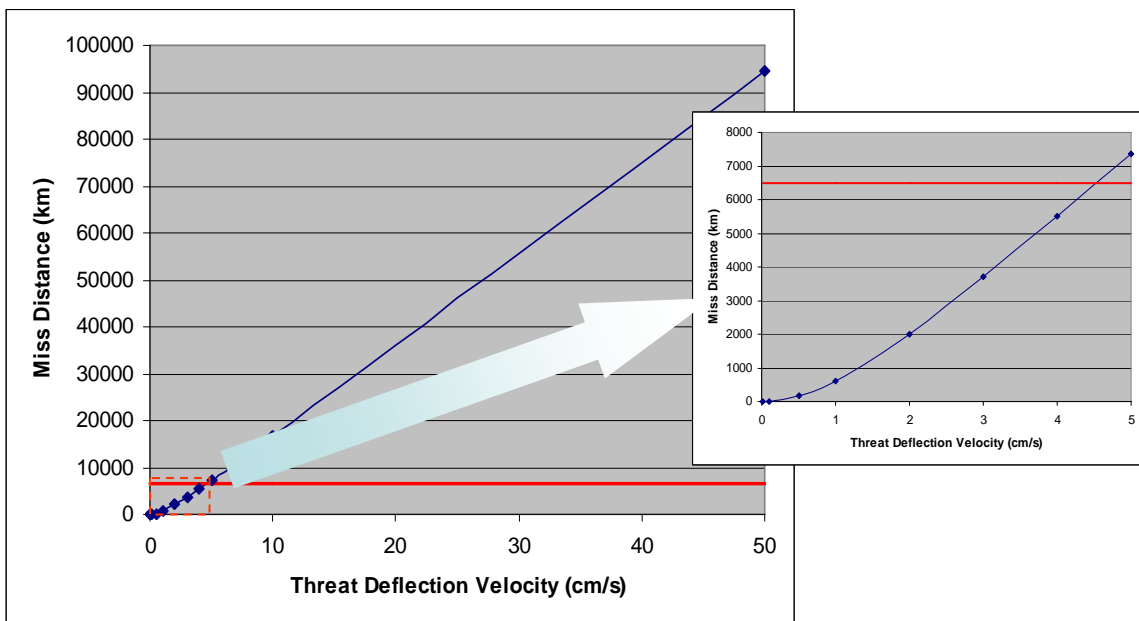


While there are a variety of trends in these plots and variations of those trends between the plots, the behavior of greatest importance is the sizable relative drop in the duration of the deflection window for any intercepts attempted with short warning times (i.e., “first peak” deflections), especially against low-eccentricity threats. There is some relief at higher threat inclinations, but the majority of asteroid threats have *low* inclinations: in accordance with the data of Figure 3-8, about half of the observed hazardous objects have inclinations below $8\frac{1}{2}$ degrees and almost 90% are below 25 degrees. As such, the relief offered against higher inclination threats will not often come into play.

4.9 Effect of Various Imparted Velocity Changes on Displacements

This section investigates the degree to which there is motivation to direct resources toward achieving larger threat deflection velocities as opposed to investing only in ways to achieve earlier deflection. Figure 4-31 shows two different scales of attainable threat displacement as it varies with increasing deflection velocity for first-peak deflections of the example threat; the horizontal lines in each plot show the 6488 km zero-margin Earth miss.

Figure 4-31: Effect of Increasing Deflection Velocity

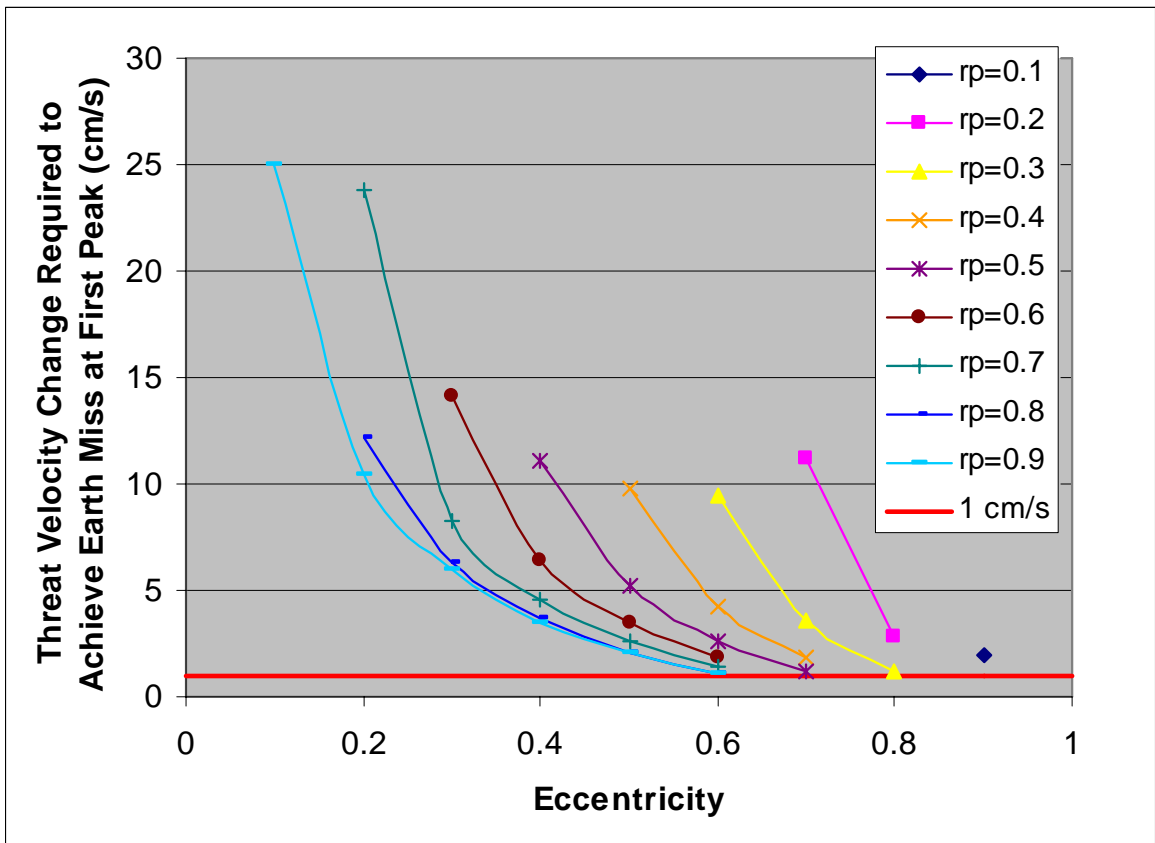


It is seen that it is correct to assume a linear change in attainable threat displacement over a wide range of deflection velocities. Note that while there is a slight non-linear tail off at the extreme low end of the deflection velocity scale, the velocities in the non-linear region are so small that they produced no threat displacements of any interest. This linear

behavior was found to hold across the entire representative threat space and for all deflection times, not just those producing peak values.

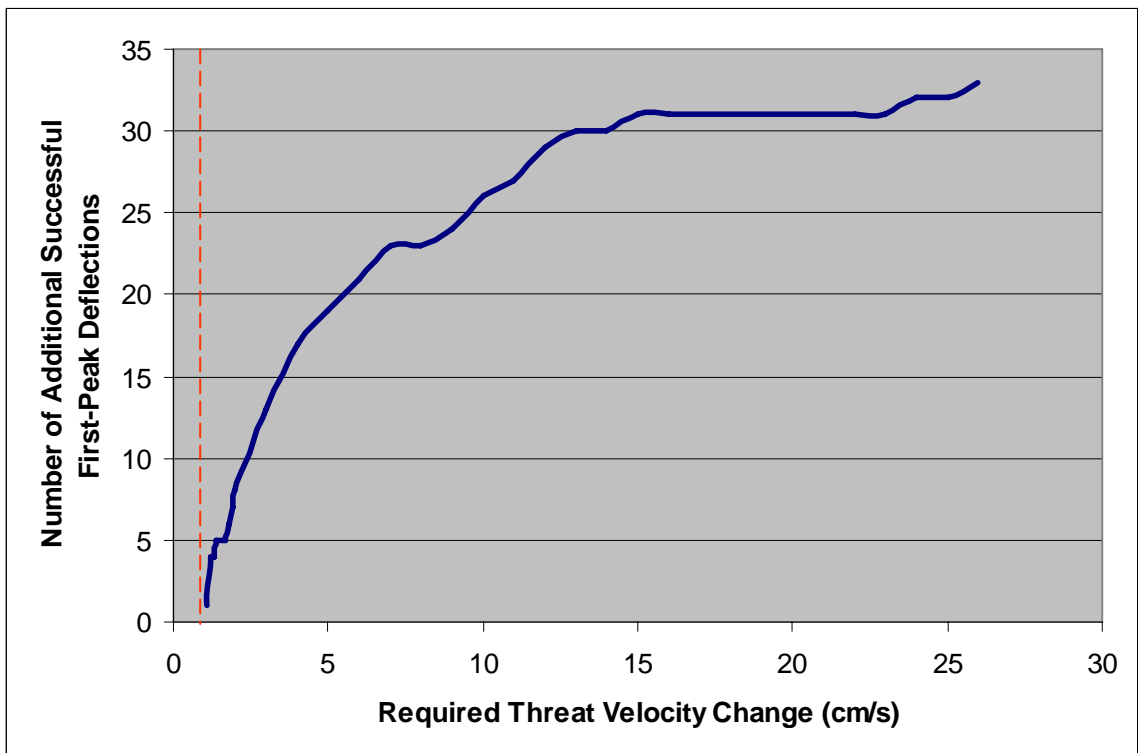
Figure 4-32 presents the deflection velocities required to achieve successful zero-margin Earth miss across the representative threat set at the final deflection peak before pending Earth impact. The cases shown are only those that would not have achieved successful Earth miss with only a 1 cm/s deflection. (The 1 cm/s threshold is indicated by the horizontal line near the bottom of the plot.)

Figure 4-32: Deflection Velocities Required to Recover a Full Earth Miss



The plot shows that taking advantage of all or even most of the described cases would require some fairly extreme deflection velocities, up to 25 cm/s for high-perihelion/low-eccentricity cases. This is because the objects at this end of the scale have periods approaching that of Earth, which, again, often results in an insufficient amount of time for threat deflection to accumulate to that required for an Earth miss. Of critical note, however, is that there exist many last-peak deflection opportunities waiting to be taken advantage of should deflection velocities be available that are even slightly above the 1-cm/s level. This is more clearly displayed in Figure 4-33, which presents the cumulative distribution of the imparted velocities contained in Figure 4-32. Any point on the curve represents the total number of previously unsuccessful last-peak deflections that would become successful at the associated threat deflection velocity.

Figure 4-33: Sorted Distribution of Threat Velocity Change Required to Achieve a True Earth Miss



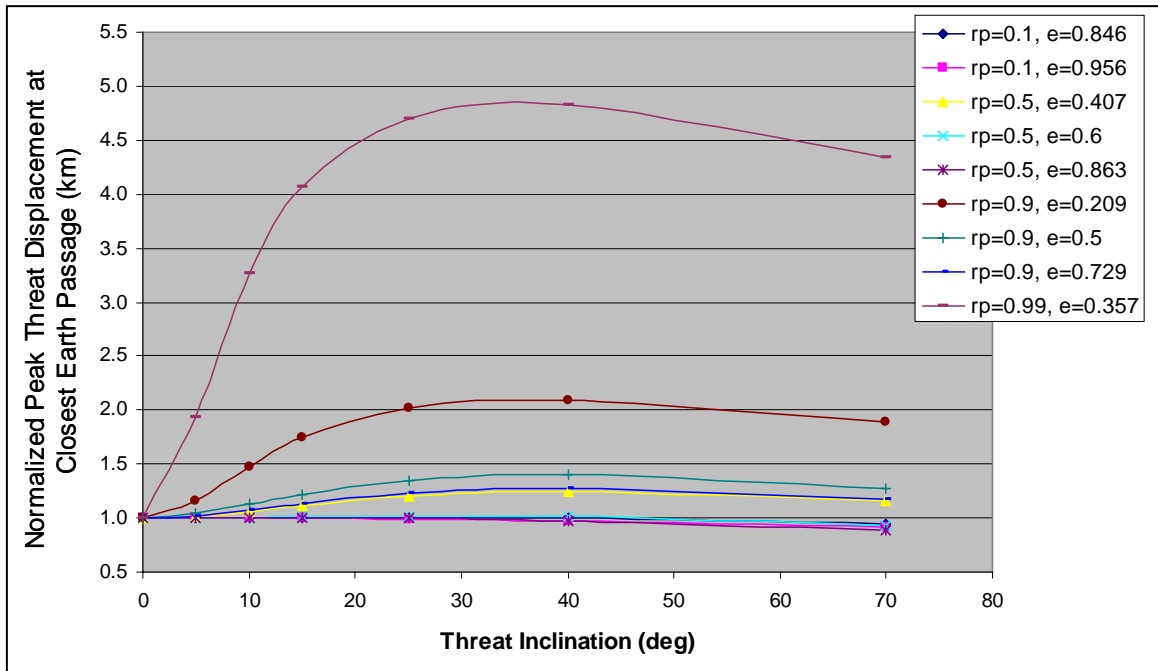
It is seen that relatively small increases in deflection velocity above the 1-cm/s baseline (i.e., the vertical dashed line) result in significant increases in the number of cases where successful displacement is achievable at the last peak before impact. Approximately 25% of the non-available cases are reclaimed with only a 2 cm/s deflection, and 50% of the cases are had for 4 cm/s. There is not significant motivation to go beyond that, however, as the cumulative distribution begins to lose slope. This is just as well, as serious questions should arise as to whether the kinds of deflection velocities represented by the upper portions of this curve would ever be achievable. This is not only from the standpoint of developing the mechanisms capable of generating and imparting the required energies, but also regarding the capability of the threat objects to withstand that imparted energy.

4.10 Threat Displacement Behavior Over a Range of Threat Inclinations

In general, the asteroid deflection data presented thus far have been for zero-degree threat inclination. As previously described, this is a moderately acceptable supposition, with the majority of observed threat objects having low inclinations. Still, because there are clear inclination dependencies in the calculated deflection data, as indicated in Figures 4-27 through 4-30, a treatment of threat displacement behavior with respect to inclination is in order.

Figure 4-34 shows the variation over inclination of the normalized threat displacements attainable at the last pre-impact deflection peaks. The normalization point for each perihelion/eccentricity combination is the first-peak threat displacement attained at zero-degree inclination.

Figure 4-34: Normalized Threat Displacement over a Range of Threat Inclinations

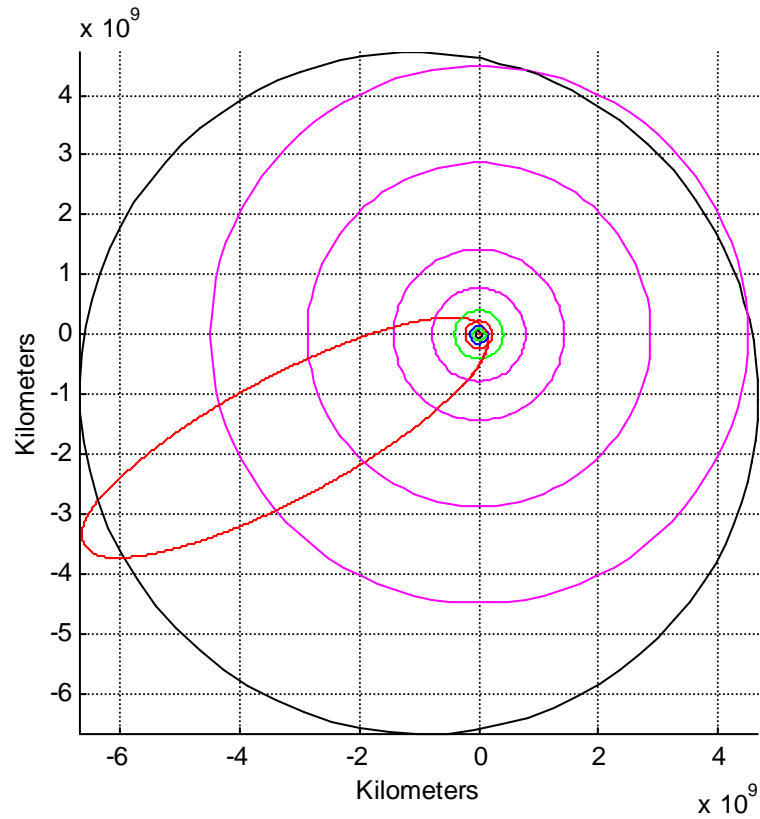


The data show that attainable threat displacement for threats with small perihelia and moderate to large eccentricities is relatively unaffected by threat inclination and in fact tails off slightly for the rarer high-inclination asteroid threats. However, for objects with the highest perihelia the effect of inclination becomes quite pronounced. Although its behavior still tails off for 70-degree threats, normalized threat displacement rises dramatically for very large perihelia and low eccentricity. These behaviors would motivate a resource allocation trade between enhancing the surveillance approach to more thoroughly search for what will be rarer but often more assuredly deflected high inclination threats, and being better prepared for the more numerous low-inclination threats that are more difficult to deflect.

4.11 Comet Deflection Example Case

As discussed earlier, it is thought that the Oort Cloud and the Kuiper Belt contain between them many billions and perhaps a trillion comets, some of which are occasionally driven free of their existing orbits, dive toward the inner planets, and are re-stabilized in lower orbits as one of the familiar periodic comets. If pending Earth impact by one of these periodic objects is discovered many threat orbits in advance, it would be expected that the capability to successfully deflect it might follow roughly the same general trends that have been determined and reported herein for the deflection of asteroids. An issue of more tactical significance, however, is whether a reasonable threat velocity change would generate a successful displacement against a comet that is not discovered to be headed for an Earth impact until it is past its last aphelion. To explore this, a representative Kuiper object with zero-degree inclination was created and placed so as to begin its descent from the outer edge of the Belt, at 50 AU from the Sun. An eccentricity of 0.963 was selected so as to force perihelion down to approximately 0.94 AU (the actual figure used was 0.94245 AU), thus ensuring that the Earth's orbit was indeed crossed. The resulting object has a period of about 130 years. The comet's orbit, adjusted in longitude of ascending node to assure an Earth impact at autumnal equinox, is shown in Figure 4-35. The small green orbit is that of the Asteroid Belt.

Figure 4-35: Comet Threat Case



The same code set used in the preceding asteroid displacement analysis was applied to this cometary threat to generate optimal displacement and associated Transangle curves. These were developed for 1 cm/s deflections out to 5000 days before impact, and are shown in Figures 4-36 and 4-37, respectively.

Figure 4-36: First Successful Mitigation for Example Comet Threat Case

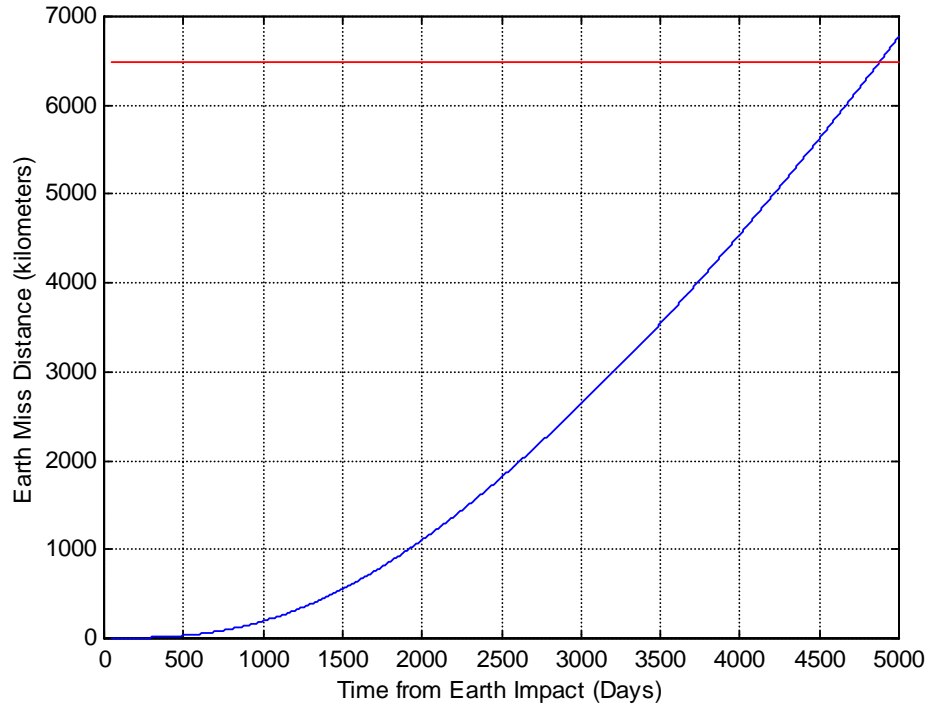
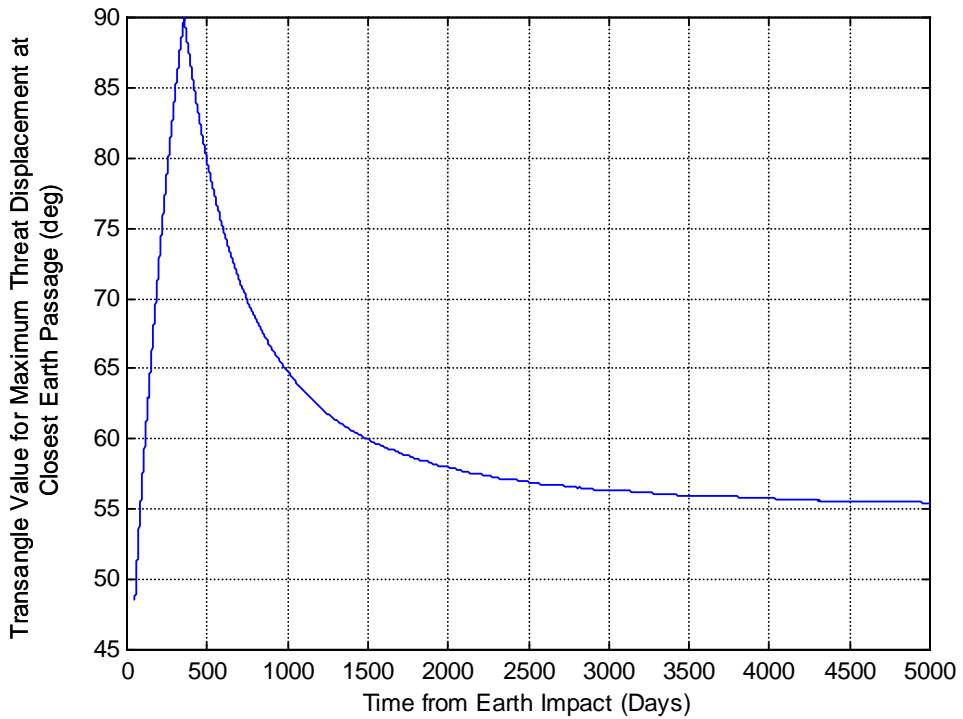
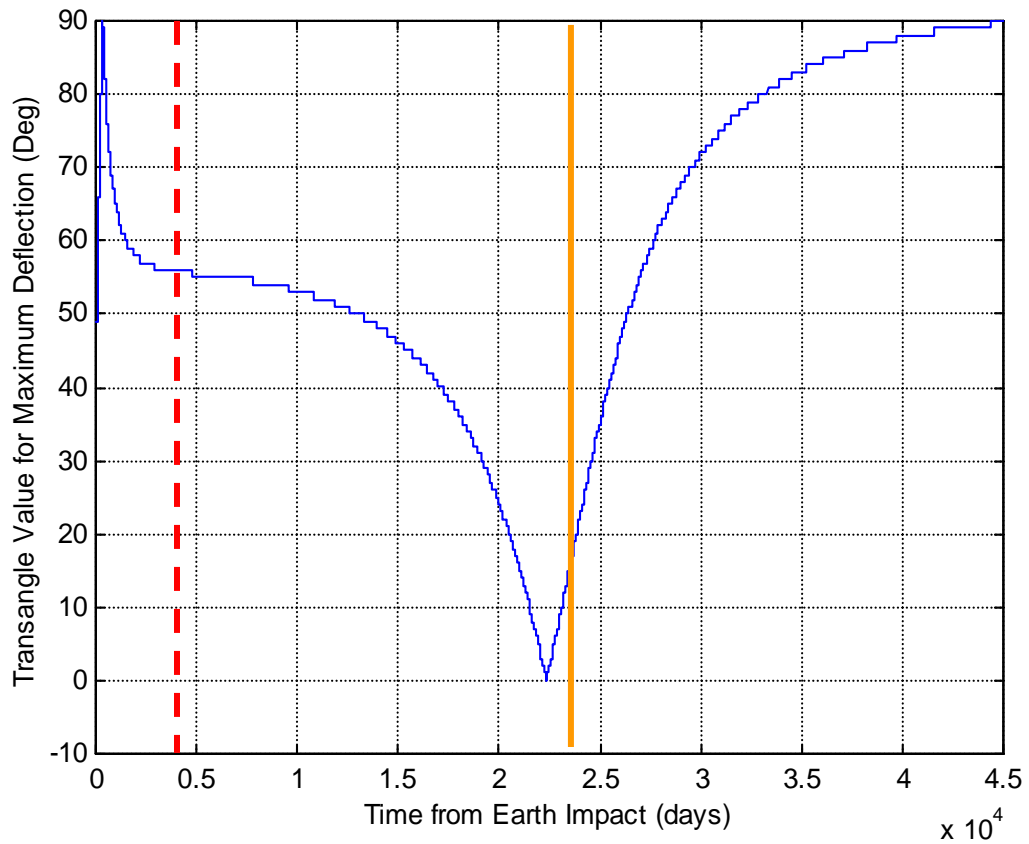


Figure 4-37: Transangle Values Required for Maximum Threat Displacement Against Example Comet Threat



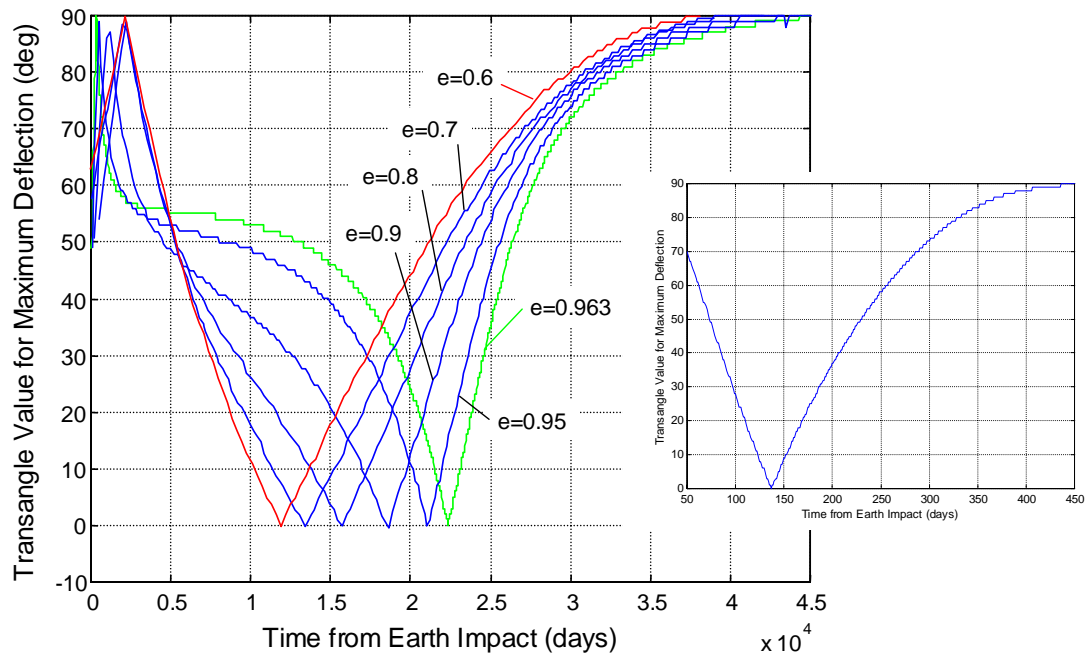
From this data it is seen that to achieve even a zero-margin Earth miss, a 1 cm/s deflection must be imparted at least 4874 days or well over 13 years before Earth impact. For comparison, that amount of lead time gave a displacement margin factor of around 2.5 for the example asteroid threat. For the given comet orbit, the Transangle values for optimal displacement from deflections reaching to its perihelion are shown in Figure 4-38, with the solid vertical line indicating the location of the object's aphelion.

Figure 4-38: Transangle Values Required for Maximum Threat displacement against Example Comet Threat



It is seen that Transangle would make the expected rise to essentially 90 degrees as deflection time is pushed back from threat aphelion to perihelion, as it did for the example asteroid. Beyond that, however, cometary Transangles appear to behave rather differently from those of the example asteroid case, stalling for a significant amount of time near the 55-degree mark during final descent. This is of particular note as this flattened area contains the time of latest possible deflection, indicated by the dotted vertical line in Figure 4-38. As is shown in Figure 4-39, however, the Transangle pattern can be shown to transition smoothly from this cometary case down to the familiar pattern presented earlier for asteroids.

Figure 4-39: Transition in Transangle from Cometary to Asteroid Threats

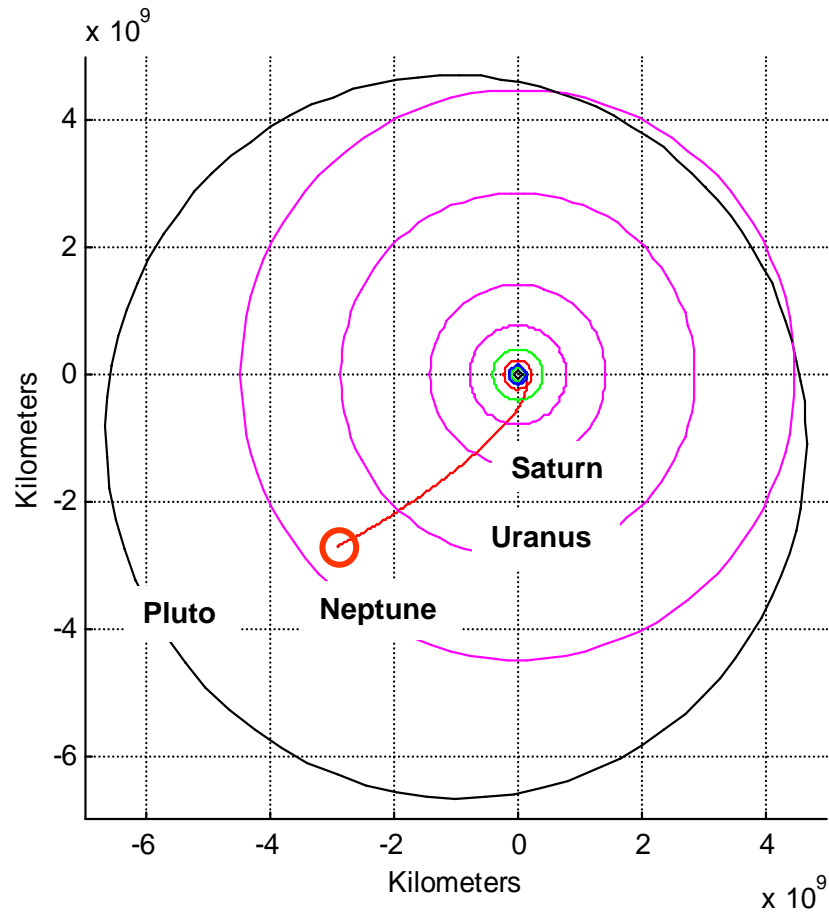


This data set was developed by holding threat perihelion to that value established for the comet threat, decreasing eccentricity incrementally from the comet's 0.963 down to 0.6,

and then normalizing the data to the time of last pre-impact perihelion for *each* test threat. As eccentricity drops, the Transangle pattern approaches that of the example asteroid threat, as shown in the inset. The flattening in Figure 4-38 appears to be a manifestation of the fact that when comets such as this are in their long and only slightly-curved post-aphelion approach, the change in direction of threat path occurs extremely slowly: it would be expected that the optimal direction of deflection would change at the same pace as does the geometry of approach.

Although Figure 4-36 showed that cometary deflections are kinematically possible, at least by the assumptions given, a notable difference from the asteroid cases is the distance from Earth at which a 1-cm/s deflections must take place to create an Earth miss. For the example asteroid discussed in Section 4.1, required deflection location was shown to be very close to the orbit of Venus, a location of fairly relative convenience. The required deflection location for the example cometary threat is nearly to the orbit of Neptune, as shown in Figure 4-40.

Figure 4-40: Required Deflection Location (1 cm/s) for Earth Miss of Example Comet Threat



The operational differences between executing a deflection mission near the orbit of Venus and doing so most of the way to Neptune are radical. Most notable is that while the worst case round-trip communications delay from Earth to a mission at Venus' orbit is a little under 30 minutes for Earth-Venus conjunction, the minimum delay for the described comet mission would be almost 7½ hours. This difference could mean orders of magnitude in required sophistication for any pre-impact threat characterization activity and in overall mission automation. This and the extensive flyout time would motivate very early detection of such objects, a difficult task as the comet would not be expected

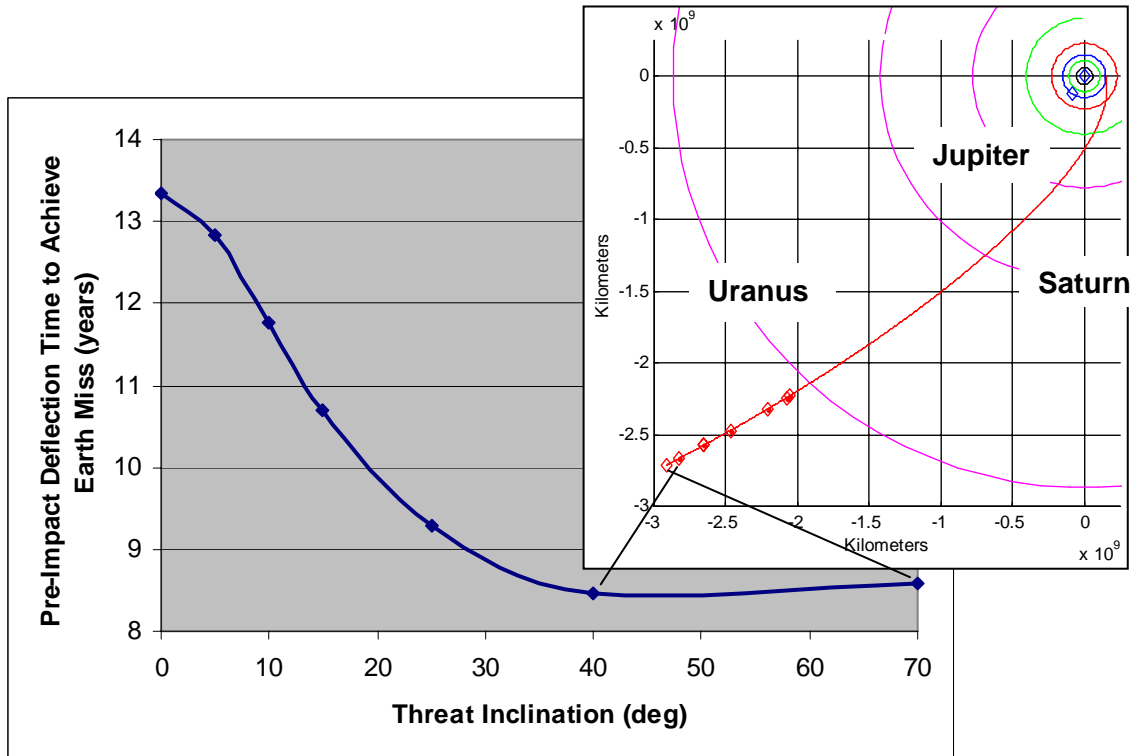
to be producing an observable tail that far from the Sun. If interceptors are pre-deployed in the regions where these intercepts would have to take place, there is still the fact that a heliocentric ring at Neptune's orbit would be almost 155 billion kilometers in circumference. If interceptors are emplaced no more than 1 AU apart, over 1000 of them would be needed. Some relief is provided on the basis of the threat's orbital mechanics: heliocentric velocity of this Earth-bound comet when it is still in the neighborhood of Neptune is less than 5 km/s, as opposed to a heliocentric velocity of over 40 km/s at Earth impact. As such, if, say, 3 years are required for an interceptor flyout to the threat, it would push the requirement for threat detection back only to essentially Neptune's orbit, assuming that a mitigation mission is sitting on the pad and ready to launch as soon as warning is received. The regret of the low threat velocity, however, is that earlier statements on the efficacy of achieving 1-cm/s deflections relied on a large threat velocity to achieve sufficient interceptor kinetic energy. That high relative velocity being absent, nuclear means may be required for cometary deflection.

4.12 Comets and Inclination

While Kuiper objects are biased toward posigrade ecliptic motion, there is still some chance that whatever encounters caused the cometary example object to dive toward Earth also had a sizable effect on its inclination. The trends for displacement behavior with respect to threat inclination that were presented for the asteroid threat hold also for the cometary threat, although Figure 4-41 presents this in an inverted fashion. The figure shows that an Earth miss with a 1 cm/s deflection can almost always be achieved later (i.e., closer to Earth impact) when dealing with comets with higher inclinations. The data

points on the time curve correspond to the threat locations in the orbit plot: note the order inversion after the 40-degree inflection point.

Figure 4-41: Variation over Threat Inclination of Deflection Time Required to Produce an Earth Miss



Chapter 5 - Mission Design Conclusions

5.1 Mission Design Considerations

It is found that even for a relatively conservative 1-cm/s deflection velocity, successful deflections are achievable against a large portion of the asteroid threat for engagements occurring up to 10 threat orbits before Earth impact. The percentage of the representative PHA threats against which defense should be available is as high as 68% when calculated as a count of successful peak deflection opportunities over the broadly representative parametric PHA threat set. The actual warning times will vary with the period and general observability of the threat object in question, but real-world projections have tended to offer warning times that can be significantly greater than just 10 threat orbits. If a surveillance component is developed that is capable of a warning time of 20 orbits, nearly 80% of the threat can be handled at 1 cm/s.

The common assumption that earlier threat deflections result in larger threat displacements at Earth passage is clearly and not surprisingly supported. The expected rise and fall in attainable displacement as deflection events approach and recede from threat perihelion is also supported.

It was discovered that there are many opportunities for successful 1-cm/s deflections against threats that have already entered their last orbit before Earth impact. However, no successful deflections are available after the threats have passed their final pre-impact aphelion (i.e., when those threats are on their “final approach”). It was also found that successful Earth miss is more easily achieved against threats with low perihelion.

Many high-margin deflection opportunities were discovered, but only against threats with higher eccentricities. Deflections occurring as far back as the 10th peak before impact generally give twice the margin as those occurring on the 5th peaks, and at least eleven times the margin of 1st-peak deflections. Late deflections (i.e., those attempted closer to Earth impact) can be successful, but there is clear motivation from the point of view of threat displacement margin to deflect as early as possible.

Although the miss distance results calculated for this paper were presented from the standpoint of single threat deflection events, scenarios could easily arise that would call for multiple deflection events occurring well separated in time [9]. If, for instance, an impact threat is discovered many orbits in advance, but a “near-term” mitigation mission cannot be executed in time to produce a maximum displace on the threat’s current trip around the Sun (i.e., it cannot reach threat perihelion before the threat has passed), the mission might still be flown to an engagement at some non-optimal location in order to achieve at least some deflection and perhaps to provide some diagnostic data on the threat. Certainly a second mission (or perhaps more) would be executed to provide additional miss margin or, as a worst case, *some* miss margin; such follow-on engagements should be timed so as to produce optimal deflections, even if that means delaying the engagement.

The outcome of a cumulative series of deflections can be estimated directly from the data provided in this paper, as they would be additive in nature. Figure 4-12, for instance, showed that the example threat must be prosecuted at least the fifth or sixth deflection peak prior to Earth impact (up to 7.5 years out) in order to achieve any Earth miss. If, however, a deflection at that sixth peak is then followed up by one at the fifth peak, the

cumulative Earth miss distance would have a margin of over 100% (i.e., miss the Earth by over 100% of its radius plus atmosphere), otherwise achievable by a single deflection only if it took place almost ten years out. Likewise, 1-cm/s deflections could be applied against the example threat as late as five years before Earth impact, and achieve a miss margin of over 80% simply by deflecting at each of the four deflection peaks closest in time to Earth impact. This is of particular note because, as was also seen in Figure 4-12, none of those four peak deflections by themselves would have been able to achieve an Earth miss.

The common assumption that the imparted velocity for early threat deflections (i.e., those occurring many threat orbits before impending Earth impact) should be along the threat's velocity direction is supported in general, but it was shown that it could not be applied strictly. The variation of optimal deflection direction over time is shown to be cyclic in nature, but also to be convergent for deflections occurring earlier and earlier. The behavior of threat displacement as a function of deflection direction was shown to display even more complex features as this convergence takes place.

The accuracy required of the deflection direction was shown to be fairly relaxed with at least several tens of degrees of full angle available while still achieving at least 90% of the maximum attainable displacement, higher against threats with smaller perihelia and larger eccentricity. There is also an angular window advantage for deflections applied increasingly early, but this trend will be challenged by the dynamic and structural character of the threat objects, which are expected to be both highly uncooperative and probably fairly unknown.

The temporal width of the threat window, also defined as that which causes only a 10% reduction in the maximum attainable displacement, is likewise often rather comfortable, ranging fairly continuously from a few days to well over a hundred days over the representative threat set.

One of the more contentious resource allocation trades in planetary defense will be that between investments to enable increasingly earlier deflections (a major portion of which would be spending to enhance surveillance efforts), and those that would enable larger deflections. This trade becomes especially contentious when it is realized that if these larger deflections are to be achieved in the near term, they might best be achieved through the use of nuclear devices. It was determined herein that there are a large number of deflection opportunities to be had for only small increases in deflection velocity above the 1-cm/s level. It was shown that that 50% of unsuccessful engagements can be regained if 4-cm/s deflections are possible. Although the return diminishes quickly beyond that, there is still significant motivation to increase deflection velocity.

Much of the data presented herein were calculated for defense against zero-degree-inclination asteroid threats. It was shown that enhanced displacements result from 1-cm/s deflections against inclined threats, especially for objects with high eccentricity and low perihelion.

With respect to defense against cometary threats, it was shown that successful deflections are possible at the 1-cm/s level, but that these must occur well out in the solar system. Such missions, which may have to occur essentially at the distance of Neptune, would be of elevated complexity due to extreme round-trip communications delays and the implied high-degree of mission autonomy. Flyout time is also a daunting challenge

for such missions, and any plans to pre-position interceptors must contend with the enormous volume of space that would have to be patrolled at that distance from the Sun.

5.2 Follow-on Work

Potential next steps fall into two categories: filling in points of interest with respect to the trends and behaviors discovered for and captured in this paper, and expanding the overall mission design effort. Points of interest deserving additional attention include the development of a representative parametric cometary threat set and an attending expansion of the treatment of the cometary threat in general. Regarding the asteroid treatment presented herein, additional work needs to occur to more fully characterize capability against inclined threats; to determine displacements available with long-duration, low-threat deflections; and to treat more broadly the analyses on deflection timing, direction, and deflection velocity.

With respect to the overall mission design effort, it would be of interest to develop a set of end-to-end mission descriptions against a broadly-representative threat set, to include development of various fly-out options and an assessment of how those might be optimized so as to take advantage of convenient Earth-to-threat positions over time and advantageous intercept geometries that maximize the threat-relative velocity of the interceptor to likewise maximize available deflection kinetic energy.

Finally, in order to create a more salient statement on our capabilities, it would be of extreme importance to estimate the true timeframe for accurate projection of the impact threat as it varies over the span of PHA orbits, and to then recalculate the percentage of

the threat against which it is believed that an effective planetary defense mission could be mounted.

References

- [1] Adushkin, V. and Nemchinov, I. "Consequences of Impacts of Cosmic Bodies on the Surface of the Earth." *Hazards Due to Comets and Asteroids*. Ed. Tom Gehrels. Tucson, The University of Arizona Press, 1994.
- [2] Ahrens, T., and Harris, A. "Deflection and Fragmentation of Near-Earth Asteroids." *Hazards Due to Comets and Asteroids*. Ed. Tom Gehrels. Tucson, The University of Arizona Press, 1994.
- [3] Alvarez, L., Alvarez, W., Assaro, F., and Michael, H. "Extraterrestrial Cause for the Cretaceous-Tertiary Mass Extinction." *Science*, **208**, pp. 1095-1108.
- [4] Atkinson, H., Tickell, C., and Williams, D. "Report of the Task Force on Potentially Hazardous Near Earth Objects." 2000.
- [5] Bailey, M., Clube, S., Hahn, G., et al. "Hazards Due to Giant Comets: Climate and Short-Term Catastrophism." *Hazards Due to Comets and Asteroids*. Ed. Tom Gehrels. Tucson, The University of Arizona Press, 1994.
- [6] Bate, R., Mueller, D., and White, J. *Fundamentals of Astrodynamics*. New York, Dover Publications, Inc., 1971.
- [7] Canavan, G. "Integration Summary Report." *Proceedings of the Planetary Defense Workshop, Lawrence Livermore National Laboratory*. Livermore, California, May 22-26, 1995.
- [8] Canup, Robin, "Big Bang, New Moon: Theoretical and Computational Simulations at SwRI Could Soon Explain How the Earth Came to Have its Orbiting Neighbor." *Technology Today*. Southwest Research Institute, Spring 1999, <http://www.swri.edu/3pubs/ttoday/spring99/moon.htm>.
- [9] Chichka, D., The George Washington University, various personal correspondences.
- [10] Chapman, C., Durda, D., and Gold R. "The Comet/Asteroid Impact Hazard: A Systems Approach." 24 February 2001.
- [11] Chyba, C. F., Owen, T. C., and Ip, W. -H. "Impact Delivery of Volatiles and Organic Molecules to Earth." *Hazards Due to Comets and Asteroids*. Ed. Tom Gehrels. Tucson, The University of Arizona Press, 1994.
- [12] Conway, B. "Optimal Low-Thrust Interception of Earth-Crossing Asteroids." *Journal of Guidance, Control, and Dynamics*. **20** (5), pp. 995-1002.
- [13] Davies, P., "Planet X," Morrison, D., *NEO News* (personal newsletter). 14 Jan. 2002.

- [14] Duignan-Cabrera, A., Bullseye: Deep Impact Slams Into Comet. SPACE.com, 4 July 2005.
- [15] Gomes, R., et al, "Origin of the Cataclysmic Late Heavy Bombardment Period of the Terrestrial Planets." *Nature*, **435**, pp.466-469.
- [16] Grieve, R., and Shoemaker, E. "The Record of Past Impacts on Earth." *Hazards Due to Comets and Asteroids*. Ed. Tom Gehrels. Tucson, The University of Arizona Press, 1994.
- [17] Harris, A. "Evaluation of Survey Systems." *NASA NEO Survey Working Group*, 1996
- [18] Harvard-Smithsonian Center for Astrophysics, *Press Release No. 04-28*, August 31, 2004, <http://www.cfa.harvard.edu/press/pr0428.html>
- [19] Hills, J., and Mader, C. "Tsunami Produced by the Impacts of Small Asteroids." *Near-Earth Objects: The United Nations International Conference*. Ed. John Remo. New York, April 24-26, 1995.
- [20] Johns Hopkins University Applied Physics Laboratory NEAR home page: <http://near.jhuapl.edu/iod/20000216a/index.html>
- [21] Levy, Eugene H. "Early Impacts: Earth Emergent from its Cosmic Environment." *Hazards Due to Comets and Asteroids*. Ed. Tom Gehrels. Tucson, The University of Arizona Press, 1994.
- [22] Levy, David H. *Impact Jupiter: The Crash Of Comet Shoemaker-Levy 9*. New York, Plenum, 1995.
- [23] Lewis, J. *Rain of Fire and Ice: The Very Real Threat of Comet and Asteroid Bombardment*. Addison Wesley, 1996.
- [24] Melosh, H., Nemchinov, I., and Zetzer, Y. "Non-Nuclear Strategies for Deflecting Comets and Asteroids." *Hazards Due to Comets and Asteroids*. Ed. Tom Gehrels. Tucson, The University of Arizona Press, 1994.
- [25] Gugliotta, G., "A New Path for Asteroids," *The Washington Post*, 10 Nov 2005.
- [26] The MathWorks, Inc., "Using MATLAB," *The MathWorks, Inc.*, 1998.
- [27] Milani, Chesley, and Valsecchi, *Close Approaches of Asteroid 1999 AN10: Resonant and Non-Resonant Returns*, 12 May 1999, <http://www.cnn.com/2000/TECH/space/01/04/britain.asteroidwatch.ap/>

- [28] Minor Planet Center, Smithsonian Astrophysical Observatory, PHA web site: <http://cfa-www.harvard.edu/iau/lists/Dangerous.html>. (as of 17 July 05)
- [29] Morrison, D., "Has the Spaceguard Survey Made Us Any Safer?" *NEO News* (personal newsletter). 15 Jan. 2004.
- [30] Morrison, D., "Notes from Planetary Defense Conference," *NEO News* (personal newsletter). 25 Feb. 2004.
- [31] Morrison, D., "Summary of Tsunami Hazard Workshop, Houston 03/16/03," *NEO News* (personal newsletter). 17 Mar. 2003.
- [32] Morrison, D., Chapman, C., and Slovic, P. "The Impact Hazard." *Hazards Due to Comets and Asteroids*. Ed. Tom Gehrels. Tucson, The University of Arizona Press, 1994.
- [33] Morrison, D., Harris, A., Sommer, G., et al. "Dealing with the Impact Hazard." *Asteroids III (final draft)*. Ed. William Bottke, Alberto Cellino, et al. Tucson, The University of Arizona Press, 2003.
- [34] Mullen, L. "Toutatis: Almost Too Close for Comfort." *Astrobiology Magazine* (online), 27 Sep. 2004, <http://astrobio.net/news/modules.php?op=modload&name=News&file=article&sid=1219&mode=thread&order=0&thold=0>.
- [35] Naeye, R. "Chaos and Capture." *Sky and Telescope*, Sep. 2005, pp. 18-19.
- [36] NASA News Release "NASA Scientists Use Radar to Detect Asteroid Force." December 5, 2003.
- [37] NASA Ames Research Center "Asteroid and Comet Impact Hazards" web site: <http://impact.arc.nasa.gov/>
- [38] NASA Jet Propulsion Laboratory NEO Program web site: <http://neo.jpl.nasa.gov/neo/number.html>
- [39] NASA Jet Propulsion Laboratory Asteroid web site: http://echo.jpl.nasa.gov/asteroids/4179_Toutatis/toutatis.html
- [40] National Research Council, "New Frontiers in the Solar System: An Integrated Exploration Strategy." The National Academies Press, 2003.
- [41] Park, S., and Ross, M. "Two-Body Optimization for Deflecting Earth-Crossing Asteroids." *Journal of Guidance, Control, and Dynamics*, **22**, (3), pp. 415-420, 1999.

- [42] Price, S. “Infrared Detection and Characterization of Near Earth Objects.” *Proceedings of the Planetary Defense Workshop, Lawrence Livermore National Laboratory*. Livermore, California, May 22-26, 1995.
- [43] Prussing, J., and Conway, B. *Orbital Mechanics*. New York, Oxford University Press, 1993.
- [44] Rampino, M., and Haggerty, B. “Extraterrestrial Impacts and Mass Extinctions of Life.” *Hazards Due to Comets and Asteroids*. Ed. Tom Gehrels. Tucson, The University of Arizona Press, 1994.
- [45] Sagan, Carl. *Cosmos*. New York, Random House, 1980.
- [46] Shafer, B., Garcia, M., et al. “Non-Nuclear Strategies for Deflecting Comets and Asteroids.” *Hazards Due to Comets and Asteroids*. Ed. Tom Gehrels. Tucson, The University of Arizona Press, 1994.
- [47] Simonenko, V., Nogin, V., Petrov, D., et al. “Defending the Earth against Impacts from Large Comets and Asteroids.” *Hazards Due to Comets and Asteroids*. Ed. Tom Gehrels. Tucson, The University of Arizona Press, 1994.
- [48] Sky & Telescope's News Bulletin, “Double Trouble,” Morrison, D. *NEO News* (personal newsletter), 29 Sep. 2000.
- [49] Solem, J. “Interception and Disruption.” *Proceedings of the Planetary Defense Workshop, Lawrence Livermore National Laboratory*, Livermore, California, May 22-26, 1995.
- [50] Steel, D., and Harris, A. “The Berlin Declaration on the Cosmic Impact Hazard.” *Astronomy & Geophysics*, **43** (6).
- [51] Tagliaferri, E., et al. “Dealing With the Threat of an Asteroid Striking the Earth – An AIAA Position Paper.” AIAA. Apr, 1990.
- [52] Tedeschi, W. “Mitigation of the NEO Impact Hazard Using Kinetic Energy.” *Proceedings of the Planetary Defense Workshop, Lawrence Livermore National Laboratory*, Livermore, California, May 22-26, 1995.
- [53] Tenenbaum, D. “Colossal Cataclysm - Facing the Asteroid Threat” *NEO News* (personal newsletter), 2 Mar. 2000.
- [54] University of Illinois at Urbana-Champaign, 25 Nov 2002, “Scientists Studying Two Big Craters on Earth Find Two Causes” *University of Illinois at Urbana-Champaign News Bureau*.

[55] Urias, J., DeAngelis, I., et al. “Planetary Defense: Catastrophic Health Insurance for Planet Earth.” *U.S. Air Force*. Oct. 1996.

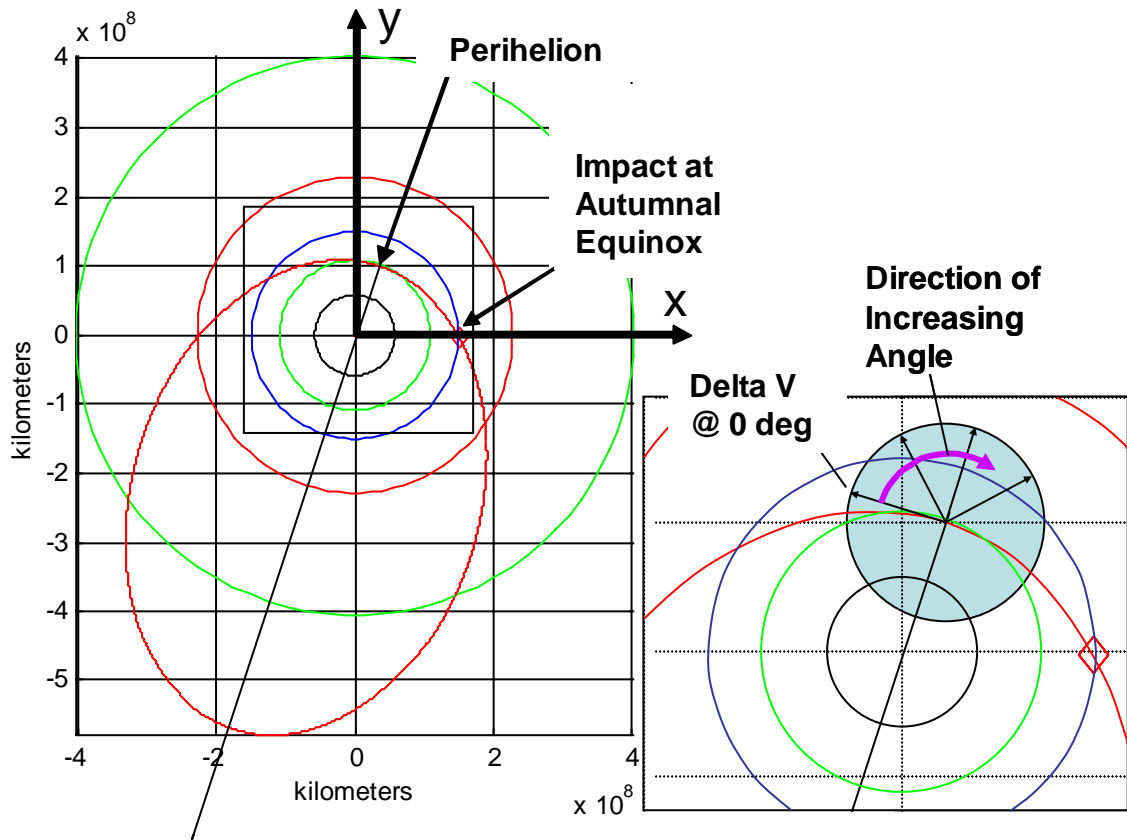
[56] Walton, M. “What Really Happened to the Dinosaurs?: Scientist Says Asteroid-Extinction Theory Too Simple” (interview with Professor Gerta Keller, Princeton University), *CNN*, Tuesday, March 2, 2004.

Appendix A – Perihelion Offset

Chapter 4, Section 4.1 discussed an offset between threat perihelion and the threat orbit location at which a deflection results in a maximum Earth miss. It was asserted that this offset was a simple manifestation of the relative motions of the Earth and the threat object. This appendix elaborates on the calculation of simplified post-deflections threat motions in support of this assertion.

A threat test case was chosen with an aphelion of 4 AU, zero-degree inclination, and an eccentricity of 0.7, resulting in a perihelion of approximately 0.706 AU, just inside the orbit of Venus as shown in Figure A-1. This threat was chosen because it has a noticeable eccentricity and a period that is long enough to allow sizable displacement effects to accumulate, but not so long that simulation run times would be inordinate. Based on the simulation code set that produced the data for the main body of this paper, a series of specialized codes was developed to investigate the displacements and relative motions involved in a progressive series of simplified deflection scenarios. The code set applies threat deflections at or shortly before threat perihelion, with the angle that measures deflection direction being defined at 0 degrees when aligned with the threat velocity vector and advancing clockwise as shown by the inset of Figure A-1. All deflections were performed in the plane of the threat's orbit. The code-based discussion that demonstrates the cause of the perihelion offset is introduced by way of a progressive analytic treatment to provide context for and a benchmarking of the code-generated results.

Figure A-1: Perihelion Offset Test Case



In accordance with the discussion of Section 4.1, a maximum increase in semi-major axis is obtained when a threat is deflected at the point in its orbit where its velocity is greatest, a condition that occurs at perihelion. Also, the optimal direction for that maximizing deflection is that which results in the largest velocity change. By the principles of vector addition, the deflection must therefore be either aligned with or in the opposite direction of the threat's instantaneous velocity; this corresponds to a direction angle of either 0 or 180 degrees. If these two conditions are satisfied, semi-major axis will experience the maximum change possible, with the location of maximum displacement from the original orbit being exactly at aphelion.

Velocity at perihelion for the test-case threat is found by way of the energy equation shown in Equation A.1:

$$\varepsilon = \frac{V^2}{2} - \frac{\mu_{Sun}}{r} = \frac{-\mu_{Sun}}{2a} \quad (A.1)$$

where, for any point in an orbit, ε is the orbital energy, V is velocity, μ_{Sun} is the Sun's gravitational parameter, r is the radius, and a is the semi-major axis. This is solved for velocity V by substituting in the value for the test case radius of perihelion for the variable r , resulting in Equation A.2:

$$V = \sqrt{\mu \left(\frac{2}{r} - \frac{1}{a} \right)} \quad (A.2)$$

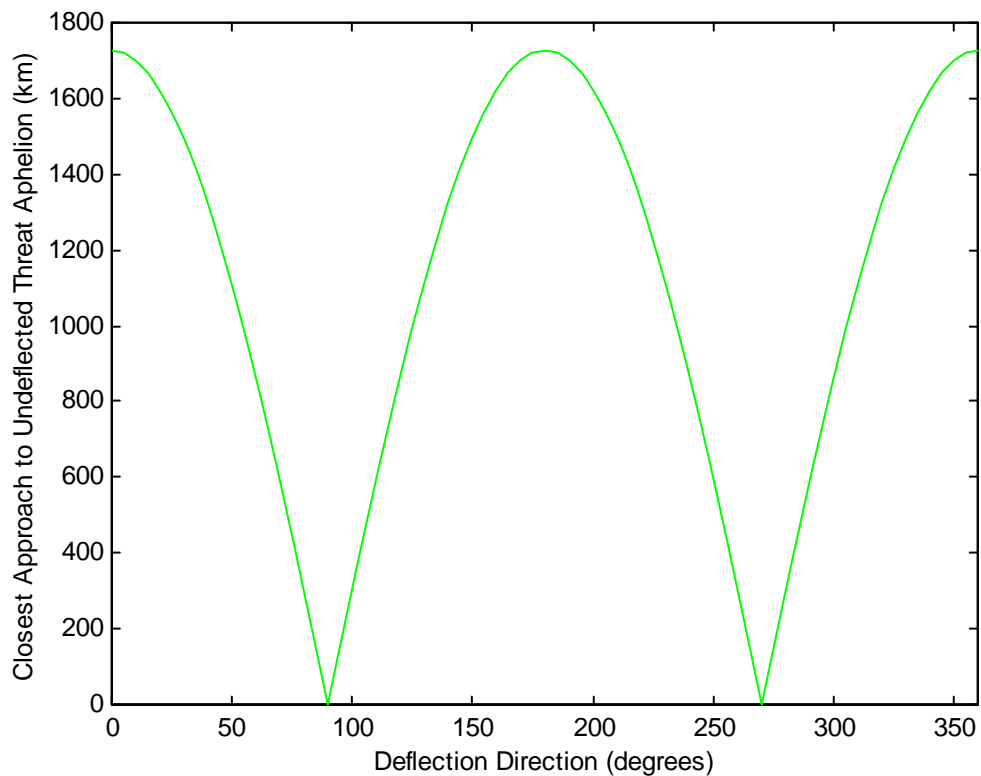
The resulting velocity at perihelion is approximately 46.22 km/s. Adding the 1-cm/s imparted velocity change to this and substituting the resulting modified velocity back into Equation A.1 results in a semi-major axis change of approximately 863 km, and an aphelion change of approximately 1726 km. With orbital period given by Equation A.3:

$$Period = 2\pi \sqrt{\frac{a^3}{\mu_{Sun}}} \quad (A.3)$$

it is found that the 1 cm/s velocity change delays the threat's arrival at aphelion by approximately 3.5 minutes.

The code-based investigation of these effects starts with the same 1-cm/sec velocity change applied exactly at perihelion. The deflected threat is then propagated along its new orbit to determine closest approach to what would have been the undeflected threat's aphelion. The code executes this for a series of deflections directions, and, in each case, finds the closest approach to the location of undeflected aphelion regardless of the required time of flight. The resulting distances, plotted against the direction of the imparted velocity, are shown in Figure A-2.

Figure A-2: Perihelion-Deflected Threat Closest Approach to Undeflected Threat Aphelion

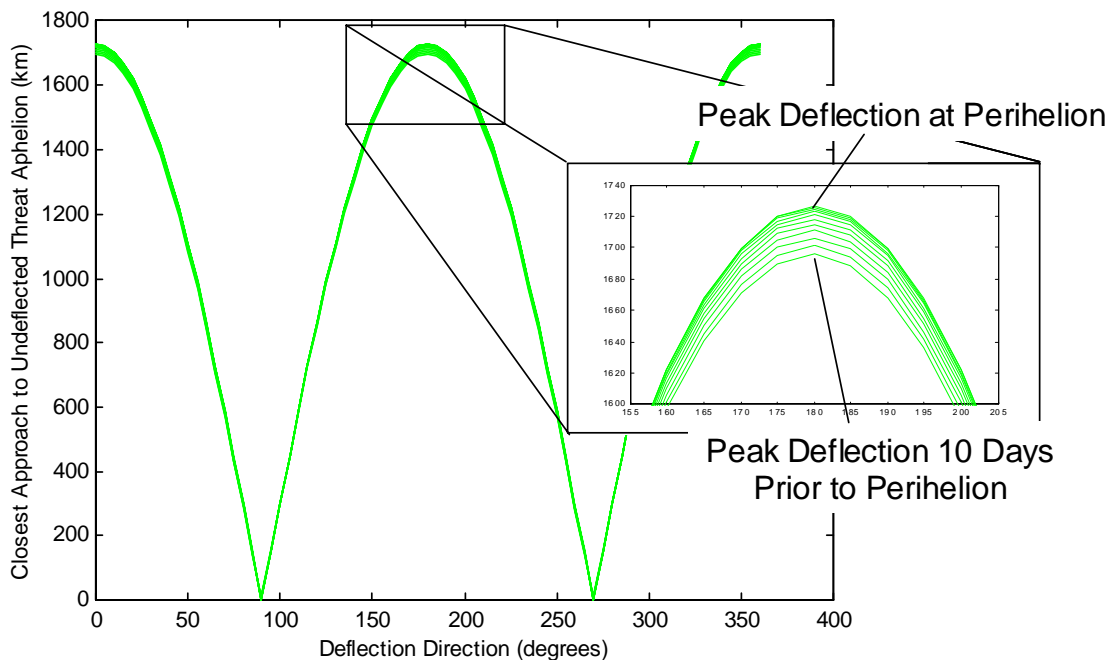


The trends are as expected in accordance with the discussion in Chapter 4, specifically, those involving Equations 4.1 and 4.2: the deflection directions causing greatest

displacement from the undeflected threat's aphelion are along the threat's orbital velocity (at 0 degrees) or anti-velocity (at 180 degrees) direction. More importantly, the peak deflection agrees with the 1726-km value developed by way of Equation A.2. Also of note is that there is no displacement when deflections occur along the orbit's major axis (i.e., at 90 and 270 degrees).

Next, an expanded code was developed to determine peak displacements for a 1-cm/s deflection at a various points prior to perihelion. Figure A-3, which reaches back 10 days prior to perihelion in increments of 1 day, shows that the results carry the same basic pattern as did deflections at perihelion, but that the maxima obtained decrease monotonically as the deflection is applied increasingly far away from perihelion. That monotonic behavior is indicated in the inset.

Figure A-3: Deflected Threat Closest Approach to Undeflected Threat Aphelion: Deflections Occurring Before Perihelion



More important than the trends of threat displacement at aphelion are those at the autumnal equinox, the assumed point of Earth impact. The angular location of that impact point with respect to the threat orbit's heliocentric orientation can be found by solving Equation A.4 for true anomaly ν at a radial distance of 1 AU:

$$r_{Earth\ impact} = \frac{h^2 / \mu_{Sun}}{1 + e \cos(\nu_{impact})} \quad (A.4)$$

where, for the appropriate eccentricity e , angular momentum magnitude h is found by multiplying the threat's perihelion distance by its velocity at perihelion. True anomaly for a post-aphelion impact is in this way calculated to be approximately 278 degrees, which can be roughly confirmed by inspection of Figure A-1. The corresponding eccentric anomaly E is found from Equation A.5:

$$E_{impact} = 2 \tan^{-1} \left(\sqrt{\frac{1-e}{1+e}} \tan \left(\frac{\nu_{impact}}{2} \right) \right) \quad (A.5)$$

and is found to be approximately 325 degrees, This is then substituted into Keplers equation for flight from perihelion, given by Equation A.6:

$$t_{impact} = \sqrt{\frac{a^3}{\mu_{Sun}}} [E_{impact} - e_{impact} \sin E_{impact}] \quad (A.6)$$

where E is eccentric anomaly. The undeflected threat time of flight from perihelion to Earth impact is approximately 110,137,853.66 seconds or about 3 years, 179 days, and slightly under 18 hours.

If the test threat is deflected at perihelion by 1 cm/s in the direction of the threat's instantaneous velocity vector, the modified eccentricity is calculated by Equation A.7:

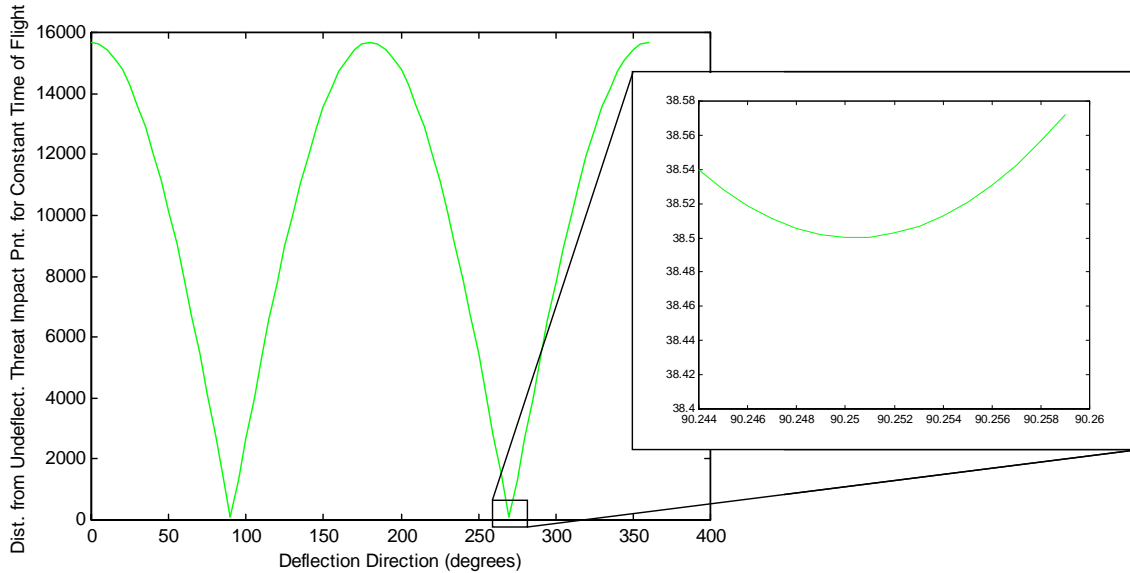
$$\bar{e}_{deflected} = \frac{1}{\mu_{sun}} \left[\left(V_{deflected}^2 - \frac{\mu_{sun}}{r_{perihelion}} \right) \bar{r}_{perihelion} - \left(\bar{r}_{perihelion} \bullet \bar{V}_{deflected} \right) \bar{V}_{deflected} \right] \quad (A.7)$$

where $V_{deflected}$ is the perihelion velocity calculated by Equation A.2 *plus* the 1 cm/s velocity change. The eccentricity of the deflected threat is found to be 0.70000073557293. Finally, when the deflected threat is allowed to fly for the *undeflected* threat's time of flight to impact, it's position relative to the autumnal equinox impact location is found by calculating the eccentric anomaly associated with that time of flight, determining the associated true anomaly to arrive at a deflected threat position vector, with vector subtraction then applied to determine a final impact-relative position vector.

The required eccentric anomaly value is found from iterative solution of Kepler's equation as given in Appendix B, Equations B.4 – B.7, and translation to true anomaly is accomplished with Equation B.8 in Appendix B. When the deflected threat position vector is developed from this, it is found that the offset from Earth's position at the autumnal equinox is nearly 16,000 km; the change in the threat's period has delayed its

arrival at the projected impact point. The behavior of the offset over a range of deflection directions is shown in Figure A-4.

Figure A-4: Distance from Undelected Threat Impact Point at Undelected Time of Flight from Perihelion



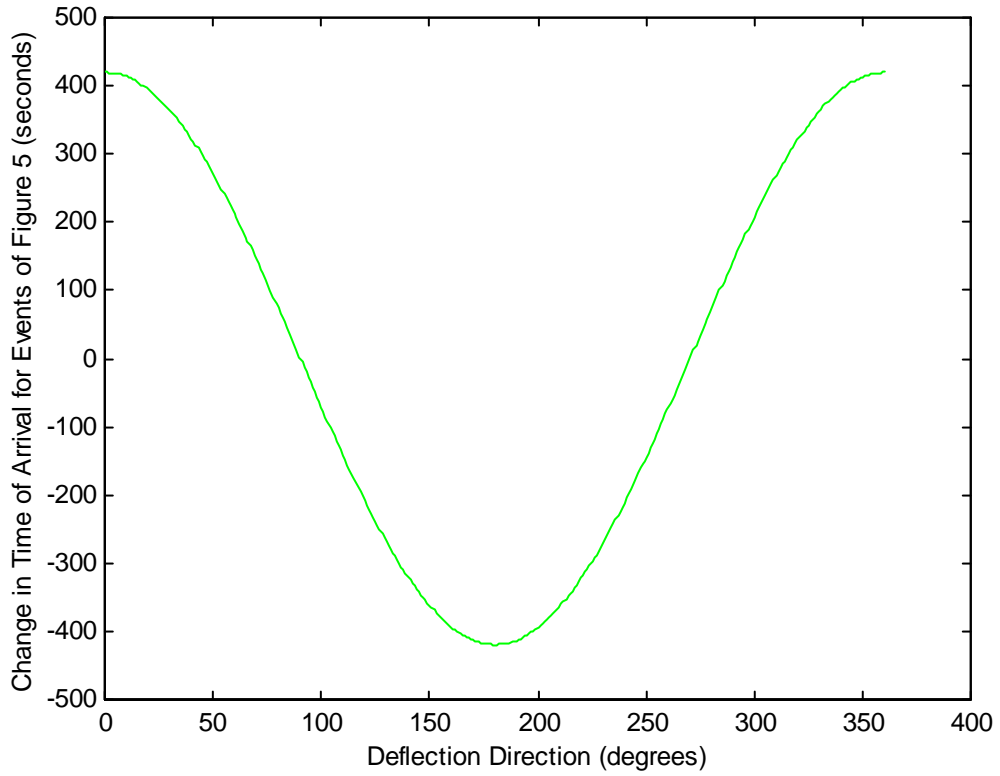
The curve confirms the analytic calculation of the peak offset's magnitude, and it displays the same symmetric pattern as did Figures A-2 and A-3. Deflections at 0, 180, and again at 360 degrees produced the largest changes in semi-major axis, and thus the largest changes in threat orbit period: with a set propagation time, threats deflected in these particular directions will fly either well past or fall well short of the original impact point, and thus produce large displacements. Deflections at 90 and 270 degrees, because they produced no aphelion change and therefore no change in threat period, again produced minimal displacements, but not zero displacements. As shown in the inset of Figure A-4, the displacements that do occur at these points are caused by the simple fact

that the threat's orbit has been changed, albeit slightly. Indeed, the output data show that the bottom of the 90- and 270-degree valleys on Figure A-4 are very small, bottoming out at approximately 38.5 km.

To further examine offset behaviors for pre-perihelion deflections, the threat's post-deflection time of flight can be made an independent variable and the threat propagated to the same true anomaly that resulted in an impact for the undeflected threat. This particular geometry is chosen so as to enable an analytic solution, which is accomplished by Equation A.4 using the deflected threat's angular momentum and eccentricity. The resulting offset from autumnal equinox is found to be only a little over 38 km from the original impact location. Time of arrival to this location, calculated by way of Equations A.5 and A.6, is found to be almost 420 seconds after the Earth's passage through autumnal equinox. With the Earth's orbital velocity at approximately 30 km/s, this translates to a threat-to-Earth displacement that is still over 12,500 km. This figure and the previously-calculated 16,000 km offset indicate that displacements of the level of interest for Earth protection are much more a function of a delay in threat arrival due to the change in threat period than they are a function of any lateral shift in the orbit.

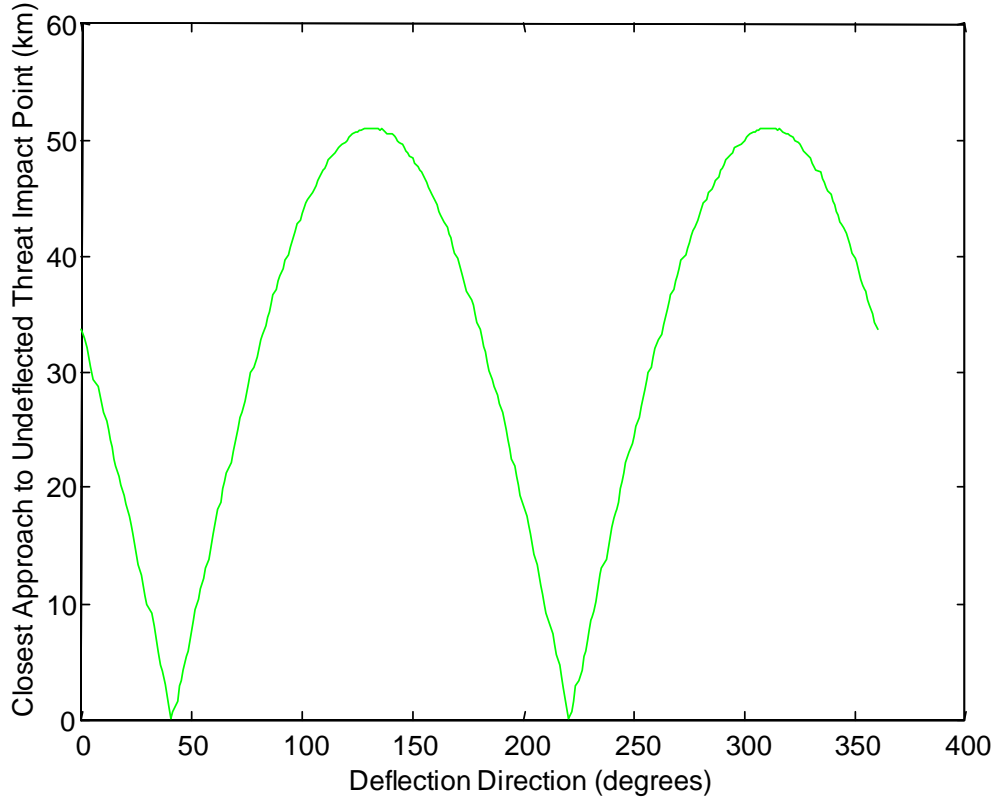
The process described above that determined the approximately-38-km offset was coded so as to find the closest threat passage to autumnal equinox over a range of directions for deflections at perihelion. The change in time of arrival at closest passage to the equinox compared to the time of flight to impact of the undeflected threat is plotted in Figure A-5. Positive time values indicate threat arrival after the expected time of impact of the undeflected threat.

Figure A-5: Change in Time of Arrival at Closest Passage to Undeflected Threat Impact Point



This matches the calculated peak temporal shift of around 420 seconds. Closest passage as a function of deflection direction is shown in Figure A-6.

Figure A-6: Deflected Threat Closest Approach to Original Impact Point



Most apparent is that with the shedding of the time-of-flight requirement, the symmetric nature of the data that was exhibited in Figure A-4 becomes skewed. Also of note is that the two “valleys” of the plot pass through zero, unlike those of Figure A-4. This can be understood by inspection. Consider that a deflection at perihelion in the direction of threat velocity (i.e., at 0 degrees) creates an orbit with larger semi-major and semi-minor axes: that new orbit fully envelopes the undeflected threat orbit. Likewise, a perihelion deflection at 180 degrees (opposite the direction of threat velocity) would produce semi-major and semi-minor axes that are *smaller* than those of the undeflected orbit: that deflected threat would lie completely *inside* the orbit of the undeflected threat. In transitioning from one of these threats to the other (i.e., from a fully internal orbit to a

fully external one), some set of orbits in between these two extremes must cross over the path of the undeflected threat, and two of those cases will happen to do so at autumnal equinox. For the chosen test threat, Figure A-6 shows that this happens to occur for deflection directions of approximately 40 and 220 degrees.

Beginning with the curve of Figure A-6 and adding deflections at a series of points prior to perihelion results in the behaviors shown in Figure A-7. This displays the same max/min pattern as did Figure A-3, with the maxima decreasing monotonically as the deflection is moved farther away from perihelion. The monotonic decrease for this case is demonstrated in Figure A-8, a plot of the peak displacements for earlier-than-perihelion deflections in 1-hour increments.

Figure A-7: Deflected Threat Closest Approach to Original Impact Point: Deflections Occurring Before Perihelion

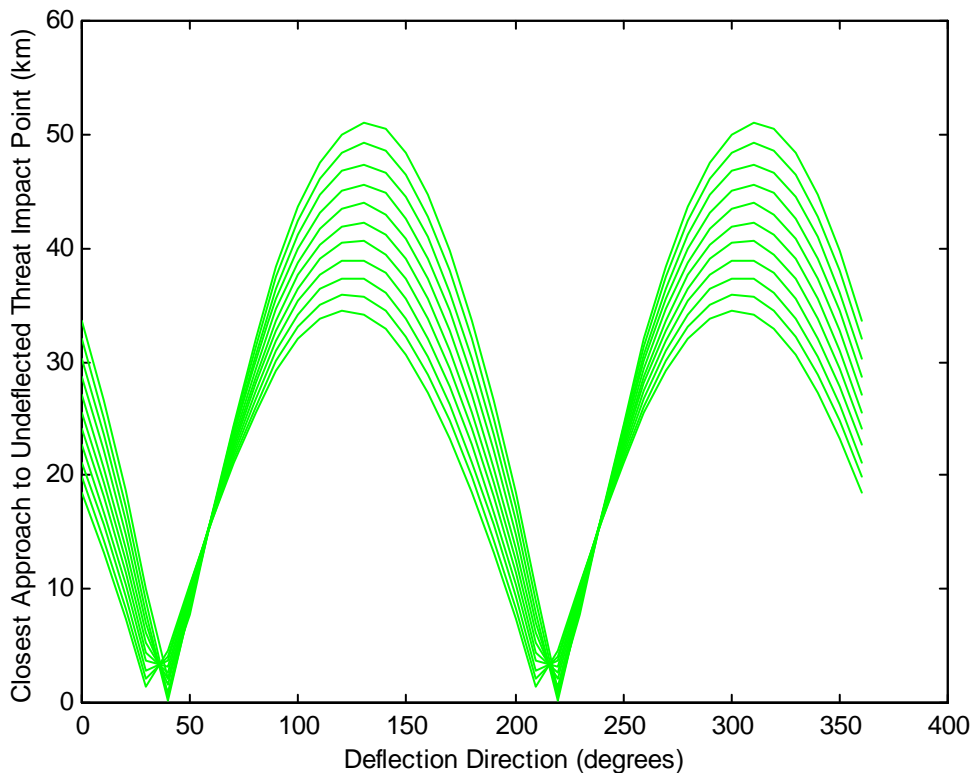
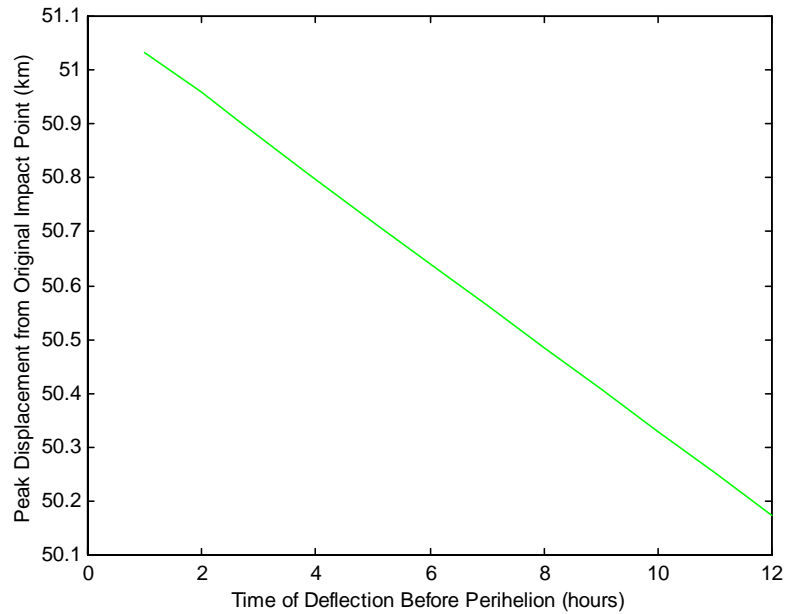


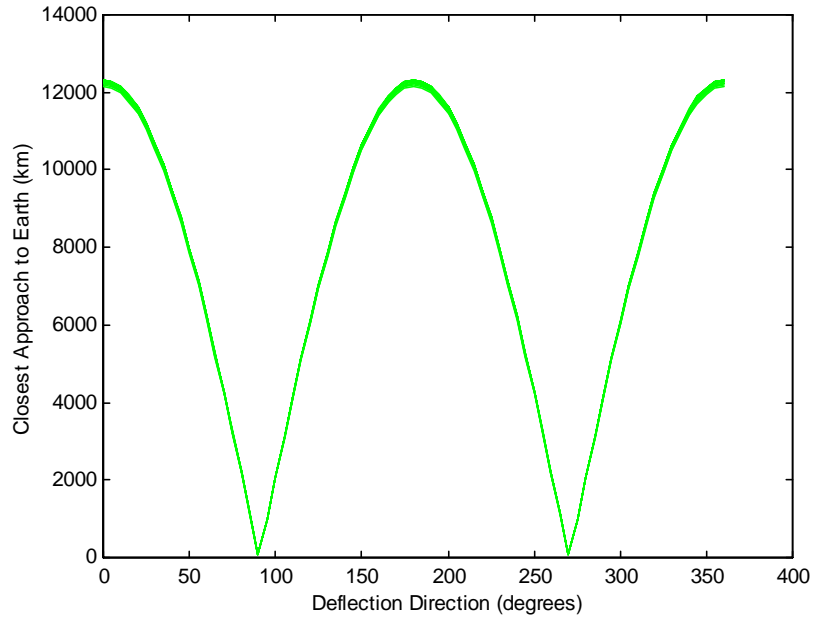
Figure A-8: Monotonic Decrease in Threat Closest Approach to Original Impact Point: Deflections Occurring Before Perihelion



The final and key measure of interest is displacement from the Earth itself. Even though the effects of Earth gravity are being ignored for the purposes of this appendix, the determination of minimum threat passage to Earth still requires independent tracking of the simultaneous motions of both bodies, and an iterative solution of the distance between them. While the previous steps of this development were each introduced by an analytic treatment, the Earth-relative displacement calculation is best executed by code, although it is fully described by equations of this appendix.

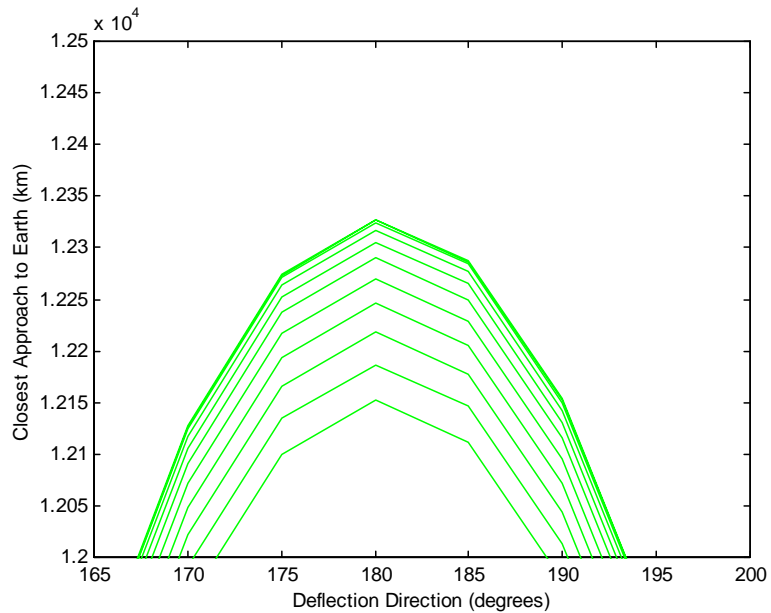
The code in question was run over the full span of deflection directions from 0 through 360 degrees, and for a series of threat positions prior to perihelion. The results are shown in Figure A-9 for 1-day increments moving back to 10 days prior to perihelion.

Figure A-9: Deflected Threat Closest Approach to Earth: Deflections Occurring Before Perihelion



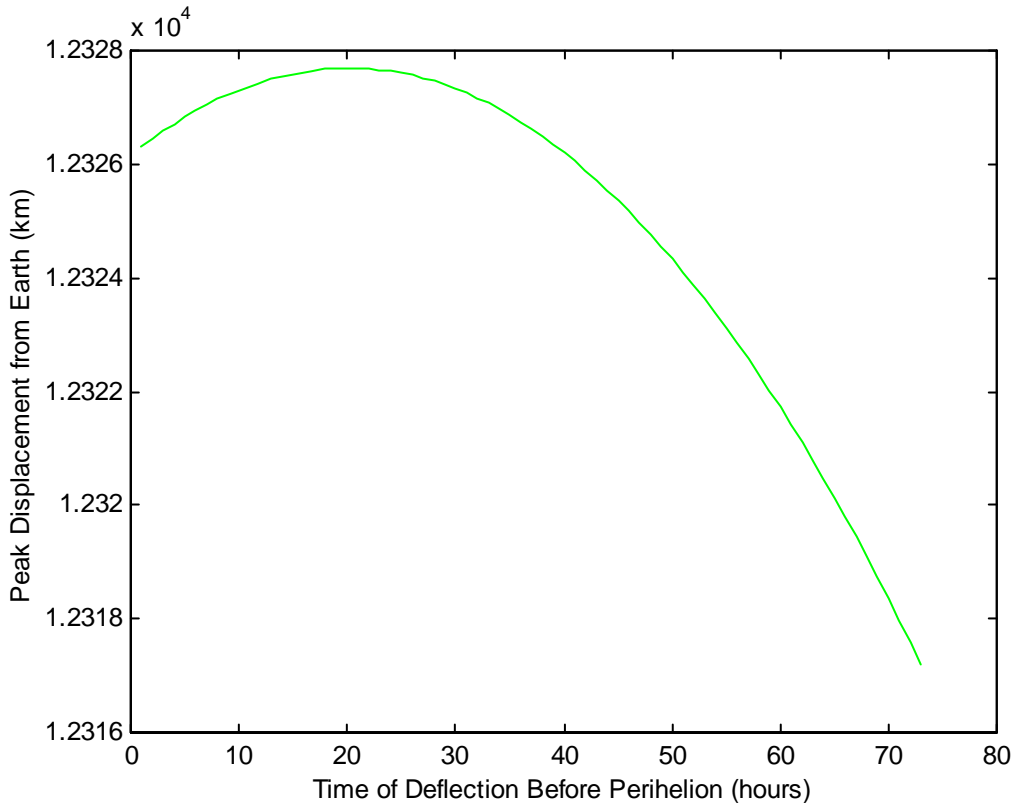
Zooming into the middle peak, the behavior at first appears to be monotonically declining, as it was for the other displacement metrics. This is shown in Figure A-10.

Figure A-10: Zoom in of Deflected Threat Closest Approach to Earth: Deflections Occurring Before Perihelion



However, a pattern quite different from the monotonic behavior of Figure A-8 emerges when the peak displacement values are plotted against time before perihelion on an hourly scale, as shown in Figure A-11.

Figure A-11: Non-Monotonic Behavior in Threat Closest Approach to Earth: Deflections Occurring Before Perihelion



It appears that the offset between threat perihelion and the deflection point offering maximum threat displacement at Earth has its roots in the simple relative motions expected of two orbiting bodies and in how those motions change with changing orbit size (semi-major axis), shape (eccentricity), and orientation (argument of perihelion) for earlier and earlier deflections.

Appendix B – Simulation Code Description

What follows is a detailed breakout of the approaches taken and the equations used in the core displacement calculation code, expanding on the description given in Section 3.2, Threat Simulation Modeling. This discussion will focus on the principal equations only. Applications of common or standard equations are simply referenced, and the discussion does not delve into the numerous control algorithms used for such functions as selection from among various scenario options, resolving of quadrant ambiguities, or initialization of iterative solution schemes.

The first process of interest in the operation of the displacement code is the assignment of values to the user-controlled variables. These are the magnitude of the velocity change that is to be imparted to a threat object, the direction of that velocity change as described by the variable “Transangle,” and the key threat orbital elements at impact: eccentricity (e_{impact}), inclination (i_{impact}), and radius of perihelion (rp_{impact}). Standard equations are then used to calculate semi-major axis (a_{impact}), and semi-latus rectum (p_{impact}), thus establishing the threat orbit’s size, shape, and tilt.

The code next determines the threat orbit’s inertial orientation required to force the threat to cross the Earth’s orbit at autumnal equinox, which was selected as the universal impact location because of convenience of sign convention relative to the heliocentric inertial Cartesian coordinate system. Earth’s orbit is assumed to be circular at 1 AU, but because threat orbital elements are selected parametrically, no reduction in the applicability of the representative threat set is suffered by ignoring the slight eccentricity of Earth’s orbit. To force the threat through autumnal equinox, longitude of ascending

node is set to zero and the value of argument of perihelion is found that forces a threat ecliptic crossing at the desired 1 AU. This is accomplished with Equation B.1:

$$\omega_{impact} = \cos^{-1} \left(\frac{1}{e_{impact}} \left(\frac{P_{impact}}{AU} \right) - 1 \right) \quad (B.1)$$

Next, the model performs a backward propagation of both the Earth and the threat to find the pre-impact time at which the Earth-to-threat distance equals the radius of the Earth-to-Sun gravitational sphere of influence (SOI). The SOI definition used is that suggested by Laplace as shown in Equation B.2:

$$R = D \left(\frac{m_{Earth}}{m_{sun}} \right)^{2/5} \quad (B.2)$$

where D is the distance between the Earth and the Sun (i.e., 1 AU); m_{earth} and m_{sun} are the Earth and Sun masses, respectively; and R is the sphere of influence radius, which is found to be just less than 925,000 km or about two and a third times the Earth-Moon distance.

The propagation algorithm is initialized with the undeflected threat's eccentric anomaly at Earth impact (E_{impact}), calculated by Equation B.3:

$$E_{impact} = 2 \tan^{-1} \left(\sqrt{\frac{1 - e_{impact}}{1 + e_{impact}}} \tan \left(\frac{v_{impact}}{2} \right) \right) \quad (B.3)$$

where the undeflected threat's true anomaly (ν_{impact}) is found from the fact that the threat ascending node is at Earth impact, so ν_{impact} is simply one full threat revolution (i.e., 2π radians) less ω_{impact} .

After seeding the propagation algorithm with an estimate of the “backward” time of flight from Earth impact to the SOI, iterations are performed to find a converged solution to Kepler's equation, and the threat location associated with that initial time of flight estimate is determined. Kepler's equation itself is given as Equation B.4:

$$t_{impact} - t_{SOI} = \sqrt{\frac{a_{impact}^3}{\mu_{Sun}}} [E_{impact} - E_{SOI} - e_{impact} (\sin E_{impact} - \sin E_{SOI})] \quad (B.4)$$

where μ_{Sun} is the Sun gravitational parameter. The solution is accomplished by way of a Newton iteration, the equations for which are:

$$F(E_{SOI}) = E_{impact} - E_{SOI} - e_{impact} (\sin E_{impact} - \sin E_{SOI}) - (t_{impact} - t_{SOI}) \sqrt{\frac{\mu_{Sun}}{a_{impact}^3}} \quad (B.5)$$

and its derivative:

$$F'(E_{SOI}) = 1 - e_{impact} \cos(E_{SOI}) \quad (B.6)$$

These are solved according to Equation B.7:

$$E_{(SOI)_{k+1}} = E_{(SOI)_k} - \frac{F(E_{(SOI)_k})}{F'(E_{(SOI)_k})} \quad (B.7)$$

The subscripts track the relation between functional values of the current ($k+1$) and the previous (k) iteration step. The solution was assumed to be converged when subsequent iterations closed to within a tolerance of 1×10^{-8} , producing a maximum positional error of less than 1 km at 1 AU.

The converged output of this first cycle of the iterative process is E_{SOI} , an estimate of the heliocentric eccentric anomaly of the undeflected threat at the SOI. E_{SOI} is then translated to an estimated heliocentric true anomaly ν_{SOI} by way of Equation B.8:

$$\nu_{SOI} = 2 \tan^{-1} \left(\sqrt{\frac{1+e_{impact}}{1-e_{impact}}} \tan \left(\frac{E_{SOI}}{2} \right) \right) \quad (B.8)$$

and then to an estimated heliocentric distance r_{SOI} with Equation B.9:

$$r_{SOI} = \frac{p_{impact}}{1 + e_{impact} \cos(\nu_{impact})} \quad (B.9)$$

Estimated heliocentric perifocal coordinates of the threat at the SOI are determined according to Equations B.10 and B.11:

$$r_{SOI}^1 = r_{SOI} \cos(\nu_{SOI}) \quad (B.10)$$

$$r_{SOI}^2 = r_{SOI} \sin(v_{SOI}) \quad (B.11)$$

where the “1” superscript indicates the primary perifocal coordinate that lies along the eccentricity vector and pierces threat perihelion, and the “2” superscript represents the perifocal coordinate located at a true anomaly of 90 degrees. (Because of the nature of perifocal coordinates, the threat position vector has no component in the third coordinate direction, which is normal to threat orbit plane.) The threat’s estimated perifocal coordinates are then transformed into the heliocentric coordinate system with the primary coordinate lying along the direction of vernal equinox. The transformation is given in Equation B.12:

$$\begin{Bmatrix} r_1 \\ r_2 \\ r_3 \end{Bmatrix} = \begin{bmatrix} \cos \Omega \cos \omega - \sin \Omega \cos i \sin \omega & -\cos \Omega \sin \omega - \sin \Omega \cos i \cos \omega & \sin \Omega \sin i \\ \sin \Omega \cos \omega + \cos \Omega \cos i \sin \omega & -\sin \Omega \sin \omega - \cos \Omega \cos i \cos \omega & -\cos \Omega \sin i \\ \sin i \sin \omega & \sin i \cos \omega & \cos i \end{bmatrix} \begin{Bmatrix} r_1 \\ r_2 \\ r_3 \end{Bmatrix} \quad (B.12)$$

The Earth is also back propagated by the threat’s estimated time of flight to the SOI. The position vector of the center of the Earth with respect to the threat is calculated by vector subtraction of the respective heliocentric position vectors, and the magnitude of the resultant vector is compared to the SOI distance. If the threat location is inside of the SOI, time of flight is increased and the iteration is cycled; if the location is outside, time is decreased and the iteration is cycled. This process continues until a threat location is found within approximately 10 km of the SOI, which was determined to provide

sufficiently converged results across the representative threat space within a reasonable number of iterations.

From this point in the simulation, whenever the threat is inside of the SOI it is modeled as moving solely under Earth’s gravity, which will, for the objects in question, be along hyperbolic paths in geocentric space. However, the threat velocity vector at its current position on the SOI is still that which was calculated to deliver the threat to a center-to-center Earth impact along an elliptical path in heliocentric space. The velocity vector that the threat needs to possess is that which places it on a path leading to a dead-on impact under the influence of Earth’s gravity only. To make the needed modification, the velocity portion of the threat state vector at the SOI is realigned so as to point directly at the Earth’s center, thus guaranteeing a “dead-on” hit under the influence of Earth gravity only. This process begins with a calculation of the threat’s heliocentric perifocal velocity vector according to Equations B.13 and B.14:

$$V1_{SOI} = \sqrt{\mu_{Sun}/p} (-\sin v_{SOI}) \quad (B.13)$$

$$V2 = \sqrt{\mu_{Sun}/p} (e + \cos v_{SOI}) \quad (B.14)$$

As was the case with heliocentric perifocal position, perifocal velocity has no component in the coordinate direction normal to threat orbit plane.

Next, the transformation in Equation B.12 is applied to the heliocentric perifocal velocity vector to place it into the heliocentric coordinate system. The Earth velocity

vector is then subtracted from that of the threat to determine the velocity of the threat with respect to the Earth. A unit vector is then created that points directly at the Earth from the threat's position at the SOI. This is done by dividing the position vector of the center of the Earth with respect to the threat by its own magnitude. That unit vector is then multiplied by the magnitude of the Earth-relative velocity vector of the threat, effectively rotating the threat velocity so as to be pointing directly *at* the Earth. Note that this threat velocity adjustment does not have to be performed in geocentric coordinates: a vector determined inertially to be pointing at the Earth will point at the Earth regardless of the inertial coordinate system in which it is described.

The modification to the threat velocity vector changes the threat orbit, so threat orbit elements must therefore be updated according to the original threat position vector at SOI and the updated velocity vector. This is accomplished as follows, starting with eccentricity:

$$\bar{e}_{adjusted} = \frac{1}{\mu_{sun}} \left[\left(V_{adjusted}^2 - \frac{\mu_{sun}}{r_{SOI}} \right) \bar{r}_{SOI} - (\bar{r}_{SOI} \cdot \bar{V}_{adjusted}) \bar{V}_{adjusted} \right] \quad (B.15)$$

Next, the nodal vector is determined as:

$$n_1 = -h_2; \quad n_2 = h_1 \quad (B.16)$$

where n_1 and n_2 are the first and second coordinates of the nodal vector (the third coordinate of the nodal vector being zero in this and any perifocal coordinate system),

and h_1 and h_2 are the first and second coordinates of the angular momentum vector, calculated by:

$$\bar{h} = \bar{r}_{SOI} \times \bar{V}_{adjusted} \quad (B.17)$$

Continuing, with h_3 being the component of angular momentum normal to the heliocentric plane, and h being the total angular momentum magnitude, inclination is calculated as:

$$\cos i_{adjusted} = \frac{h_3}{h} \quad (B.18)$$

Because the original threat orbit passed through the ecliptic at autumnal equinox, its longitude of ascending node Ω was zero. In general, however, the velocity vector adjustment just described will create a non-zero Ω , calculated by Equation B.19, with n_1 being the primary component of the nodal vector, and n being the nodal vector calculated magnitude:

$$\cos \Omega_{adjusted} = \frac{n_1}{n} \quad (B.19)$$

Argument of periapsis is calculated by:

$$\cos \omega_{adjusted} = \frac{\bar{n} \bullet \bar{e}_{adjusted}}{ne_{adjusted}} \quad (B.20)$$

Finally, semi-latus rectum (p) and semi-major axis (a) are calculated as:

$$p_{adjusted} = \frac{h^2}{\mu_{sun}} \quad (B.21)$$

$$a_{adjusted} = \frac{p_{adjusted}}{1 - e_{adjusted}^2} \quad (B.22)$$

With the modified threat orbit now determined, the threat and the Earth are again back propagated by the amount of time before impact at which the deflection will occur less the threat time of flight from the SOI to impact. Once at the location at which the deflection will occur (at the heliocentric position vector $r_{deflect}$), a local orbit-based coordinate system is defined with the threat's instantaneous velocity vector as the second coordinate axis (y), and the threat orbit normal as the third coordinate axis (z). The primary coordinate (x) is then developed by crossing the secondary coordinate into the third.

The direction in which the velocity change will be applied is defined relative to this coordinate system by way of a "Transangle," defined as being zero degrees when the imparted velocity is directed along the primary local coordinate, and as 90 degrees when aligned with the threat's instantaneous velocity vector. Out-of-plane deflections in

general do not add significantly to the attainable threat displacement, and where therefore not included in the main analysis (see Section 3.2 for addition detail). The components of the applied velocity change ΔV are calculated according to Equations B.23 and B.24, where ΔV_A is the component along the primary, “outward” pointing coordinate, and ΔV_B is the component in the direction of the threat’s instantaneous velocity vector:

$$\Delta V_A = \Delta V \cos(\text{transangle}) \quad (B.23)$$

$$\Delta V_B = \Delta V \sin(\text{transangle}) \quad (B.24)$$

The velocity change vector in the orbit-based frame can be written in the heliocentric frame by multiply it by a matrix whose columns are the unit vectors of the heliocentric frame written in terms orbit-based frame. Because the second coordinate of the orbit-based frame was defined as lying along the threat’s instantaneous velocity vector at the location of the deflection, it can be expressed in the heliocentric frame with Equation B.25:

$$\hat{y} = \frac{\bar{V}_{adjusted}}{|\bar{V}_{adjusted}|} \quad (B.25)$$

Because the third coordinate z was defined as normal to the threat orbit plane, there are several acceptable approaches to determining its equation. Equation B.26 shows the generalized approach coded for the displacement simulation:

$$\hat{z} = \frac{\bar{r}_{deflect} \times \hat{y}}{|\bar{r}_{deflect} \times \hat{y}|} \quad (B.26)$$

but creating a unit vector from the angular momentum would have produced the same result. Finally, the primary orbit-based axis is calculated as:

$$\hat{x} = \frac{\hat{y} \times \hat{z}}{|\hat{y} \times \hat{z}|} \quad (B.27)$$

The actual transformation of the velocity change applied to the threat from orbit-based local coordinates to heliocentric coordinates is as shown in Equation B.28:

$$\begin{Bmatrix} \Delta V_x \\ \Delta V_y \\ \Delta V_z \end{Bmatrix}_{heliocentric}^{deflected} = \begin{bmatrix} x_A & y_A & z_A \\ x_B & y_B & z_B \\ x_C & y_C & y_C \end{bmatrix} \begin{Bmatrix} \Delta V_A \\ \Delta V_A \\ \Delta V_A \end{Bmatrix}_{Orbit-based}^{deflected} \quad (B.28)$$

The threat's post-deflection heliocentric velocity vector is then found by vector addition of the threat pre-deflection heliocentric velocity vector and the velocity change vector that was just transformed from the local orbital coordinate system. The orbital elements for the deflected threat are then updated by way of Equations B.15 through B.22.

Next, the threat is propagated forward on the newly-defined orbit to a location near the SOI. The process for finding a location on the deflected threat orbit that is within the desired 10 km of the SOI is similar to that is applied during the original back propagation to the SOI: Kepler's equation is solved iteratively (Equations B.3 through B.7) with the

time of flight varied according to whether test propagations place the threat inside or outside of the SOI.

When a threat position sufficiently close to the SOI is found, the Earth is forward-propagated by the associated amount of time, and the threat's Earth-relative heliocentric position and velocity vectors are determined by vector subtraction. Finally, hyperbolic miss distance is calculated by first using the Earth-relative position and velocity vectors in Equation B.15 to determine eccentricity, and then substituting into Equation B.29:

$$r_{miss} = (e - 1) \frac{\mu}{V^2} \quad (B.29)$$

which is based on the patch-conic assumption that the hyperbolic velocity at the SOI is V_∞ . When this assumption is substituted into the energy equation, the result is Equation B.30:

$$\varepsilon = \frac{V_\infty^2}{2} - \frac{\mu}{\infty} = \frac{-\mu}{2a} \quad (B.30)$$

Solving for semi-major axis in Equation B.31:

$$r_{periapsis} = a(1 - e) \quad (B.31)$$

Substituting into Equation B.30, and solving for $r_{periapsis}$ indeed yields Equation B.29. The V_∞ patched-conics assumption can also be ignored; the Earth-relative position and

velocity vectors would then be used to calculate angular momentum for use in Equation B.32:

$$r_{periapsis} = \frac{h^2 / \mu_{Earth}}{1 + e_{impact} \cos(0)} \quad (B.32)$$

This approach results in less-conservative deflection estimates: they are slightly larger than but well within 1% of those determine with the patched-conics approach.